

https://dspace.org/

Influence of ruthenium and molybdenum ion implantation on the machining performance of WC-Co straight grade inserts

Mkhaliphi, Thuli Goodness

2019

https://hdl.handle.net/10539/29084

Mkhaliphi, Thuli Goodness, 2019, Influence of ruthenium and molybdenum ion implantation on the machining performance of WC-Co straight grade inserts, University of the Witwatersrand, https://hdl.handle.net/10539/29084

Downloaded from a DSpace repository. https://dspace.org/

Influence of Ruthenium and Molybdenum Ion Implantation on the Machining Performance of WC-Co Straight Grade Inserts



UNIVERSITY OF THE
WITWATERSRAND,
JOHANNESBURG

Thuli Goodness Mkhaliphi

A dissertation submitted to the Faculty of Engineering and the Built Environment, University of the Witwatersrand, Johannesburg, in fulfilment of the requirements for the degree of Master of Science in Engineering.

July 2019

Declaration

I declare that this report is my own unaided work. It is to be submitted for the Masters of Science in Engineering at the University of the Witwatersrand, Johannesburg. This report has never been submitted before for any degree or examination in any other University.

Student Name: Thuli Mkhaliphi; Student No.: 0511221h

Student Signature……

Abstract

The aim of this study was to determine the effect of Ru and Mo ion implantation on the tool life of WC-Co straight grade cutting tool inserts during face milling of AISI H13 tool steel. The cutting tool inserts were implanted at 6 different ion implantation dosages. The acceleration voltage was kept constant for 5 ion implantation dosages at 100 keV and it was then increased to 120 keV for one of the ion implantation dosages. The face milling tests were conducted under unlubricated conditions according to ISO standard 8688-1: 1989. In order to ensure intermittent conditions the radial depth of cut was set at 30% of the cutter diameter. A 5 insert cutter was fully loaded during machining. The non-implanted inserts were used as the baseline for the volume of material to cut. The induced cutting forces of the ion implanted inserts were higher than that of non-implanted inserts due to increased shear area as a result of cutting edge chipping. The estimated heat generated when using ion implanted inserts had a scattered relationship with respect to the non-implanted inserts; this was attributed to the several factors involved in heat generation during machining. Several overlapping failure mechanisms were observed between the non-implanted and ion implanted inserts. The flank wear scar of the ion implanted inserts was smaller than that of non-implanted inserts indicating abrasion resistance from increased micro-hardness resistance. Even though the surface roughness of the machined components using ion implanted inserts was slightly higher than that of non-implanted inserts, it was still within allowable tolerances. Uncoated inserts failed prematurely due to workpiece adhesion that resulted to flaking and excessive chipping on the rake face. The ion implantation dosage of 8E+15 ions/cm^2 at 100 keV and 2E+16 ions/cm^2 at 120 keV were the best dosages with low wear rate, acceptable surface roughness and heat generation similar to that of non-implanted inserts.

Acknowledgements

Assoc. Professor N. Sacks, for providing the project, exceptional supervision, her support, patience, encouragement, insight and technical guidance throughout this work. Prof, I am truly grateful for everything.

Dr. P. Nunthavarowong, for the many helpful suggestions and technical support.

The School of Chemical and Metallurgical Engineering support staff, namely, Hopewell Gumede, Donald Mahole, Shadrack Maqobane and Brayner Neluwani) and Postgraduates colleagues from office RW 411 for their friendship and support.

The School of Mechanical, Industrial and Aeronautical Engineering staff namely, Dr. R Genga, Mr M. Leering, Prof. F. Keinhofer, Mr S. Riekert and Mr Lionel Classen) are acknowledged for their continued interest and support.

The School of Physics, Prof T. Derry for his technical support

The Staff at Microscopy and Microanalysis Unit, Ms T. Xuma for the use of the MMU equipment.

iThemba LABS for allowing me to use their facilities and Mr T. Miller and Dr. M. Madhuku for the technical support

Pilot Tools (Pty) Ltd, for providing the testing facilities and donating the uncoated samples, Dr. C. Freemantle and Ms. A. Mtonjeni are acknowledged for their technical support.

NECSA for providing the facilities for the residual stress measurements and Dr. T. Ntsoane and Dr. A Venter for the technical support.

The DST and NRF, South Africa, for supporting the DST/NRF CoE in Strong Materials, for financially supporting my research and up keep.

My parents, brothers and friends, for their love, support and prayers.

Finally, Jehovah God, for providing me with strength and support every day of my MSc.

Table of Contents

Chapter 1 Introduction 2
1.1 Background and motivation for research 2
1.2 Research Aim and Objectives 4
1.3 Contribution to knowledge 4
1.4 Structure of the dissertation 4
Chapter 2 Literature Review 6
2.1 Cemented tungsten carbide tools 6
2.2 Ion implantation 9
2.2.1 Ion implantation of uncoated and coated WC-Co 11
2.3 Milling 15
2.4 Failure mechanisms of WC-Co tools 20
2.4.1 Deformation 21
2.4.2 Diffusion wear 22
2.4.3 Attrition wear 22
2.4.4 Abrasive wear 24
2.4.5 Fracture 24
2.4.6 Thermal fatigue 25
2.5 Literature Review Summary 26
Chapter 3 Experimental Procedures 27
3.1 Materials 28
3.2 Ion Implantation 28
3.3 Face Milling Test 29
3.4 Materials Characterisation Tests 32
3.4.1 Coercivity 32
3.4.2 Magnetic Saturation 32
3.4.3 Porosity 33

3.4.4 Density 33
3.4.5 Sample Preparation 33
3.4.6 Vickers Hardness 34
3.4.7 Fracture Toughness 35
3.4.8 Quantitative Microstructural Analyses 36
3.4.9 Crystalline Phase Identification 37
3.4.10 X-ray Photoelectron Spectroscopy (XPS) 37
3.4.11 Time-of-Flight Secondary Ion Mass Spectroscopy (TOFSIMS) 38
3.4.12 Atomic Force Microscope (AFM) 38
3.4.13 Residual Stress Measurements 38
3.4.14 Rutherford Backscattering Spectroscopy (RBS) 39
Chapter 4 Results 41
4.1 Characterisation of the cutting tool inserts prior to ion implantation 41
4.2 Workpiece 43
4.3 Characterisation of the Ru and Mo ion implanted cutting tool inserts 44
4.3.1 FESEM and EDS analyses 44
4.3.2 Rutherford Backscattering Spectroscopy (RBS) 49
4.3.3 Micro-hardness of the cutting tool inserts 51
4.3.4 Surface Roughness 52
4.3.5 Residual Stresses 54
4.3.6 Grazing Incident X-ray Diffraction (GIXRD) 55
4.3.7 X-ray Photoelectron Spectroscopy (XPS) 57
4.3.8 Time of Flight Secondary Ion Mass Spectroscopy 60
4.4 Face Milling Test Results 62
4.4.1 Machining Analyses 62
4.4.2 Tool Inserts Failure Mechanisms 65
4.4.3 Cutting Chips Analyses 72

4.4.4 Steel Machined Surface Analyses....78
Chapter 5 Discussion....81
5.1 Influence of Ru and Mo ion implantation on the material properties of WC-6wt%Co cutting tool inserts....81
5.1.1 Coated cutting tool inserts....81
5.1.2 Effect of increased voltage during ion implantation....85
5.1.3 Comparison between coated and uncoated inserts....86
5.2 Machining performance of coated cutting tool inserts....87
5.2.1 Coated Cutting tool inserts....88
5.2.2 Effect of increased acceleration voltage during ion implantation....94
5.2.3 Comparison between coated and uncoated cutting tool inserts....94
Chapter 6 Conclusions....97
Chapter 7 Recommendations....99
Chapter 8 References....100
Appendix A....106
FESEM micrographs of the coated ion implanted cutting tool inserts cross-sections....106
Appendix B....108
Rutherford Backscattered Spectroscopy (RBS)....108
Appendix C....111
Grazing incident X-ray Diffraction Patterns....111
Appendix D....115
Time-of-Flight Mass Ion Mass Spectroscopy (TOFSIMS)....115
Appendix E....117
Flank face of the coated inserts....117
Flank face of the uncoated inserts....119
Appendix F....120
FESEM micrographs of the failed coated cutting tool inserts....120

FESEM micrographs of the failed uncoated cutting tool inserts 125
Appendix G.....129
EDS results of the cutting chips.....129

List of Figures

Figure 2.1: Vickers hardness of cemented tungsten carbide (WC-Co) as a function of grain size and Co content [6]. 7
Figure 2.2: Ranking of coated and uncoated inserts for steel cutting[12]. 9
Figure 2.3: Implanted ions distribution [45]. 10
Figure 2.4: Tool life T dependence on cutting speed V using hard alloys Δ VK8 non-implanted, ○ VK8 ion implanted and ▼ BK8 implanted during machining titanium alloy VT22 [53].....12
Figure 2.5: Residual stress measurement carried out at different angles of incidence in TiN coating ion implanted with Mo [50]. 13
Figure 2.6: Wear rate of the TiN coating at different Mo ion implantation dosages[16]. 14
Figure 2.7: Variation of micro-hardness and wear loss TiN coatings at different Mo + C ion implantation dosages [15]. 15
Figure 2.8: A typical machine setup for vertical milling used for horizontal machining [62]. 16
Figure 2.9: Face milling mechanisms [30]. 16
Figure 2.10: Cross-sectional view of machining process showing the major angles involved in machining [65]. 17
Figure 2.11: (a) Shows the effect of depth of cut on tool wear rate [67], (b) shows the effect of cutting speed on the surface [66] and (c) shows the effect of feedrate and cutting speed on the tool life [12]. 18
Figure 2.12: Schematic diagram of the forces at the cutting tool insert and the chip interface [68] 19
Figure 2.13: Heat generating zones in orthogonal cutting [62]. 20
Figure 2.14: Cross sectional view of a machining process [30]. 21
Figure 2.15: SEM micrograph of a deformed WC-TaC-Co cemented carbide [70]. ..21
Figure 2.16: SEM micrograph showing crater wear on the rake face [70].....22
Figure 2.17: (a) SEM micrograph of a BUE formation on the cutting edge[72] and (b) effect of grain size and hardness on the flank wear rate [6]. 23
Figure 2.18: Abrasion of cemented carbide [70]. 24
Figure 2.19: Fracture on the cutting tool [73]. 25

Figure 2.20: Thermal fatigue cracks in cemented carbide tool after interrupted cutting of steel [32]. 25
Figure 3.1: Work flow outline of the research study. 27
Figure 3.2: Face milling inserts. 28
Figure 3.3: Bridgeport GX 1000 showing the machining setup. 29
Figure 3.4: Fully loaded cutter (a) top view and (b) side view. 30
Figure 3.5: Machining setup inside the Bridgeport GX 1000. 31
Figure 3.6: Positions on the cutting tool inserts where stress measurements were conducted. 39
Figure 3.7: Schematic representation of the RBS operation. 40
Figure 4.1: (a) FESEM micrograph of the cutting tool insert cross-section with the corresponding XRD pattern shown in (b). 42
Figure 4.2: FESEM micrograph of the H13 steel microstructure with the corresponding XRD pattern shown in (b). 44
Figure 4.3: FESEM micrograph of (a) non-implanted inserts and (b) insert with ion implantation dosage of 1E+17 ions/cm^2. 45
Figure 4.4: (a) FESEM micrograph of the cross-section, (b) corresponding EDS spectrum (c) FESEM micrograph of coating and (d) corresponding EDS spectrum of the insert with ion implantation dosage of 1E+17 ions/cm^2. 46
Figure 4.5: Elemental composition of the cross-section compared to that of the coating of the insert with ion implantation dosage of 1E+17 ions/cm^2. 47
Figure 4.6: Ru and Mo composition at different ion implantation dosages. 48
Figure 4.7: Elemental mapping of the cutting tool insert with ion implantation dosage of 1E+17 ions/cm^2 (a) FESEM micrograph of the scanned, and the elemental mapping of (b) tungsten (W), (c) cobalt (Co), (d) aluminium (Al), (e) titanium (Ti), (f) nitrogen (N), (g) molybdenum (Mo) and (h) ruthenium (Ru). 49
Figure 4.8 RBS of the coated cutting tool inserts implanted at an ion implantation dosage of 2E+16 ions/cm^2. 50
Figure 4.9: RBS results of the uncoated cutting tool inserts implanted at 2E+16 ions/cm^2 50
Figure 4.10 RBS of the coated cutting tool inserts implanted at ion implantation dosage of 2E+16 ions/cm^2 at 120 keV. 51
Figure 4.11: Vickers Micro-hardness of the Ru + Mo ion implanted cutting inserts at different ion implantation dosages. 52

Figure 4.12: AFM images of the coated cutting tool inserts showing surface at topography at different ion implantation dosage s (a) non-implanted, (b) 5E15, (c) 8E15, (d) 1E16, (e) 2E16 and (f) 1E17 ions/cm^2. 53
Figure 4.13: AFM images of the cutting tool inserts showing the surface morphology. (a) Non-implanted (b) ion implantation of 1E+16. 53
Figure 4.14: Average surface roughness at different Ru + Mo ion implantation. 54
Figure 4.15: Residual stresses of the Ru and Mo ion implanted coated cutting tool inserts. 55
Figure 4.16: X-ray diffraction pattern analysis of coated non-implanted cutting inserts. 56
Figure 4.17: X-ray diffraction pattern analysis of the coated cutting tool inserts implanted at 2E+16 ions/cm^2 dosage. 56
Figure 4.18: X-ray diffraction pattern analysis of the non-implanted uncoated cutting tool insert. 57
Figure 4.19:X-ray diffraction pattern analysis of the uncoated cutting tool inserts implanted at 2E+16 ions/cm^2. 57
Figure 4.20: XPS spectra of the surface layer of the non-implanted cutting tool insert. 58
Figure 4.21: XPS spectra of the surface layer of the Ru + Mo ion implanted cutting tool insert at implantation dosage of 2E+16 ions/cm^2 at 120 keV. 59
Figure 4.22: XPS spectra of the surface layer of the Ru + Mo ion implanted cutting tool insert at implantation dosage of 1E+17 ions/cm^2. 59
Figure 4.23: TOFSIMS results of the non-implanted cutting tool inserts. 60
Figure 4.24: TOFSIMS results of the cutting tool inserts implanted at an ion implantation dosage of the 5E+15 ions/cm^2. 61
Figure 4.25: TOFSIMS results of the cutting tool inserts implanted at an ion implantation dosage of 2E+16 ions/cm^2. 61
Figure 4.26: Induced cutting forces experienced by cutting tool inserts during machining. 62
Figure 4.27: Heat generated at the tool–workpiece interface during machining. 63
Figure 4.28: Flank wear (VB) of the coated cutting tool inserts. 64
Figure 4.29: Residual stress measurements in the coated inserts before and after machining. 65

Figure 4.30: (a) and (b) Failure mechanism experienced by the coated, (c) and (d) failure mechanisms experienced by the non-implanted uncoated cutting tool inserts on the rake face. 67
Figure 4.31: Failure mechanisms experienced by the coated ion implanted cutting tool inserts. 68
Figure 4.32: Failure mechanisms experienced by the uncoated ion implanted inserts. 69
Figure 4.33: GIXRD pattern using ion implantation dosage of 2E+16 ions/cm^2 (a) 100 and (b) 120 keV. 70
Figure 4.34:X-ray diffraction pattern (a) 5E+15, (b) 8E+15, (c) 1E+16 and (e) 1E+17 ions/cm^2.....71
Figure 4.35: Purple to dark blue cutting chips collected while using different coated cutting tool inserts (a) non-implanted, (b) 5E+15, (c) 8E+15, (d) 1E+16, (e)2E+16 and (f) 1E+17 ions/cm^2 at 100 keV. (f) 2E+16 ions/cm^2 at 120 keV. 73
Figure 4.36: Blue to purple cutting chips collected while using different uncoated cutting inserts (a) non-implanted, (b) 5E+15, (c) 8E+15, (d) 1E+16, (e)2E+16 and (f) 1E+17 ions/cm^2 at 100 keV. (f) 2E+16 ions/cm^2 at 120 keV, the circles show the jagged edges and the shear fronts. 74
Figure 4.37: Chip compression ratios of the cutting chips collected during machining. 75
Figure 4.38: X-ray diffraction pattern of the cutting using different cutting inserts as indicated on the graph. 75
Figure 4.39: FESEM micrographs of the cutting chips free surface of the coated cutting tool inserts (a) and (b) non-implanted, (c) 5E+15, (d) 8E+15, (e) 1E+16, (f)2E+16 and (h) 1E+17 ions/cm^2 at 100 keV. (g) 2E+16 ions/cm^2 at 120 keV. 76
Figure 4.40: FESEM micrographs of the cutting chips free surface of uncoated tool inserts (a) non-implanted, (b) 5E+15, (c) 8E+15, (d) 1E+16, (e)2E+16 ions/cm^2 at 100 keV and (f) 2E+16 ions/cm^2 at 120 keV. 77
Figure 4.41: Surface of the workpiece at different ion implantation dosages. 78
Figure 4.42: X-ray diffraction pattern of the workpiece machined surfaces. 79
Figure 4.43: FE-SEM micrographs of the machined workpiece using different cutting tool inserts (a) non-implanted, (b) 5E+15 , (c) 1E+16, (d) 2E+16 and (f) 1E+17 ions/cm^2 at 100 keV and (e) 2E+16 ions/cm^2 at 120 keV. 80

Figure 5.1: FESEM micrographs of the cross-section of the used coated cutting tool inserts (a) non-implanted, (b) 5E+15 , (c) 8E+15 (d) 1E+17 and (e) 2E+16 ions/cm^2 at 100 keV. 92
Figure 5.2: Oxygen wt.% in cutting chips. 93
Figure A.0.1: FESEM Micrographs of the ion implanted inserts (a) 5E+15 (b) 8E+15 (c) 1E+16 (d) 2E+16 ions/cm^2 at 100 keV and (e) 2E+16 ions/cm^2 at 120 keV. 107
Figure B.0.1: RBS of the uncoated tool inserts implanted (a) 5E+15, (b) 8E+15, (c) 1E+16, and (d) 2E+16 ions/cm^2 109
Figure B.0.2: RBS of the coated tool inserts implanted (a) 5E+15, (b) 8E+15, (c) 1E+16, and (d) 1E+17 ions/cm^2 110
Figure C.0.1 GIXRD results (a) 5E+15, (b) 8E+15, (c) 1E+16, (d) 2E+16-120 keV and (e) 1E+17 ions/cm^2 112
Figure C.0.2: GIXRD results (a) 5E+15, (b) 8E+15, (c) 1E+16 and (d) 2E+16-120 keV. 114
Figure D.0.1: TOFSIMS results (a) 8E+15, (b) 1E+16, (c) 2E+16-120 keV and (d) 1E+17 ions/cm^2. 116
Figure E.0.1: FESEM Micrographs showing flank wear on the coated implanted inserts (a) non-implanted (b) 5E+15 (c) 8E+15 (d) 1E+16 (e) 2E+16, (f) 2E+16-120 keV and (g) 1E+17 ions/cm^2 118
Figure E.0.2: FESEM Micrographs showing flank wear on the uncoated implanted inserts (a) non-implanted (b) 5E+15 (c) 8E+15 (d) 1E+16 (e) 2E+16, (f) 2E+16-120 keV ions/cm^2. 119
Figure F.0.1: Failure mechanisms of a set of non-implanted inserts on the rake face of the cutting inserts that were used at the same time. 120
Figure F.0.2: Failure mechanisms of the cutting tool inserts with ion implantation dosage 5E15 ions/cm^2 (a) and (c) on the rake face and (b, d-f) shows the cutting edge from flank face. 121
Figure F.0.3: Different failure mechanism of the rake face of the inserts implanted at 8E+15 ions/cm^2 dosage. 122
Figure F.0.4: Different failure mechanisms of the rake face of the cutting tool inserts implanted at 1E+16 ions/cm^2 dosage. 122
Figure F.0.5: Different failure mechanism of the rake face of the inserts implanted at 2E+16 ions/cm^2 at 100 keV. 123

Figure F.0.6: Different failure mechanism of the rake face of the cutting tool inserts implanted at 2E+16 ions/cm^2 at 120 keV. 124
Figure F.0.7: Different failure mechanisms of the rake face of the cutting tool inserts implanted at 1E+17 ions/cm^2 dosage. 125
Figure F.0.8: Failure mechanisms experienced by a set of non-implanted cutting inserts on the rake face. 126
Figure F.0.9: Failure mechanism experienced by a set of cutting inserts on the rake face implanted at 8E+15 ions/cm^2. 126
Figure F.0.10: Failure mechanisms experienced a set of cutting tool inserts on the rake face implanted at 1x10^{16} ions/cm^2 127
Figure F.0.11: Failure mechanisms experienced by a set of cutting tool inserts on the rake face 2E+16 ions/cm^2 at 100 keV 128
Figure F.0.12: Failure mechanisms of the cutting tool inserts implanted at 2E+16 ions/cm^2 -120 keV 128
Figure G.0.1: FESEM micrographs and the corresponding EDS analysis for the cutting chips (a) non-implanted, (b) 5E+15, (c) 8E+15, (d) 1E+16, (d) 2E+16 and (f) 1E+17 ions/cm^2 at 100 keV. 130

List of Tables

Table 3.1: Nominal composition of the tool steel. 28
Table 3.2: Ion implantation dosages (ions/cm^2). 29
Table 3.3: Face milling parameters. 30
Table 3.4: Sample preparation procedure. 34
Table 3.5: Composition of Murakami's solution [77]. 36
Table 4.1: Material properties of the uncoated inserts. 43
Table 5.1: Vickers micro-hardness % increase of the ion implanted cutting tool inserts compared to non-implanted cutting tool inserts 83
Table 5.2: Ion implantation time at different ion implantation dosages. 84
Table 5.3: Chemical states. 85
Table 5.4: Average Vickers micro-hardness comparison between coated and uncoated ion implanted inserts. 87
Table 6.1: Summary of the major results at different ion implantation dosages. 97

Chapter 1 Introduction

1.1 Background and motivation for research

The metal working industry requires high quality efficient cutting tools with increased wear resistance in order to meet the production demands for products with high dimensional accuracy and good surface finish [1, 2]. The quality, dimensional accuracy, net shape and integrity of machined surface are influenced by wear of the cutting tool inserts [1, 3]. Operational factors such as applied load, friction, cutting speed, and temperature at the cutting tool-workpiece interface influences the amount of wear experienced by the inserts during the machining process. Consequently inserts which have high hot hardness, high strength, moderate toughness and are chemically inert are desirable [4, 5]. Having a moderate toughness minimises fracturing and chipping during interrupted or intermittent cutting, while chemical inertness minimises diffusion wear and oxidation, especially at elevated temperatures and high cutting speeds [4, 6, 7].

Cemented tungsten carbides having cubic carbides titanium carbide (TiC), tantalum carbide (TaC) and niobium carbide (NbC) are generally used as cutting tool inserts as they meet the requirements mentioned above, and are known to have a high wear resistance [6, 8]. Tungsten carbide (WC) is hard and brittle, and cobalt (Co) is typically added as a metal binder to provide toughness; this combination provides the strength of the composite [9]. Cubic carbides such as TiC are added due to their high hardness and chemical stability at high temperatures, which also impart crater wear resistance [8]. However, the addition of TiC reduces the tool strength during cutting, which limits the tool's application to machining of lighter steels. The hot hardness of WC-Co is enhanced, without compromising strength, by grain refinement using chromium carbide (Cr_3C_2), and these tools are then known as a straight grade cutting inserts [6, 8].

The affinity between the workpiece and the cutting tools inserts when machining steel results in diffusion wear which causes premature failure of the inserts [10]. Therefore, the cutting inserts are typically coated with titanium nitride (TiN) and titanium aluminium nitride (TiAlN) hard coatings to reduce chemical diffusion, improve oxidation resistance and to ensure low thermal conductivity during machining [10].

The coatings also provide increased wear resistance at high cutting speeds, which increases the life span of the inserts and production rates [6, 10, 11]. During operation these coatings have been known to chip and/or delaminate when high cutting speeds are employed, and when machining under unlubricated conditions [3, 12, 13]. Therefore, it is of commercial interest to find methods which improve the properties of the coatings or to explore alternative methods of increasing the lifetimes of the tool inserts which do not employ the use of coatings. Additional benefits of increased tool lifetimes include reduced downtimes during industrial machining, and reduced production rates of new cutting tools, which also addresses the increasing resource depletion of tungsten [14].

A possible solution to improving the coating properties is to modify the surface of the coating using ion implantation. This technique has been shown to increase the wear resistance of TiN coatings when using different elements [11, 15–23]. For example, ion implantation of TiN coatings using Molybdenum (Mo) was initially employed to reduce friction, however ion implantation did not only reduce surface roughness, it also resulted in the formation molybdenum oxides which are known to be lubricious [16]. Research by Deng et al [15] showed that dual ion implantation of Mo + C into TiN coating increased hardness and resulted in the formation of the Mo magn'eli phase (lubricous layer). The formation of a magn'eli phase also address the drive towards cleaner and environmentally friendly machining processes by using self-lubricating cutting tools [22, 24, 25]. Ruthenium, a noble element metal known to increase wear and corrosion resistant cemented carbides [26], has a hexagonal structure, which is associated with low coefficient of friction [27]. Ion implantation of Ru into WO_3 resulted in structural densification and subsequently reduced porosity [28]. Therefore, this makes Ru a viable candidate for improving coating properties using ion implantation.

The current research study provides a systematic investigation into the application of Ru and Mo dual ion implantation into coated and uncoated cemented tungsten carbide inserts in order to increase lifespan and machining performance

1.2 Research Aim and Objectives

The main aim of this research was to increase the cutting tool life of WC-6wt%Co straightgrade inserts by reducing the wear experienced during face milling of H13 steel. This aim was achieved by assessing the feasibility of Ru and Mo dual ion implantation on coated and uncoated inserts. The research had the following objectives:

- Determining the optimum dosage of Ru and Mo dual ion implantation
- Characterising the microstructure of the ion implanted inserts
- Conducting face milling tests to assess the wear and failure mechanisms of the ion implanted inserts
- Comparing the properties of the ion implanted inserts to those of conventional inserts

1.3 Contribution to knowledge

There is minimal research on ion implantation using Ru to improve the surface properties of TiN coatings and cemented tungsten carbides and almost none on dual ion implantation of Ru and Mo. The outcome of this research will provide more applications for Ru in machining applications where wear resistance is of high importance. Ruthenium is a by-product during production of Platinum (Pt) and South Africa is a top producer of Ru [29]. Therefore, finding innovative methods of Ru applications will provide economic benefits as well as contribute to the intellectual property of the scientific community. Furthermore, the outcome of this study will provide fundamental background and vital information to stimulate further study on ion implantation using Ru to improve surface coatings.

1.4 Structure of the dissertation

This dissertation is structured in the following manner: Chapter 1 explains the significance of the research work. Chapter 2 provides detailed background on the properties of the WC-Co alloys which qualify them as the preferred material for

intermittent cutting and how they have been modified through coating and coating optimisation using techniques such as ion implantation to enhance their performance over the years. It also provides a general background of face milling and the failure mechanisms experienced during cutting. Chapter 3 describes the different experimental procedures used to investigate the effect of Ru and Mo dual ion implantation on the physical, mechanical and microstructural properties of the cutting tool inserts. It also describes the machining tests and analyses used to access the performance of the ion implanted cutting tool inserts when machining H13 steel. Chapter 4 presents the characterisation and machining performance results which are then discussed in Chapter 5. Chapters 6 and 7 provide the conclusions and recommendations for future work, respectively, followed by a list of the cited references.

Chapter 2 Literature Review

This chapter provides a review of published research work on the ion implantation of uncoated and coated WC-Co alloys. This chapter also discusses the properties of cemented carbides that are specific for cutting tools. It also gives a brief background on machining, types of tool failure mechanisms and ion implantation.

2.1 Cemented tungsten carbide tools

Cutting tool inserts made from cemented tungsten carbide (WC-Co) alloys are widely used to machine steels [30]. The WC-Co alloys are generally produced using powder metallurgy processes, which involves milling of the WC and Co powders, pressing and liquid phase sintering. Each processing stage is crucial as it influences the final microstructure and material properties of the alloy [6, 7]. The brittle WC phase provides the high hardness and associated high wear resistance, while the ductile Co binder matrix provides the toughness. The thermal expansion mismatch between WC and Co means that WC is in a compressive state and Co is in tension, which provides the strength of the carbide-binder composite [7].

A balance between hardness and fracture toughness for intermittent cutting process applications such as face-milling is crucial since both hardness and fracture toughness are equally important [31]. These mechanical properties are determined by the microstructural properties which include porosity, volume% of the WC and Co phases, mean WC grain size (d_{WC}), mean binder free path (λ_{Co}) and the distribution of the d_{WC} in the Co matrix. Figure 2.1 shows the relationship between d_{WC}, Co content and Vickers hardness. A d_{WC} below 0.5 µm and a Co content (volume%) of less than 10% achieves Vickers hardness of approximately (~) 2000 HV, while d_{WC} of ~ 5 µm with a Co content of plus 40% result in Vickers hardness of ~ 800 HV. The graph shows a linear effect of d_{WC} and the Co content on Vickers hardness [6, 31].

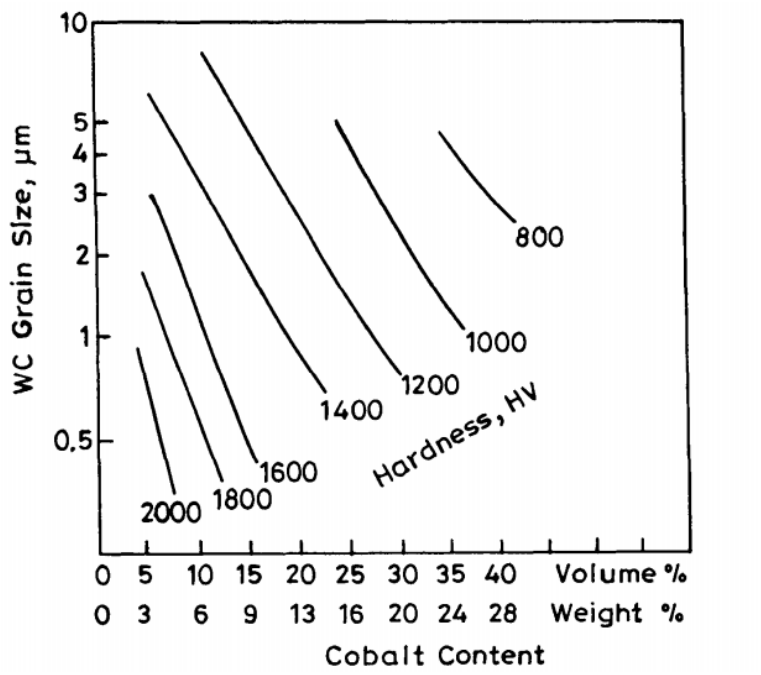


Figure 2.1: Vickers hardness of cemented tungsten carbide (WC-Co) as a function of grain size and Co content [6].

The WC-Co alloys have a hexagonal structure which restricts major structural changes when the temperature increases, thereby retaining a high hot hardness unlike steel alloys, which are mostly cubic and known to become ductile and experience a decrease in hardness as the temperature increases [32]. Due to this ductile nature of steel during machining steel, cutting chips tend to weld onto the WC-Co cutting tool inserts [6]. The strong chemical affinity between the iron (Fe) in the steel and the carbon (C) in the inserts at the elevated machining temperatures results in diffusion wear and chemical reactions at the tool-chip interface causing premature tool failure [6, 33].

To combat these problems refractory or cubic carbides (TiC, TaC and NbC) were added to the WC-Co alloys, which greatly improved the performance of the cutting tool inserts by reducing diffusion wear and plastic deformation [4, 12]. These tools are known as tool grade cemented tungsten carbides. Titanium carbide (TiC) is added to reduce the welding tendency of cutting chips or swarf onto the cutting tool inserts [32, 34], however, these alloys tend to loose strength with increasing temperature [6, 32]. Research has shown that the addition of Cr_3C_2 instead of the aforementioned cubic carbides, inhibits WC grain growth, which increases the hot hardness without compromising the strength [6]. These WC-Co alloys are known as straightgrade

cutting tool inserts; however these inserts are still susceptible to diffusion wear [6]. The success in manufacturing wear resistant steel case watches by coating the cases with hard materials resulted in the introduction of coatings on the cutting tool inserts using chemical vapour deposition (CVD); physical vapour deposition (PVD) was developed 9 years later [6, 32]. These coatings have also been shown to address the chemical diffusion problem[6].

Chemical and physical vapour deposition coatings are generally applied to inserts used in machining operations [12]. Chemical vapour deposition is used to produce thick coatings which are often used for turning applications while the PVD technique is used for the production of thin coatings, which are often used for milling applications because of sharp cutting edges and residual stresses [10]. Typical coatings used are TiN, TiAlN, TiC and Al_2O_3 [10]. These coatings are deposited by either CVD or PVD with coating thicknesses limited between 1 and 10 microns because thicker layers tend to be brittle [6, 11]. The TiAlN coating is only deposited using the PVD technique [10]. The type of coating selected is based on their high-temperature stability, fracture toughness, low coefficient of friction, hot hardness, oxidation and corrosion resistance [3, 10, 12, 13, 15, 35–37]. Coated carbides have the following advantages over uncoated carbides during machining operation [6]:

- Higher cuttings speeds providing higher metal removal rates
- Higher wear resistance
- Higher chemical stability of the coated layer compounds
- Reduced machine downtime due to fewer tool change intervals
- Improved surface quality.

Coating of WC-Co cutting tool inserts has proven to increase the tool life by reducing certain failure mechanisms such as attrition, abrasion, diffusion and thermal fatigue [10, 12]. Delamination and/or chipping of the coatings have been shown to occur during machining, however coated inserts still result in longer tool lifespans than uncoated inserts [6, 12] as shown in Figure 2.2. The figure shows the enhancement factor of different cutting tools when machining steel. The enhancement factor is based on tool life, high enhancement represent longer tool life over that of the uncoated cutting tool; C5 is the uncoated cutting tool, ZrN, TiN and TiAlN are the coatings of the cutting tools [12]. Therefore research to optimise coating performance

has been on going, and has included optimising the deposition parameters for specific techniques, addition of alloying elements, optimising the grain orientation of the coating, manipulating the composition of the coating and ion implantation [15, 16, 18, 18, 21, 23, 38–44]. As ion implantation is the focus of the current research study a review of the technique and its application to cemented carbides is provided in the next session.

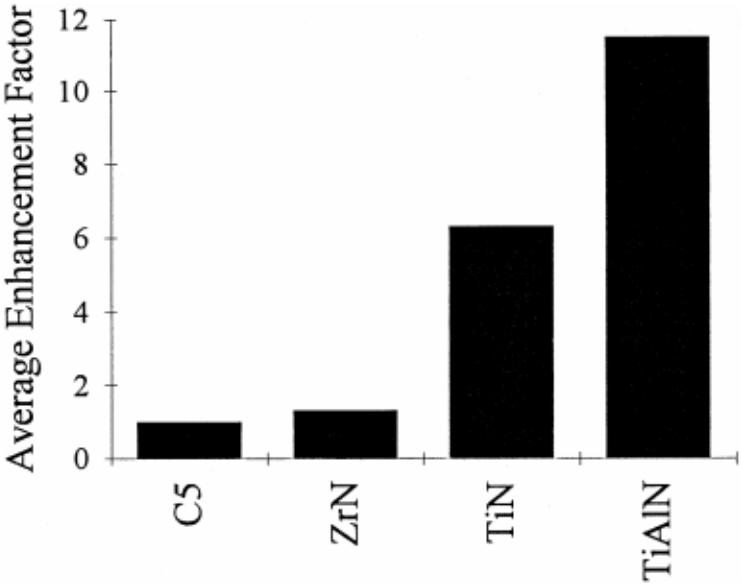


Figure 2.2: Ranking of coated and uncoated inserts for steel cutting[12].

2.2 Ion implantation

During ion implantation electrostatically charged particles of a specific atomic mass are accelerated by an applied electric force and then focused so that they strike a target. Upon reaching the target surface, the ions either bounce off or penetrate through the surface. The ions continue moving within the surface until their energy drops to below 20 eV where it is stopped by cohesive forces. The energetic ions travel through the solid and loose energy as a result of elastic collision with the target's atoms. This mechanism determines the ion range, which is the depth of ion penetration. Figure 2.3 shows a typical normal distribution of ions during ion implantation of an amorphous substrate.

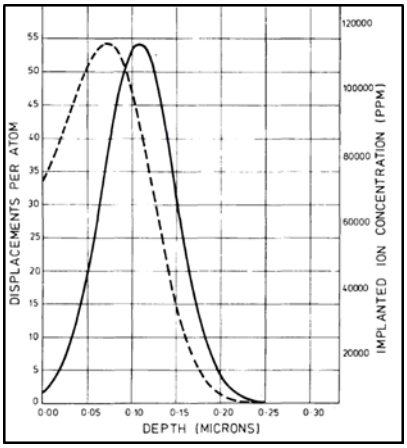


Figure 2.3: Implanted ions distribution [45].

Energy transfer during ion implantation causes dislocation, which results in strain hardening, thereby improving hardness [45–48]. The atoms that penetrate through the surface either occupy interstitial lattice or the lattice points. However, these implanted ions sometimes knock off main structure lattice atoms (sputtering) resulting in surface roughness increase. When the atoms occupy the interstitial lattice it results in swelling of the structure and that increases compressive stresses, which close micro-voids and stop propagation of cracks, and improve fatigue resistance [49, 50]. The increase in compressive stresses is also attributed to the surface amorphization. The effect of ion implantation reaches beyond the ion implanted zone due to a long range effect [46, 51]. Prolonged ion implantation might result in hardness reduction due to the critical dosage effect and sputtering process which is the ejection of surface atoms due to collisional energy transfers [11, 52]. Therefore it is important to control the dosage and implantation time. Ion implantation has the following advantages [11, 45, 46]:

- Solid solubility can be exceeded
- Can be applied to finished components with no significant dimensional change
- No sacrifice of bulk properties
- Low temperature process
- No adhesion problem since there is a sharp interface
- Depth concentration distribution is controllable
- Clean vacuum process
- Highly controllable and reproducible

- Low power consumption
- Conserves materials
- No toxicity

2.2.1 Ion implantation of uncoated and coated WC-Co

The continuous concentration profile grades of implanted ions with no definable interface which can be subjected to mechanical weaknesses or interfacial corrosion made ion implantation attractive for improving wear and corrosion resistance [41]. The reports on improvement of surface properties resulting from ion implantation, which led to improved wear resistance when using nitrogen (N), carbon (C) and argon (Ar) on cemented tungsten carbides, recorded a 30% increase in micro-hardness [47]. As also discussed in section 2.1 the importance of wear resistance in cemented tungsten carbide cutting tools, it became of interest to explore the applications of ion implantation in the cemented tungsten carbide cutting tools, which is supported by the research conducted in ion implantation since the 90s [19, 22, 51, 53, 54].

Turning test conducted using hard alloys cutting tool ion implanted with various elements such boron (B), carbon (C), nitrogen (N), aluminium (Al), titanium (Ti) and molybdenum (Mo) showed an increase in tool life by a factor of 4 [53] as shown in Figure 2.4.The hard alloys VK8 and BK8 in Figure 2.4 were ion implanted with W + Ar and Al + N respectively. The figure shows that tool life decreased with cutting speeds, since increasing cutting speed increase heat generated therefore softening of the workpiece. However, the ion implanted cutting tools were superior to the non-implanted tools. This was due to hardness increase in ion implanted cutting tools from formation of high strength compounds such as boron nitrides, surface roughness reduction and increase of residual compressive strain which increased the fatigue resistance of the cutting tools [53]. The improvement of material properties still depends on the target material, implanted ions and ion implantation parameters [55].

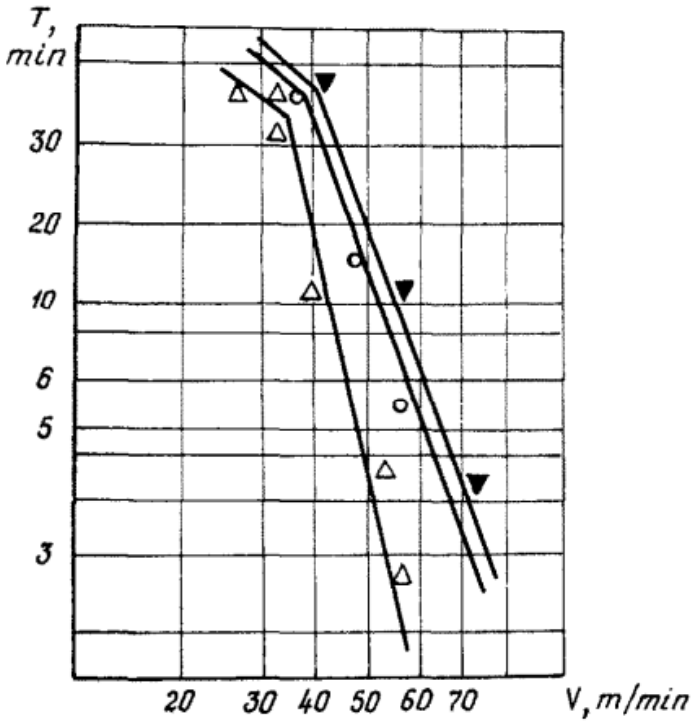


Figure 2.4: Tool life T dependence on cutting speed V using hard alloys Δ VK8 non-implanted, ○ VK8 ion implanted and ▼ BK8 implanted during machining titanium alloy VT22 [53].

However, machining of steel using cemented tungsten carbides requires the cutting tool inserts be coated using hard coatings due to the chemical affinity between the steel and the cutting tool as discussed in section 2.1. Titanium nitride (TiN) hard coatings with minor modifications are the commonly used coatings in the machining industry [6, 12, 17, 38, 40, 41, 56–59]. Studies have shown that ion implantation of TiN using metal and gas ions increase the tool life of coated cutting tools [52]. Ion implantation of TiN coatings using yttrium (Y), Mo, W, Al and Cr resulted in an increase in the compressive stresses, although compressive stresses were high closer to the surface as shown in Figure 2.5; compressive stresses decrease with increasing angle of incidence [50]. However, the structural compaction from implantation resulted in improved impact resistance. This shows that the benefits of ion implantation are beyond the ion affected zone as discussed by Townsend et al. and Manory et al. [46, 51].

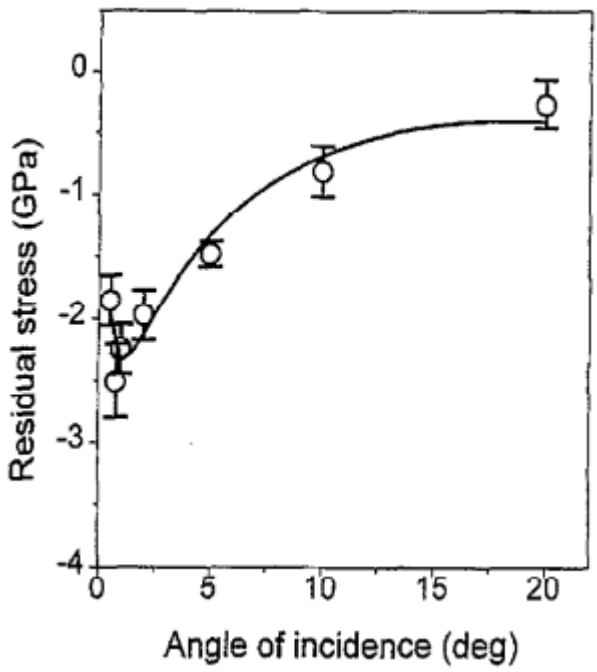


Figure 2.5: Residual stress measurement carried out at different angles of incidence in TiN coating ion implanted with Mo [50].

Ion implantation of Mo into TiN coating reduced surface roughness of the coating, subsequently reducing friction [16]. The coating was implanted using ion implantation dosages of 3E+17 and 1E+18 ions/cm^2 which resulted in the formation of titanium and molybdenum oxides, this resulted in hardness decrease as molybdenum oxides are soft. However, the surface roughness decreased, which subsequently resulted in low wear rate (Figure 2.6) during sliding wear tests. Figure 2.6 shows the wear rate of non-implanted TiN coating and TiN coating implanted at 3E+17 and 1E+18 ions/cm^2. The wear rate of a TiN coating implanted at 3E+17 was 31.38% lower than that of a non-implanted TiN coating, while the wear rate of the TiN coating implanted at 1E+18 ions/cm^2 was 35.48% lower.

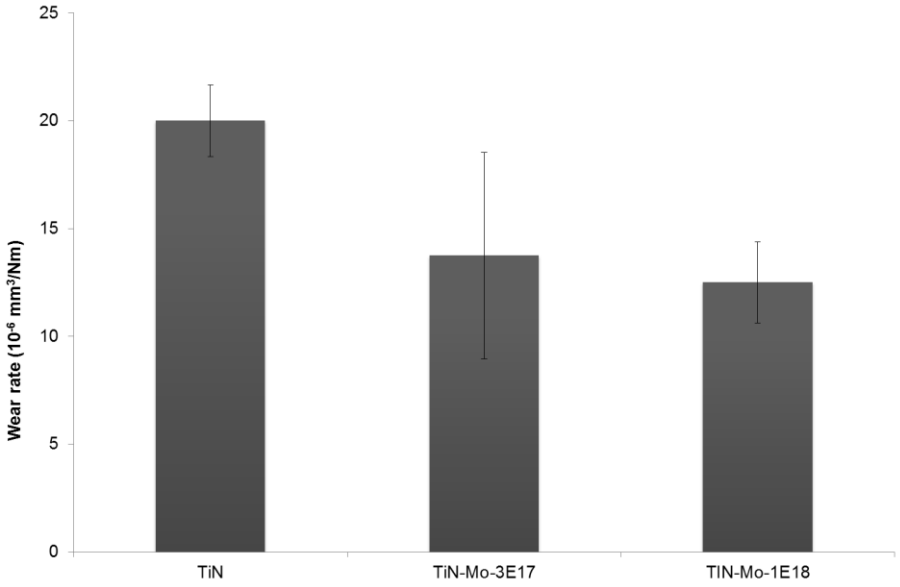


Figure 2.6: Wear rate of the TiN coating at different Mo ion implantation dosages[16].

Although the Mo ion implantation into TiN coating resulted in formation of soft Mo and M_xO_y compounds, which reduced the micro-hardness, dual ion implanting Mo + C resulted in 17% increase in micro-hardness of the coating without compromising the surface smoothness and the formation of the Molybdenum oxides [15]. The dual ion implantation resulted in hardness increase and decrease in wear loss during SRV friction and wear test as shown in Figure 2.7. This can be attributed to self-lubricating effect of molybdenum oxides and sulphides as they are known to be magn'eli. Figure 2.7 shows that a 13% hardness increase was achieved for the ion implanted TiN coating at the ion implantation dosage of 9E+16 ions/cm^2,which was the lowest ion implantation dosage, while at the same dosage an 11% wear loss was achieved.

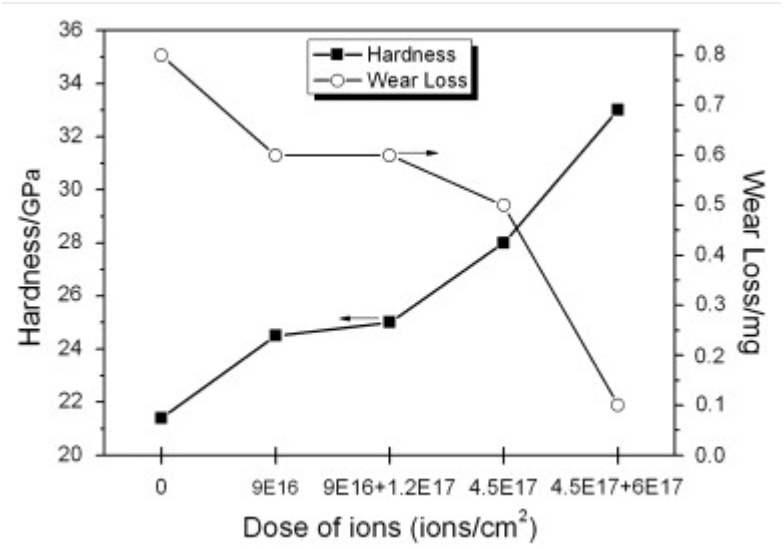


Figure 2.7: Variation of micro-hardness and wear loss TiN coatings at different Mo + C ion implantation dosages [15].

Ion implantation of ruthenium (Ru) has shown to reduce porosity and surface roughness when implanted into WO_3 [28] and there is minimal, almost none research published on the effect of dual ion implantation of Ru + Mo. The majority of the work done on WC-alloys and TiN coatings has focused on the characterisation of the ion implanted surfaces, with minimal focus on machining performance [17–19, 21, 23, 47, 60]. The limited machining tests (turning, grooving and end milling) conducted to date on metal ion implanted cemented carbide tools have shown an increase in tool lifespan, and an increase in production rates where the cutting speeds and feed rates could be increased by up to 50% [19, 54]. The machining performance tests conducted using ion implanted cutting inserts, thus far has had a minimum focus on face milling.

2.3 Milling

Milling is a machining process where the cutting operation is achieved by rotating a multipoint cutter while the workpiece is held stationery using a clamping vice as shown in Figure 2.8 [61]. The cutting tool insert is held by a cutter, which is available in a range of geometries tailored for different applications. The cutter rotation axis is perpendicular to that of the feed [30, 32, 61, 62].

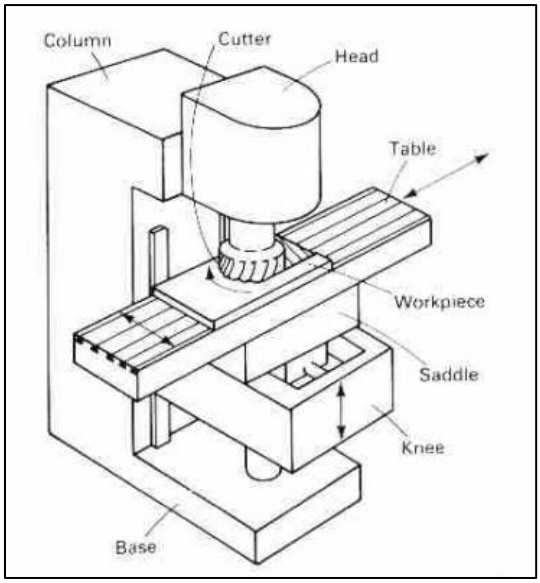


Figure 2.8: A typical machine setup for vertical milling used for horizontal machining [62].

During milling a new surface is generated as each tooth (i.e. the cutting edge of the insert) cuts away an arc-shaped segment, where the feed is usually not greater than 0.25 mm per tooth [30]. The action of each cutting edge is intermittent; each tooth cuts during half of a revolution of the cutter. Each cutting edge is subjected to impact as it comes into contact with the work piece, and machining is performed by cutting edges on both the end and outside of periphery of the cutter [63] as shown in Figure 2.9. The cutting edge is frequently stressed and heated during the cutting cycle, which result in thermal stress fatigue and subsequently tool failure [32].

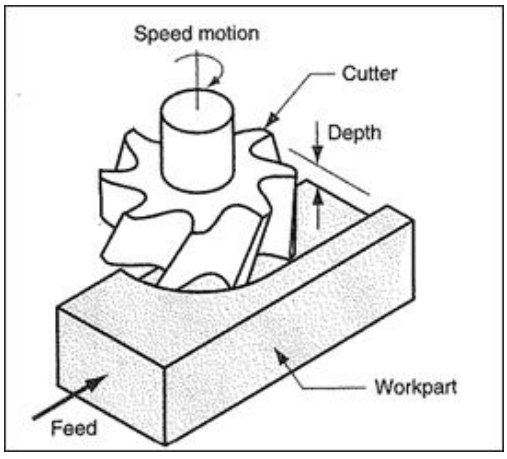


Figure 2.9: Face milling mechanisms [30].

There are three major angles, which are involved in the cutting operation, namely radial rake, axial rake and relief angle [64] as shown in Figure 2.10. The axial and

radial angle determine both the cutting energy applied to the shear zone and how the chip is removed from the cutting zone and the relief angle is the orientation of the flank surface and the flank which provides the clearance between cutting tool and the generated surface thus protecting it from abrasion [64].

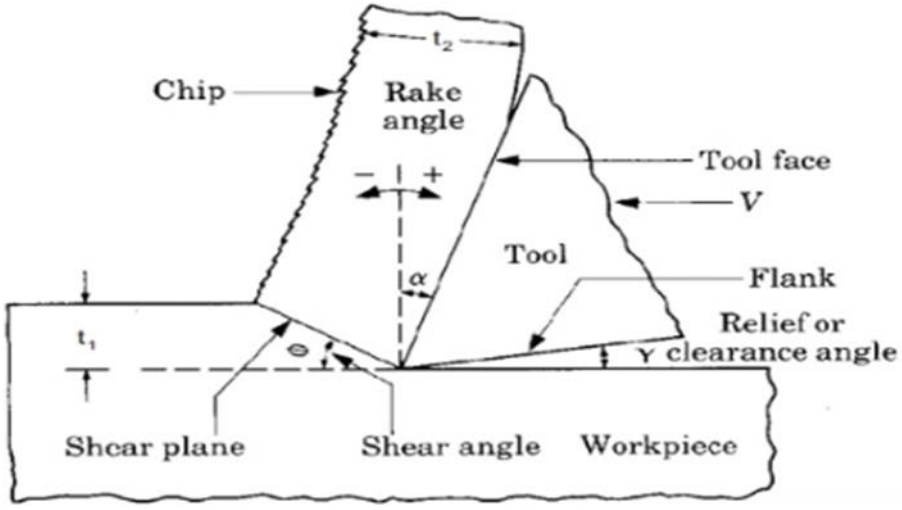


Figure 2.10: Cross-sectional view of machining process showing the major angles involved in machining [65].

Machining performance is influenced by cutting speed, feed rate and depth of cut [30]. Depth of cut has been shown to have minimal impact on machining performance, while feed rate and cutting speed control the tool lifespan (refer to Figure 2.11) and surface roughness respectively as they influence the heat generated at the cutting tool-chip interface and the induced cutting forces [12, 66]. An increase in depth of cut does not change average contact temperature and contact stresses at cutting tool-chip interface as the feedrate remain the same [67]. Figure 2.11 (a) shows the effect of the depth of cut in tool wear rate, as the depth of cut is varied while cutting speed and feed rate are kept constant, the graphs show that depth of cut have minimal effect on the tool wear rate. Figure 2.11 (b) is the surface roughness at varying cutting speed and the graph clearly shows that surface roughness decreases with increasing cutting speed for both down milling and up milling. Finally, Figure 2.11 (c) shows the effect of cutting speed and feedrate on the tool life (m) measured by the length cut, the wear rate increases with both cutting speed and feedrate. In order to obtain optimum machining performance, it is important to select the optimum cutting speed, feedrate and the depth of cut [12, 66, 67].

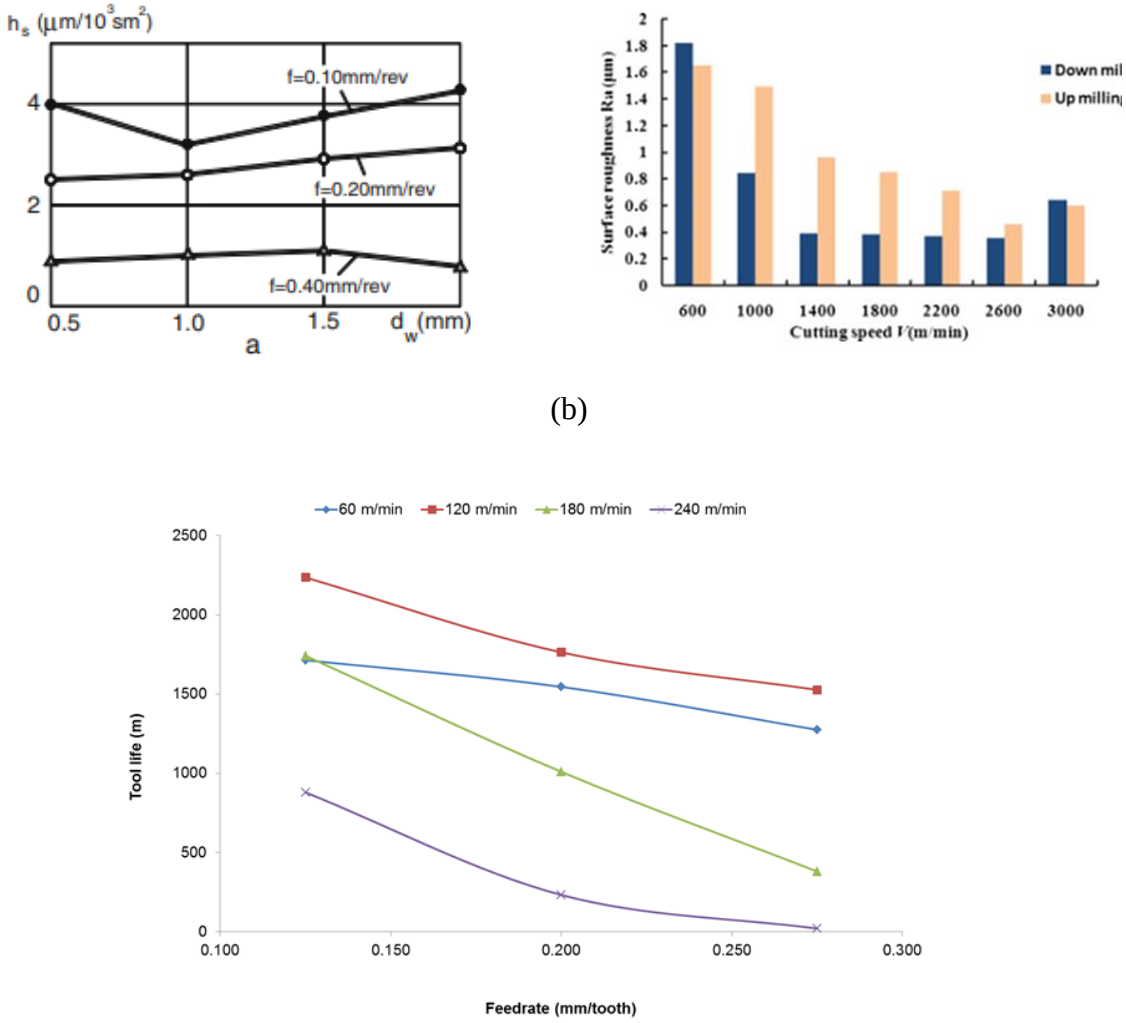


Figure 2.11: (a) Shows the effect of depth of cut on tool wear rate [67], (b) shows the effect of cutting speed on the surface [66] and (c) shows the effect of feedrate and cutting speed on the tool life [12].

The forces induced during orthogonal cutting when deforming and shearing away material in a form of a chip are shown in Figure 2.12. These forces are cutting force (F), thrust force (F_c), friction force (F_t), normal force (N), shear force (F_s) and normal force to shear (F_n). Only (F) and (F_c) can be measured because of direction they are applied. Cutting force (F) is in the direction of cutting speed and Fc is perpendicular to F, while the direction of the other forces F_t, N, F_s and F_n vary with tool geometry and machining conditions. Friction force (F_t) is the frictional force resisting cutting chip flow along the rake face, Fs causes shear deformation on the shear plane and F is the force on the rake face of the cutting tool [30, 32].

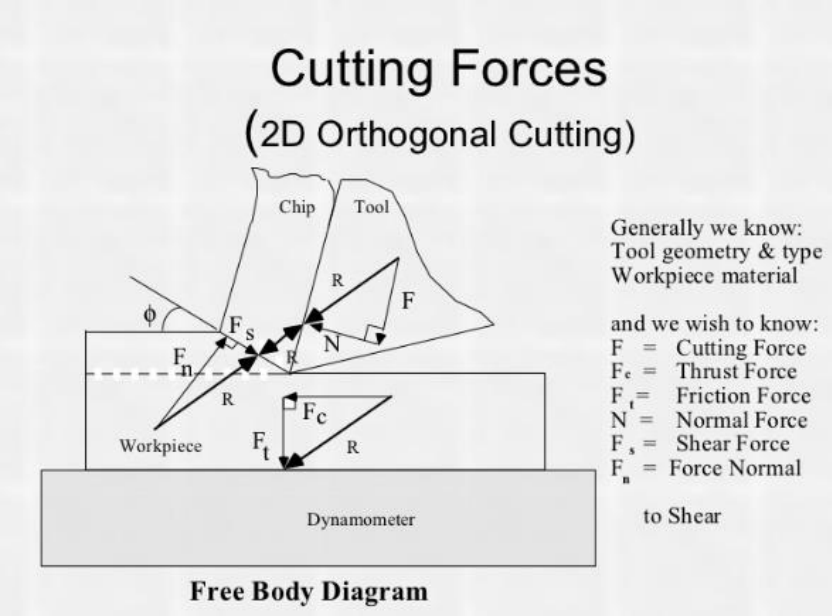


Figure 2.12: Schematic diagram of the forces at the cutting tool insert and the chip interface [68] .

Approximately 98% of the energy used during machining is converted into heat; this heat can increase the temperature at the tool-chip interface [30]. This heat, to a certain degree, contributes to technical and economic difficulties experienced during machining such as reduced tool life and poor dimensional accuracy [30, 32, 62]. Conversion of the energy into heat occurs in two regions, namely a shear zone or primary deformation zone (tool-workpiece interface) and a secondary deformation zone (tool-chip interface) as shown in Figure 2.13. Primary deformation zone is the area where the crystal structure of a metal breaks during shearing of chips and the secondary deformation zone friction heat generated when cutting chip sliding along rake face [69].

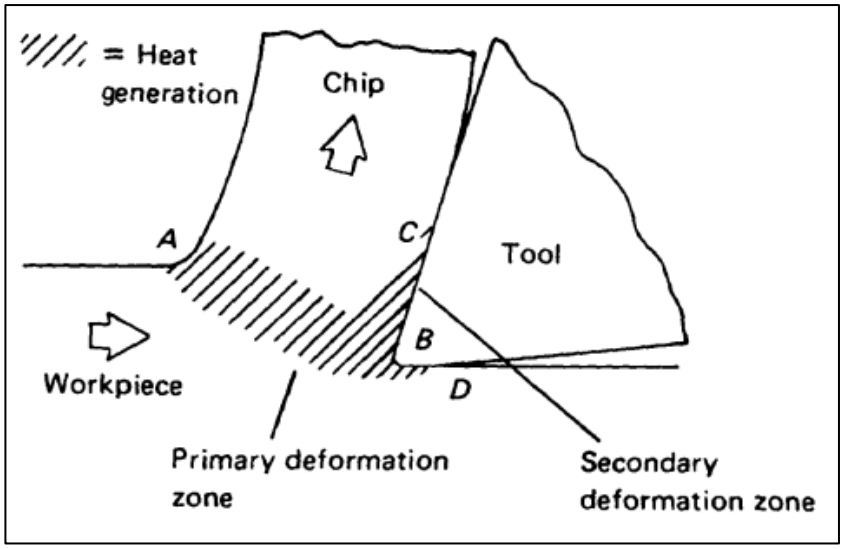


Figure 2.13: Heat generating zones in orthogonal cutting [62].

2.4 Failure mechanisms of WC-Co tools

Cutting tool life is crucial to the economics of the metal cutting industry as it is directly related to production rates [30]. Tool life is influenced by the induced forces, generated heat, operation method, tool geometry and interaction at the tool-chip interface [30, 32]. Research studies conducted over the years on cutting tool geometry, machine tool construction and operation methodology have led to efficiency of the cutting tool inserts and a decrease in premature tool failure [30]. As the cutting tool gradually changes various failure mechanisms may occur which are mainly dependent on the cutting tool microstructure and mechanical properties [30, 32, 62]. These types of failure are generally observed on the rake face, flank face, tool nose or on the cutting edge of the cutting tool inserts as indicated in Figure 2.14, which shows how the tool interacts with the workpiece during the cutting process [30]. Common failure mechanisms both gradual and progressive include deformation, diffusion wear, attrition wear, abrasive wear, fracture and thermal fatigue [6, 32, 70]. A brief review of each mechanism is provided in sections 2.4.1 to 2.4.6.

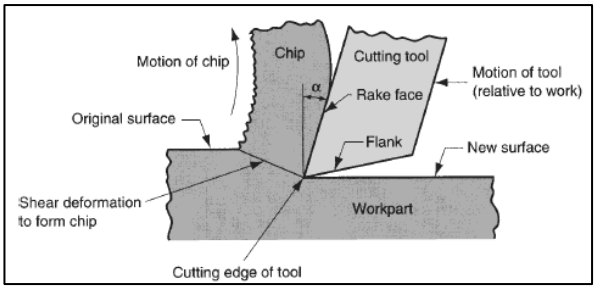


Figure 2.14: Cross sectional view of a machining process [30].

2.4.1 Deformation

High hot strength protects the cutting tool from abrasion wear due to superficial plastic deformation [30, 32]. This deformation, which occurs on the rake face as a result of compressive stresses, limits material removal therefore reducing production rates [32]. Failure due to deformation often occurs at high feed rates when the workpiece has a high hardness. Cemented carbides with low Co contents are used for high cutting speeds because of their high resistance to deformation [6]. However as the tungsten carbides can only handle limited deformation, cracks still form at high temperatures and this may lead to sudden fracture [32]. Plastic deformation due to compressive forces on the tool edge is characterised by the absence of porosity in the failed region as compared to the bulk region as shown in Figure 2.15 [70].

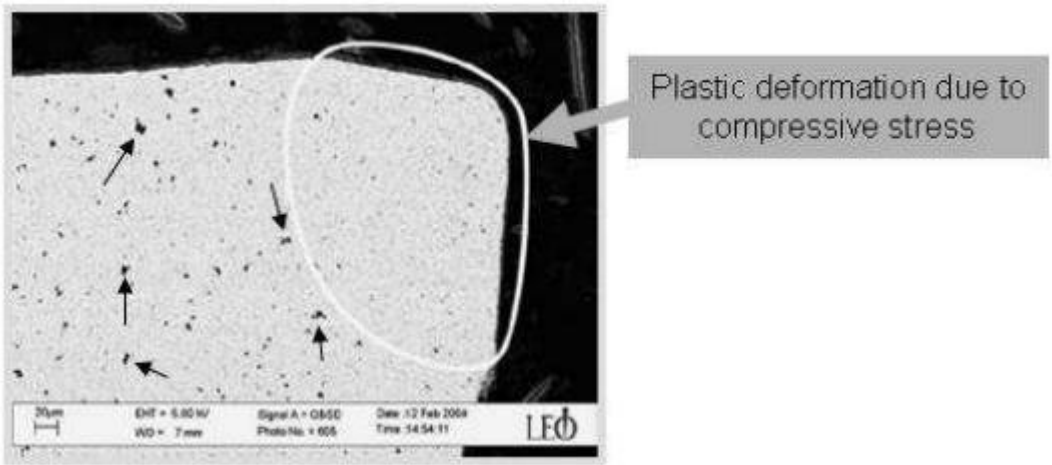


Figure 2.15: SEM micrograph of a deformed WC-TaC-Co cemented carbide [70].

2.4.2 Diffusion wear

Diffusion wear occurs when machining steel at high cutting speeds and high feed rates [32]. It is characterised by crater wear on the rake face of the tool, which is a smooth surface as shown in Figure 2.16. It is the result of a high interface temperature and chemical affinity between the cutting tool and the workpiece which causes diffusion of atoms from the tool into the workpiece which has seized on the rake face [32, 71]. Cobalt diffuses into the steel and iron (Fe) diffuses into the cutting tool, although the tool tends to remain intact since Fe provides similar cementing capabilities as Co. However, it is the diffusion of WC out of the cutting tool, which results in tool failure. The rate of WC diffusion is dependent on the cutting speed and feed rate. Therefore the rate of wear is as much dependent on chemical properties as on the mechanical strength or hardness of the tool [6, 32, 71].

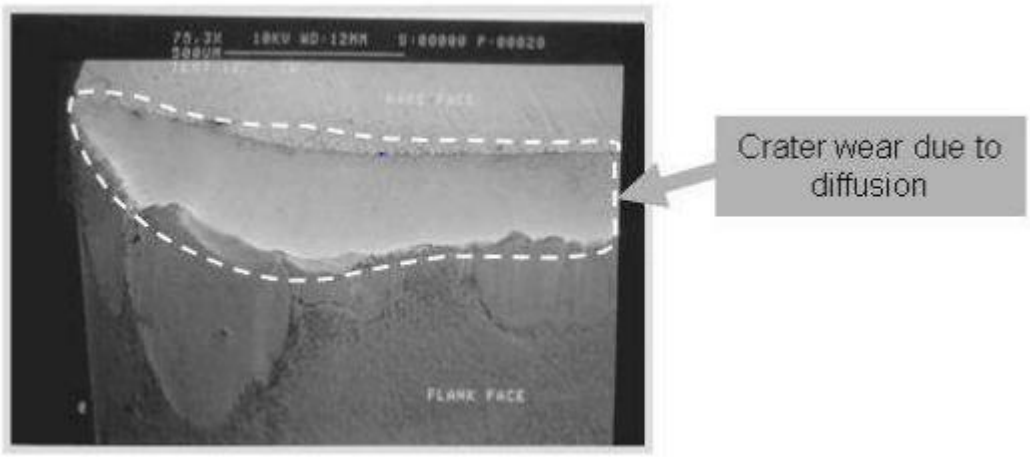


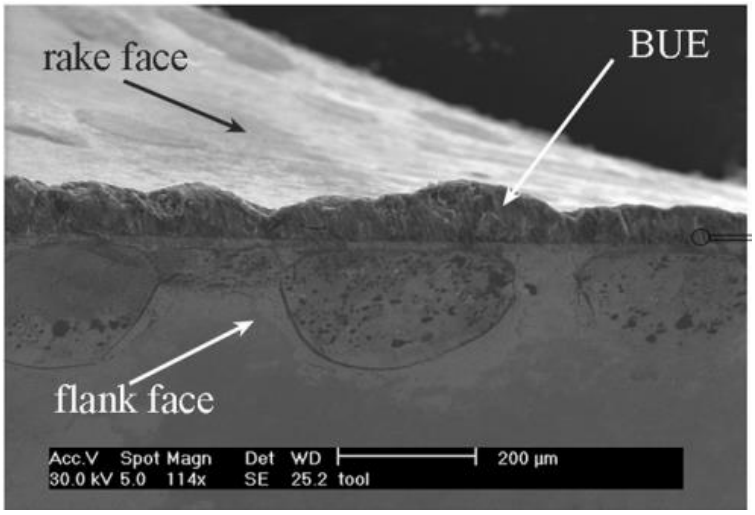
Figure 2.16: SEM micrograph showing crater wear on the rake face [70]

2.4.3 Attrition wear

Attrition wear occurs at low cutting speeds due to irregular flow of material at the tool's cutting edge [32]. Microscopic sized fragments of the tool material are torn from the tool edge. It is characterised by the formation of a built-up-edge (BUE) on the flank face as shown in Figure 2.17 (a). The BUE is often firmly bonded onto the cutting tool, and when chipped off, it often breaks away with a large portion of the tool [32]. The wear rate is directly related to the WC grain size, for example a fine grained high Co cemented carbide of 1265 HV can show better wear resistance than a

coarse grained hardmetal with low Co and a hardness of 1600 HV [6, 32] as indicated by Figure 2.17 (b).

(a)



(b)

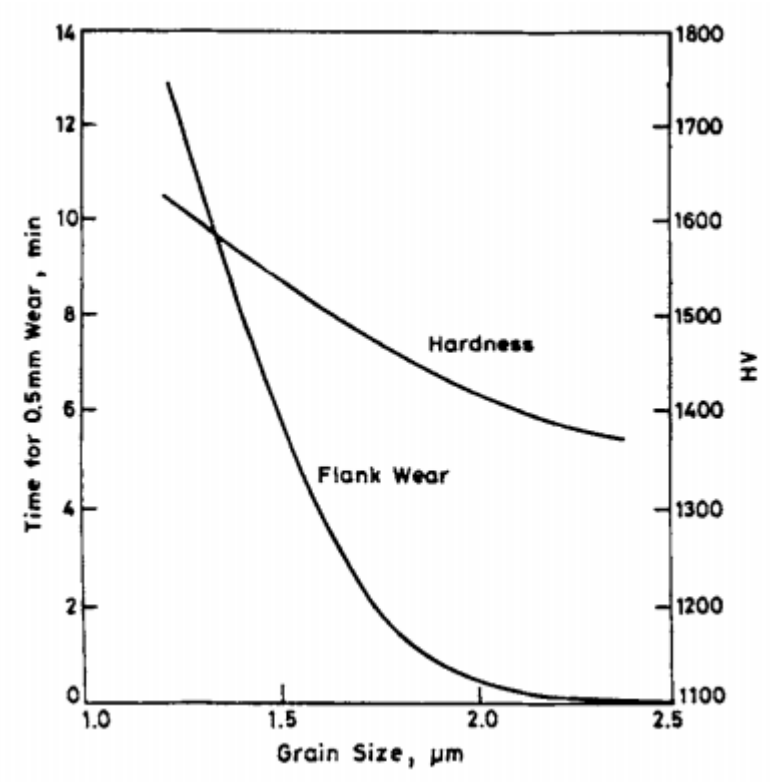


Figure 2.17: (a) SEM micrograph of a BUE formation on the cutting edge[72] and (b) effect of grain size and hardness on the flank wear rate [6].

2.4.4 Abrasive wear

Abrasive wear occurs when hard particles rub across the surface of the tool and occurs with work pieces containing hard particles like nitrides, carbides and oxides [71]. For example a particle harder than the cutting tool will cut grooves or craters larger than the individual carbide grains of the cutting tool, resulting in material removal by gross plastic deformation, which causes severe fragmentation on the surface as shown in Figure 2.18. Similarly, soft particles cause gradual extrusion of the Co binder, eventually removing it. A microstructural parameter that controls abrasive wear is the binder mean free path, subsequently the larger the mean binder free path, the higher the chances of the abrasive particles abrading the binder region. A low Co content also reduces abrasive wear because of the increased hardness [6].

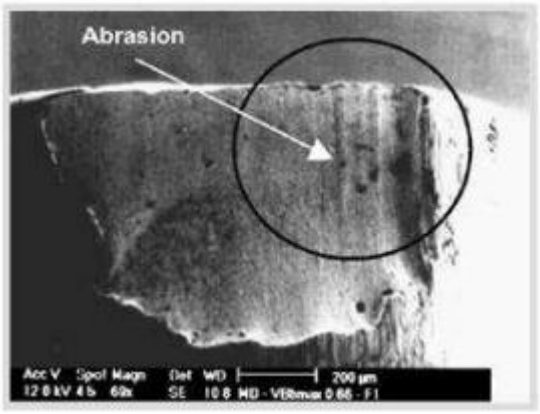


Figure 2.18: Abrasion of cemented carbide [70].

2.4.5 Fracture

Fracture is typically characterised by an erratic tool life (sudden failure) and generally occurs at the beginning of the cutting process when the cutting edge comes across a shoulder and fully engages on the workpiece [32]. In interrupted cutting operations such as milling, fracture is a result of mechanical fatigue [32]. Fracture occurs on the tool edge which is not engaged in cutting and is caused by chips curling back onto the edge or entailing the tool. Fracture may also be caused by deformation of the tool with mechanical fracture being the final state. It is minimised by preventing deformation through low %Co cemented carbides, and changing the tool geometry and operation method [32, 71].

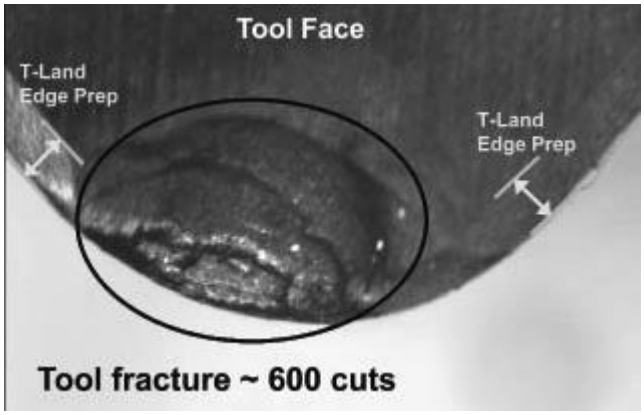


Figure 2.19: Fracture on the cutting tool [73].

2.4.6 Thermal fatigue

During interrupted cutting numerous short cracks perpendicular to the cutting edge are often seen, which are due to expansion and contraction of the surface layer of the cutting tool [32]. The cracks initiate from the hottest region of the rake face and may join and cause small fragments of the tool edge to break away. They may act as stress raisers leading to fracture initiation. Manufacturing cutting tools with a composition and structure less sensitive to thermal fatigue may help reduce thermal fatigue [26, 63].

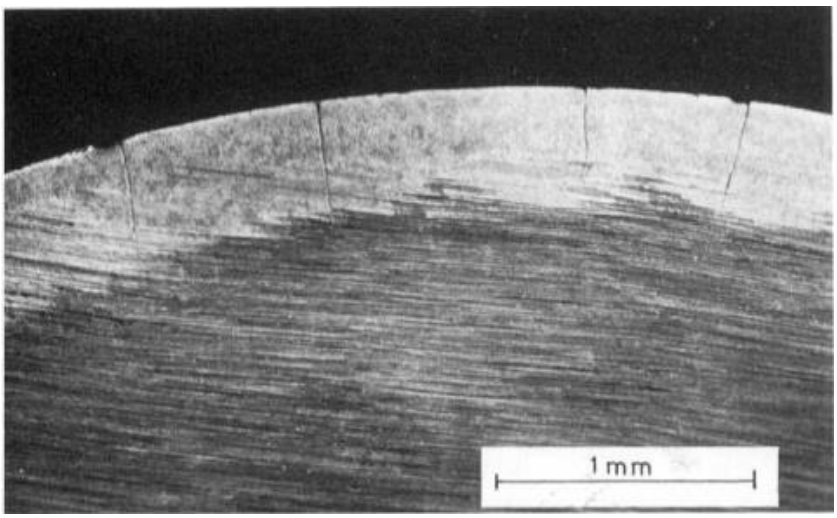


Figure 2.20: Thermal fatigue cracks in cemented carbide tool after interrupted cutting of steel [32].

2.5 Literature Review Summary

- Addition of Cr_3C_2 in WC-Co inhibits grain growth and improves hot hardness of the cutting tool inserts.
- These inserts are coated with hard coatings such as TiN, TiAlN, TiC and Al_2O_3 to reduce diffusion wear during machining of steel. However, these coatings are still susceptible to chipping and delamination at high cutting speeds.
- Ongoing research to improve coatings has been focusing on optimising coating deposition parameters, manipulation of the coating composition and ion implantation.
- Ion implantation of TiN using Y, Mo, W, Al, Nb and Cr has shown to increase wear resistance subsequently increasing the tool life.
- Single ion implantation of Mo reduces surface roughness which resulted in low wear rate during sliding wear tests. However, due to the formation of soft molybdenum oxides, hardness is reduced, which limits application where hardness is not crucial.
- Dual ion implantation of Mo and C resulted in 13% hardness increase and surface roughness reduction through the formation of molybdenum oxide, subsequently decreasing wear rate during SRV friction and wear test by at least 11%.
- Ion implantation of Ru into WO_3 resulted in reduced porosity and surface roughness. Thus far, there is no published research on the effect of dual implantation of Ru and Mo.
- The majority of the published research on the ion implantation of TiN has been focused on characterisation of the ion implanted surfaces with minimal focus on machining. The limited research on machining performance tests has a minimal focus on face milling.
- The machining performance as a measure of cutting tool insert wear rate and surface roughness of the machined surface during machining is affected by feedrate and cutting speed. Feedrate and cutting speed influence both heat generated at the cutting tool-chip interface and induced cutting forces.

Chapter 3 Experimental Procedures

This chapter describes the experimental procedures used to investigate the machining performance of Ru + Mo ion implanted cemented tungsten carbides cutting inserts when face-milling H13 tool steel. The different techniques used to determine the physical, mechanical and microstructural properties that influence the machining performance of the cutting tool inserts are also described. Figure 3.1 shows the work flow outline that was followed during the project.

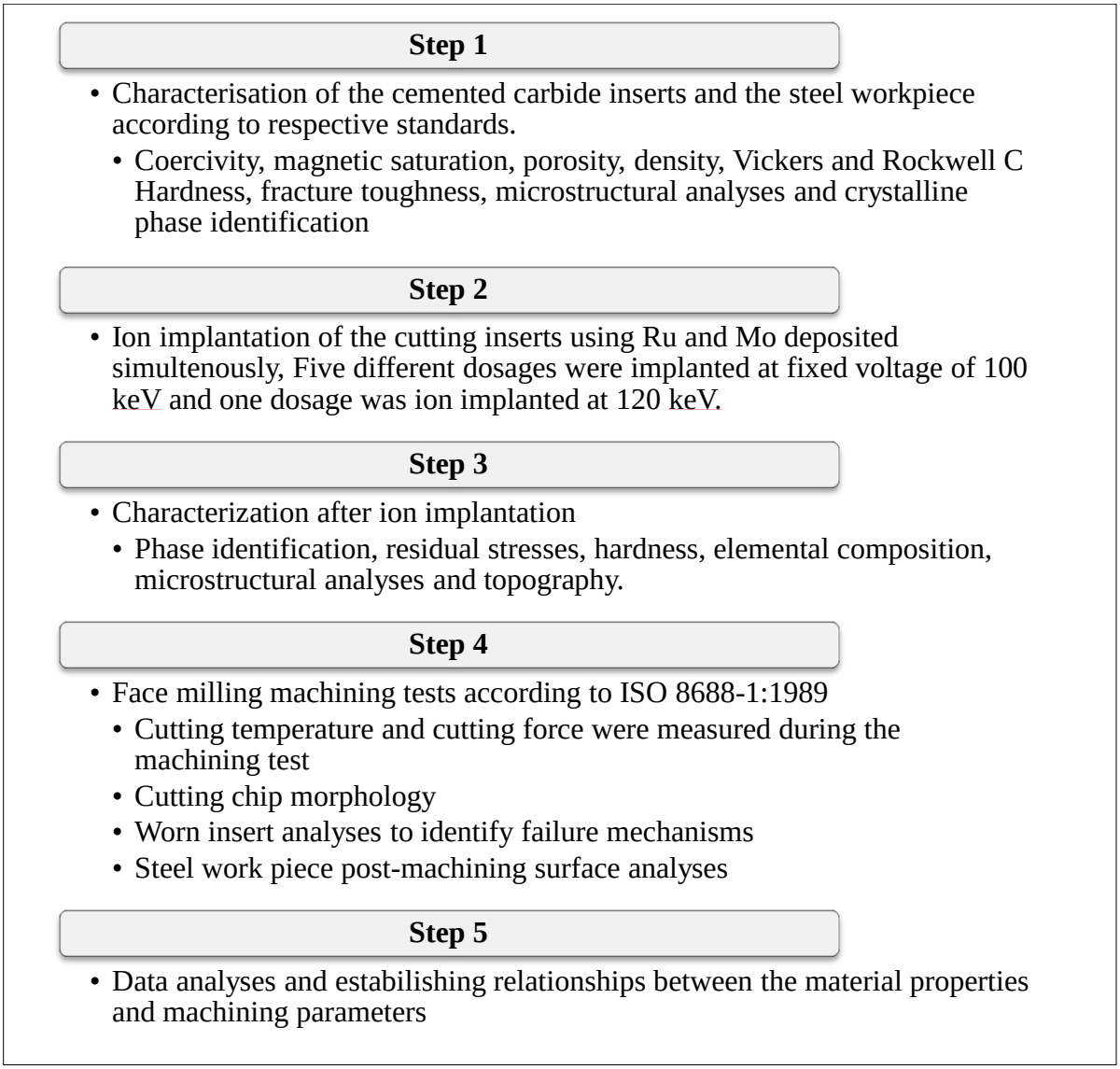


Figure 3.1: Work flow outline of the research study.

3.1 Materials

Coated and uncoated round face milling WC-6wt%Co straight grade inserts (Pilot Tools Pty Ltd, Denver, South Africa) shown in Figure 3.2 were used in this research study. The coating properties are proprietary information.



Figure 3.2: Face milling inserts.

Unhardened H13 tool steel (Bohler steel, South Africa) was used as the work piece in the face milling tests. The chemical composition is shown in Table 3.1. The crystalline phase of the steel workpiece was confirmed using a Bruker D2 Phaser X-ray Diffractometer, with x-ray generator settings of 30 kV and 10 mA, coupled with a cobalt anode. The scan range was 10 mA, coupled with a cobalt anode. The °2Th scan range was 10 to 90° with a 0.02 step size. The peaks were identified using EVA software PDF-4 coupled with the + 2018RDB database.

Table 3.1: Nominal composition of the tool steel.

Fe	C	Cr	Si	Mn	Mo	V
90.56	0.39	5.20	1.10	0.40	1.40	0.95

3.2 Ion Implantation

Ion implantation was done using a 200-20A2F modified ion implanter (iThemba LABS, Gauteng). Ruthenium (Ru) and Molybdenum (Mo) ions were used as sputtering targets and were implanted simultaneously into the inserts according to the five different ion dosages shown in Table 3.2. The individual Ru and Mo ion contributions to each of the total ion dosages are listed. During implantation the acceleration voltage and current were kept constant at 100 keV and 1-3 μA respectively. In order to investigate the influence of acceleration voltage a single ion dosage of 2E+16 ions/cm^2 was implanted using an acceleration voltage of 120 keV

while the current was kept constant at 1-3 μA. Eight coated and 8 uncoated inserts were implanted with each of the six dosages.

Table 3.2: Ion implantation dosages (ions/cm^2).

Total Ion Implantation Dosage	5E+15	8E+15	1E+16	2E+16	1E+17
Mo^+ contribution	4.5 E+15	7.5E+15	8.7E+15	1.9E+16	9.7E+16
Ru^+ contribution	5.1E+14	4.9E+14	1.3E+15	1.1E+15	2.5+15

During implantation the Ru and Mo sputtering targets were ionised using tetrachloride and the generated particles, of a specific atomic mass, were accelerated and directed towards the cutting tool insert. Upon reaching the cutting insert surface the ions either bounced off or penetrated the surface, after which they moved continuously until the acceleration voltage was below 20 eV and then came to rest.

3.3 Face Milling Test

Face milling tests were conducted using a Bridgeport GX 1000 Computer Numerical Control (CNC) machine which is shown in Figure 3.3.



Figure 3.3: Bridgeport GX 1000 showing the machining setup.

The machining tests were conducted according to ISO standard 8688-1:1989 [74], with Table 3.3 showing the process parameters.

Table 3.3: Face milling parameters.

Cutting speed (v_c)	180 m/min
Axial depth of cut (a_p)	2 mm
Radial depth of cut (a_e)	15 mm
Feed per tooth (f_z)	0.2 mm
Feed rate (v_f)	1142 mm/min
Lubricant	Dry machining

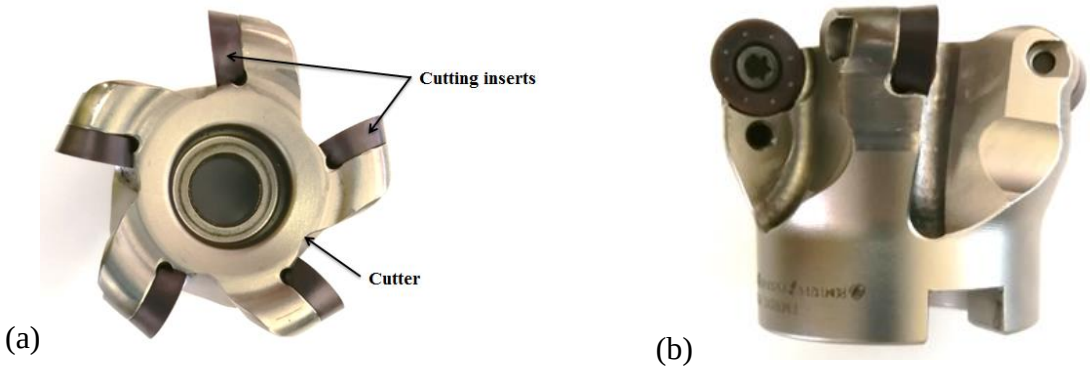


Figure 3.4: Fully loaded cutter (a) top view and (b) side view.

A FM7RD12-052Q22Z5 52 mm diameter cutter fully loaded with 5 equi-spaced cutting inserts was used for the tests (refer to Figure 3.4). The cutter was mounted onto the spindle using a BT40 x 22-spigot arbor as shown in Figure 3.5.

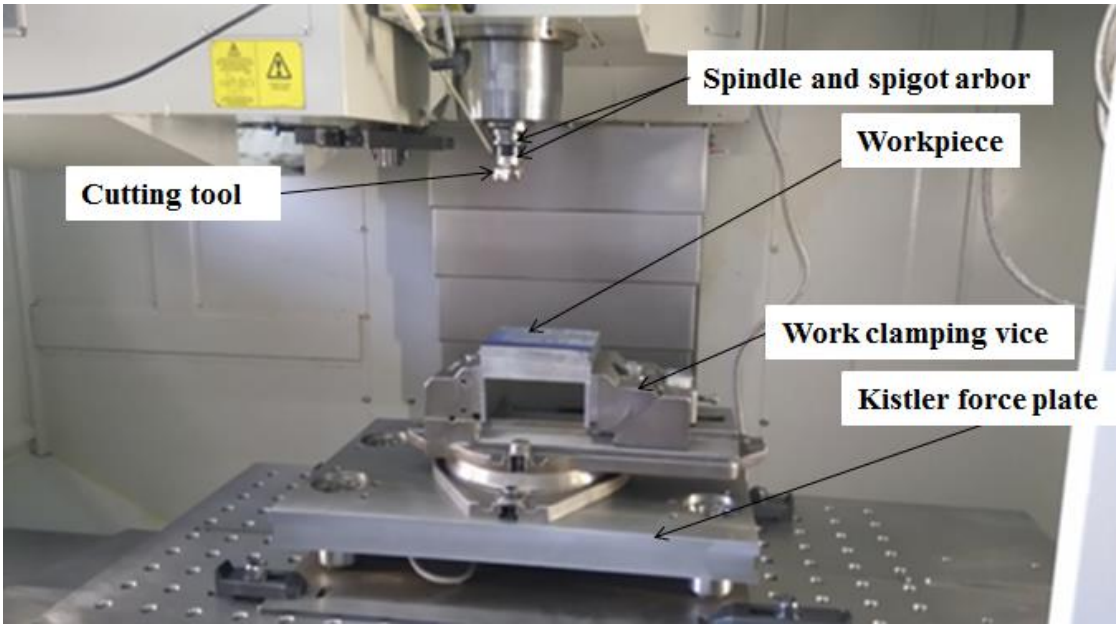


Figure 3.5: Machining setup inside the Bridgeport GX 1000.

The induced cutting forces were measured using a Kistler Multicomponent Force Link 9366CC0 force plate (refer to Figure 3.5) coupled with DynoWare version 2.5.3.8 software, which computed and recorded the forces Fx, Fy and Fz. The cutting temperature variation at the workpiece-tool interface during machining was measured at a distance of 1m away using a FLIR T55901 thermal imaging camera coupled with FLIR Tools Plus Software.

In order to obtain accurate temperature readings the emissivity of the steel workpiece was used as the workpiece was more accessible to the thermal imaging camera. The standard emissivity of the steel was determined by heating the workpiece to 70° in an Ecotherm oven and then measuring its temperature using a Fluke 52II thermometer. The wires of the thermometer were attached onto the steel using scotch weld tape to prevent heat from escaping [75]. The emissivity of the workpiece was found to be 0.22. This value was then used to calibrate the thermal imaging camera.

Tool failure was characterised by occurrence of one of the following failure criterion, as defined by Jawaid et al [33, 74, 76]:

- Flank wear (VB) of 0.7 mm or
- Excessive chipping or
- Severe flaking with a width larger than 0.4 mm

The coated, non-ion implanted, cutting tool inserts were used as a benchmark during machining to set the time to cut the steel until failure occurred. This benchmark test duration was 15 min. Thus the machining performance indicators of all ion implanted cutting tool inserts (both coated and uncoated) was their ability to machine equal volumes for 15 min. The wear scars were studied using a Carl Zeiss Sigma Field Emission Scanning Electron Microscope (FESEM) equipped with an Oxford x-act Energy Dispersive X-ray Spectrometer (EDS) and a Bruker D8 Discover Diffractometer. The workpiece surface roughness was studied using a TR220 Surface Roughness Tester coupled with Time Surf TR 220 V.1.1 software.

3.4 Materials Characterisation Tests

This section describes the materials characterisation tests conducted on the cutting tool inserts at various stages during the research project.

3.4.1 Coercivity

The coercivity of the as-received uncoated inserts was measured using a Dr Förster-Koerzimat coercimeter according to ASTM B887-03 [77]. It provides an indication of the WC grain size and generally; increases with increasing cobalt content and decreasing grain size [78].

3.4.2 Magnetic Saturation

The magnetic saturation of the as-received uncoated inserts was measured using a Setaram 6461 cobalt magnetic saturation machine, equipped with a Sigmameter digital controller and a Scout Pro SPU402 digital balance. The magnetic saturation is used to estimate the binder phase composition [78]; any W which is dissolved in the binder phase will decrease the saturation value of the cobalt phase. A high amount of W in the binder phase is typically an indication of insufficient C in the system which then results in the formation of the eta phase[6].

3.4.3 Porosity

Pores are caused by impurities, inclusions, entrapped gases, poor sintering conditions and inhomogeneous mixing of constituents during sintering [6].They can act as fracture initiation sites and stress raisers [6, 79]. The porosity of the as–received uncoated inserts was quantified using an optical microscope micrographs according to ASTM B276-05 [77].

3.4.4 Density

The density of WC-Co alloys is affected by porosity and the presence of additional constituents such as cubic carbides or chromium and vanadium carbide, which are often added to improve the alloy's properties [64]. The density of the as-received uncoated inserts was measured using hydrostatic weighing according to ASTM B311-08 [77].

3.4.5 Sample Preparation

In order to conduct Vickers hardness, fracture toughness and microstructural characterization, the cutting inserts were cross-sectioned using a Secotom-10 cutting machine and a diamond cut-off wheel. The sectioned samples were mounted in Bakelite using a Leco Mounting Press and then ground and polished to 1 μm surface finish according to the procedure outlined in Table 3.4.

Table 3.4: Sample preparation procedure.

Stage	Disc (Struers)	Lubricant	Time (min)
Grinding	MD Piano 220	H_2O	Till flat
Grinding	MD Piano 1200	H_2O	15
Grinding	MD Piano 2000	H_2O	10
Polishing	MD Dac	3 μm diamond paste	5
Polishing	MD Nap	1 μm diamond paste	3

3.4.6 Vickers Hardness

3.4.6.1 Macro-Hardness

Vickers macro-hardness depends on the grain size, porosity and any crystal structure variation [6]. The hardness of the uncoated polished inserts was measured using a Future-Tech Corp. Vickers hardness machine according to ISO 3878 [80]. An indenting load of 30kg was used for a 10 second dwell time. The average value of the two diagonals from the diamond indentation and the indentation load mass was used to calculate the hardness as indicated in Equation 3.1.

$$HV = \frac{1.8544xF}{\left[\frac{d1 + d2}{2}\right]\text{^}2} \qquad \text{Equation 3.1}$$

Where: HV = Vickers hardness (HV)

F = Indentation load (kg)

d_1&d_2 = diamond indentation diagonal lengths (mm^2)

3.4.6.2 Micro-Hardness

In order to assess the influence of ion implantation on the hardness of the inserts a micro-hardness machine had to be used due to thickness of the modified layer. The micro-hardness of the uncoated and coated inserts was measured using a Future Tech Corp FM 700 Micro Hardness Tester before and after ion implantation. The Vickers indentation tests were conducted using a load of 50g and a dwell time of 15 s [4]. The machine automatically calculates the hardness measurements.

3.4.7 Fracture Toughness

Fracture toughness is a measure of the resistance of a material to crack propagation [6]. The fracture toughness of the uncoated and coated polished inserts was measured according to ISO 28079, which is based on the Palmqvist method [81]. The total lengths of the cracks emanating from the corners of a macro-Vickers hardness indentation were used to calculate the fracture toughness according to Equation 3.2 [78].

$$W_K = A\sqrt{HV}x\sqrt{(F/T)} \qquad \text{Equation 3.2}$$

Where: W_K =Palmqvist fracture toughness ($MN.m^{-3/2}$)

A= constant 0.0028

HV= Vickers Hardness ($HV\text{-}N.mm^{-2}$)

F=Indentation load (30 kgf)

T=Sum of cracks (m)

3.4.8 Quantitative Microstructural Analyses

The microstructure of the uncoated polished inserts was studied using FESEM and EDS. Prior to examination the inserts were etched in order to reveal the microstructure using Murakami's solution; composition indicated in Table 3.5 [77].

Table 3.5: Composition of Murakami's solution [77].

Components	Quantity
KOH (Potassium hydroxide)	10 g
$K_3Fe(CN)_6$ (Potassiumferricyanide)	10 g
Distilled water	100 ml

The FESEM micrographs were subjected to further analyses in order to calculate the WC grain size, WC contiguity and Co binder mean free path. The WC grain size d_{wc} was measured using lineal analyses and Equation 3.3, the grain size is also known as Heyn grain size.

$$d_{WC} = \frac{L}{N} \qquad \text{Equation 3.3}$$

Where: d_{wc} = Heyn grain size (μm)

L = total length across the WC

N = Number of WC grains transversed

The WC contiguity C_α which is the measure of the degree of contact between carbide grains was calculated using Equation 3.4 [6].

$$C_\alpha = \frac{2(N_L)\alpha\alpha}{2(N_L)\alpha\alpha + 2(N_L)\alpha\beta} \qquad \text{Equation 3.4}$$

Where: $(N_L)_{\alpha\alpha}$ = average number of intercepts per unit length of testlines with traces of carbide-carbide grain boundary interface

$(N_L)_{\alpha\beta}$ = average number of intercepts per unit length of testlines with traces of carbide-binder interface

The mean binder free path d_{Co} (µm) is the thickness of the Co layer between the WC grains. It depends on the amount of Co and the grain size. It was calculated using Equation 3.5 [6].

$$d_{Co} = \frac{1}{1 + C_\alpha} \times d_{WC} \times \frac{V_{Co}}{V_{WC}} \qquad \text{Equation 3.5}$$

Where: d_{WC} = mean carbide grain size (µm)

V_{Co} = binder phase volume fraction

V_{WC} = WC phase volume fraction

Microstructure profiles of the cross-sections were constructed in order to assess the effect of the ion implantation, and to determine the thickness of the implanted layer. Elemental mappings were done to provide information on the distribution of the phase constituents.

3.4.9 Crystalline Phase Identification

The crystalline phase of the cutting tool inserts was studied using a Bruker D8 Advance Diffractometer where the grazing incident angle was varied from 1° to 7° with a diffraction pattern range of 15° to 104°. Peak analyses were done using EVA software PDF-4 coupled with the 2018RDB database.

3.4.10 X-ray Photoelectron Spectroscopy (XPS)

The chemical states of Ru and Mo in the coated inserts were determined using a Quantum 2000 X-ray photoelectron spectroscope operated with a monochromatic Al

kα x-ray source (1486.7 eV) operated at 50 W. Ion implantation is known to result in formation of new phases; however, not all phases are crystalline. Therefore XPS was used to determine the ion implanted elements and the compounds that they formed with substrate/target atoms.

3.4.11 Time-of-Flight Secondary Ion Mass Spectroscopy (TOFSIMS)

The distribution and concentration of the implanted atoms in the coated inserts was determined using Time-of-Flight Secondary Ion mass spectroscopy (TOF.SIMS 5, ionTOF) with a beam energy and current of 25 keV and 1 pA respectively. The concentration of the ion implanted ions was below the quantities that can be detected using elemental mapping. However, TOFSIMS can detect very low concentrations such as dopants (implanted ions) and impurities.

3.4.12 Atomic Force Microscope (AFM)

The effect of ion implantation on the surface roughness was studied using a Veeco Di 3100 Atomic Force Microscope with a silicon cantilever operated in contact mode and coupled with Nanoscope analysis software 2011. The AFM cantilever tip moved on the surface in a raster pattern, recording the height of the tip at each position, which was used to generate surface area map [20]. The dimensions of each scan area were 30 µm x 30 µm.

3.4.13 Residual Stress Measurements

Residual stress measurements were done using a Bruker D8 Discover with Azimuth angles (ϕ) ranging from 0° to 270° and tilt angles (Ψ) ranging from 0 to 70° in steps of 10° giving 8 sample tilt positions for a total time of 240 s. Stress analysis of the in-plane components σ_{11} and σ_{12} was done by employing the $\sin^2 \Psi$ technique in conjunction with LEPTOS v6 which is a data radiation and stress calculation program which uses the measured Bragg peak positions at the various Ψ-tilt angles as input

and incorporating the corresponding diffraction elastic moduli. The stress measurements were conducted on the flank face as indicated in Figure 3.6.

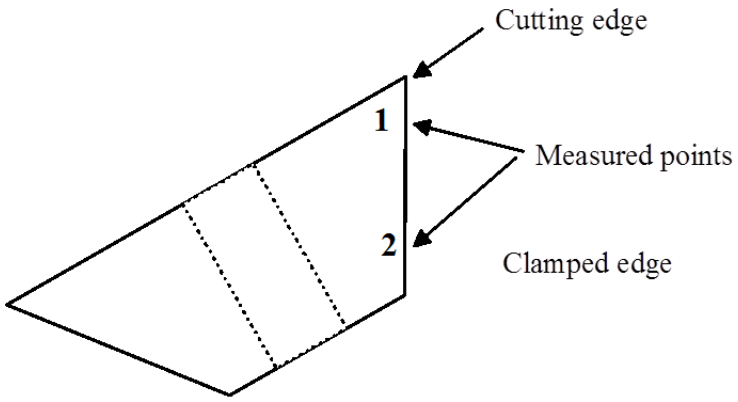


Figure 3.6: Positions on the cutting tool inserts where stress measurements were conducted.

3.4.14 Rutherford Backscattering Spectroscopy (RBS)

Rutherford Backscattering Spectroscopy was used to detect the presence of ion implanted elements in the sample. It is often used for elemental depth analysis of single or multilayer systems. A 6 MeV tandem accelerator was used to accelerate the energetic charged helium (He) particles to 3.60 MeV. The energetic ion beam was directed to the RBS target chamber where it struck the target surface, particles scattered through an angle greater than 90º were detected as shown in Figure 3.7. The charge was set at 500 nC. In addition to the particle detector for RBS; an x-ray detector for Particle Induced X-ray Emission (PIXE) was also used in order to determine the elemental composition of the sample. This was used as a complement for RBS due the wide difference between atomic mass of tungsten (W) and the ion implanted ions (Ru and Mo), which can make it difficult for the light elements to be detected especially at low concentrations.

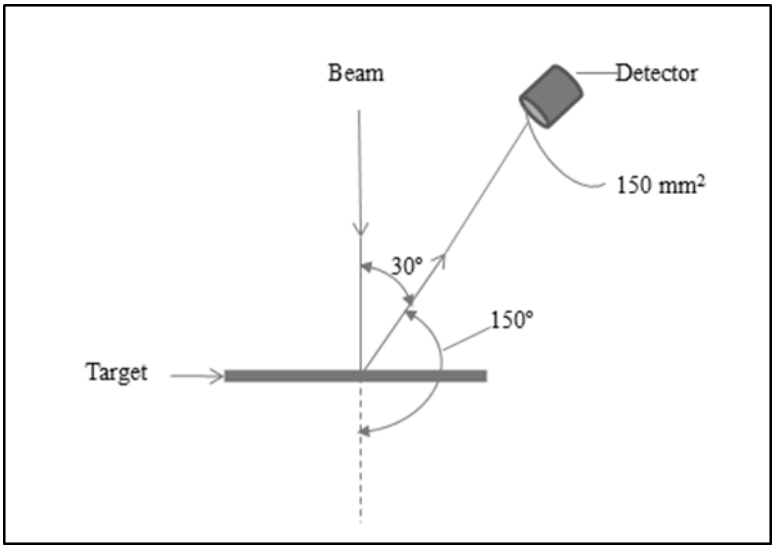


Figure 3.7: Schematic representation of the RBS operation.

Chapter 4 Results

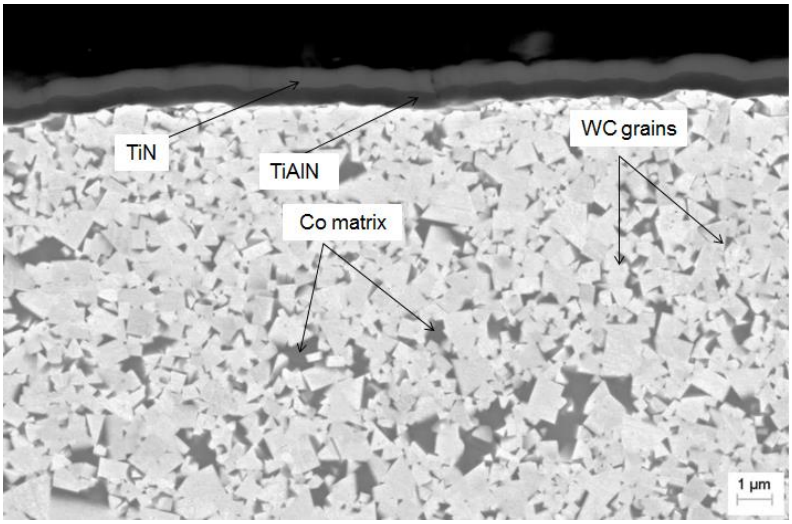
This chapter presents the results of the experimental work conducted according to Chapter 3. It must be noted that in this chapter all the results associated with the different ion implantation dosages were implanted using an acceleration voltage value of 100 keV. The results of the single ion implanted dosage using the acceleration voltage of 120 keV are accredited with the voltage value. This chapter is sub-divided into 4 sections:

- Section 4.1 Characterisation of the cutting tool inserts prior to ion implantation
- Section 4.2 Characterisation of the steel workpiece
- Section 4.3 Characterisation of the Ru and Mo ion implanted cutting tool insert.
- Section 4.4 Face Milling Tests Results

4.1 Characterisation of the cutting tool inserts prior to ion implantation

Figure 4.1 (a) is an FESEM image of the cross-section of the coated tool insert. The TiN and TiAlN coatings are clearly visible and have an average coating thickness of 556 and 515 nm respectively. The TiAlN coating was deposited first due to its thermal stability, good adhesion and impact resistance, the TiN was added second mainly for its low coefficient of friction and low wear rate compared to TiAlN [82–84]. The evenly distributed dark grey trapezoidal shaped WC grains, showing different crystal orientations, are embedded in the Co matrix. Even distribution is important for the mechanical properties as it ensures strength and integrity of the substrate. No deleterious phases such as eta phase were found in the alloys as confirmed by the XRD pattern shown in Figure 4.1 (b), where only WC peaks were detected.

(a)



(b)

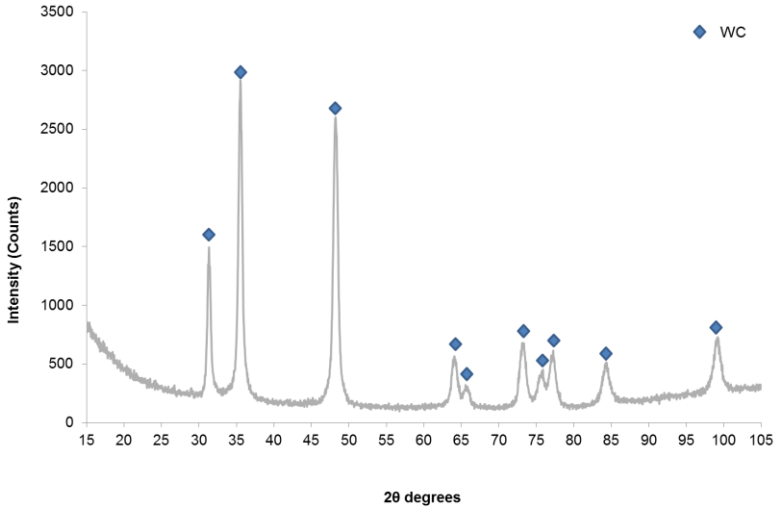


Figure 4.1: (a) FESEM micrograph of the cutting tool insert cross-section with the corresponding XRD pattern shown in (b).

The strength of the coated tool inserts depends on the substrate [85]. The results in Table 4.1 are the material properties of the uncoated cutting inserts, which is also the substrate of the coated inserts and the values are in agreement with those found in literature for a WC-6wt%Co alloy [6]. The Vickers hardness and the fracture toughness are in agreement with literature for an alloy with 6 wt% Co and 0.52 µm WC grain size. Magnetic saturation and coercivity are quality control parameters that provide an indication of the presence of deleterious phases (eta phase) and the WC grain size respectively. The magnetic saturation and coercivity results show no presence of deleterious phase and the smaller grain size respectively, which is in agreement with the rest of the results. Type A02 porosity indicates that pore size was less than 10 µm and the porosity volume % was 0.02%. This is good as pores can act

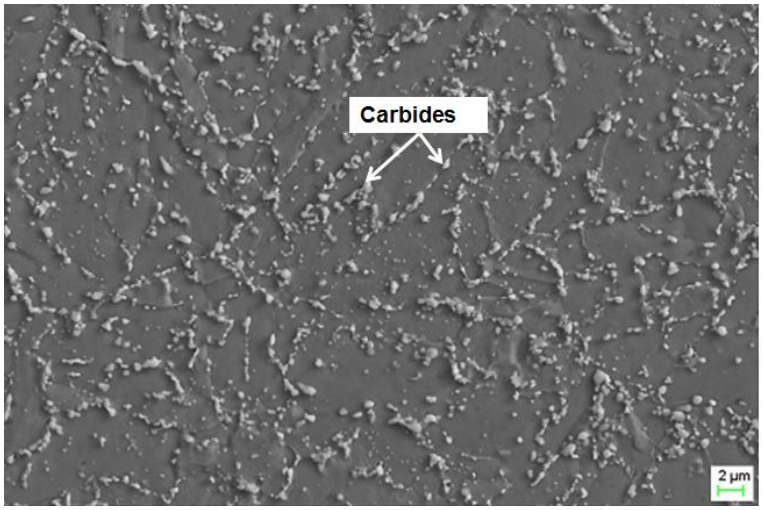
as stress raisers, fracture and cracks initiation and allow easy propagation of cracks. The density was inline with the porosity results and in agreement with literature.

Table 4.1: Material properties of the uncoated inserts.

Property	Units	Value
Vickers Hardness	MPa	1620±3.2
Fracture Toughness	$MN.m^{-3/2}$	10.58±0.07
Density	gcm^{-3}	14.47±0.01
Porosity	Type	TypeA02, TypeB00, TypeC00
Coercivity	kAm^{-1}	20.69± 0.16
Magnetic saturation	μTm^{3}	18.78± 0.39
Grain size	µm	0.52±0.01

4.2 Workpiece

Figure 4.2 (a) is an FESEM micrograph showing the microstructure of the H13 tool steel, which was used as the workpiece during the face milling tests. The steel was selected since majority of metal cutting industry in South Africa uses the round face milling cutting tool inserts to machine it. The micrograph shows that ferrite grains have undissolved carbides along their grain boundaries. The microstructure was predominantly cubic Fe as identified using XRD analyses, shown in Figure 4.2 (b). A Rockwell C hardness of 20 ±0.19 was measured for the steel.

(a) 

(b)

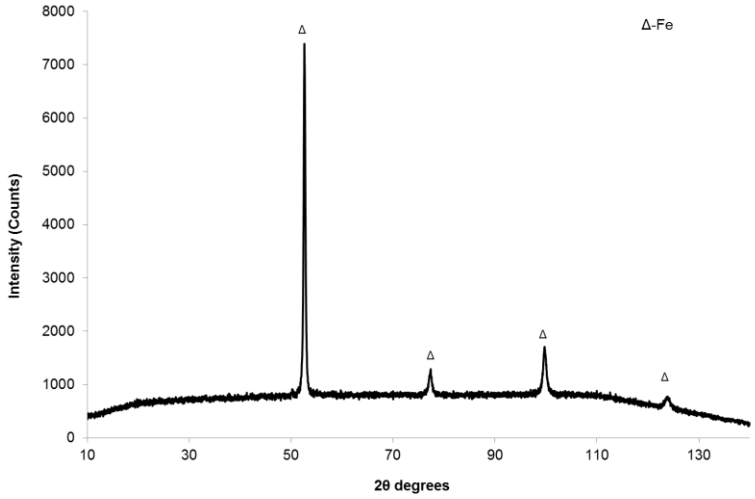


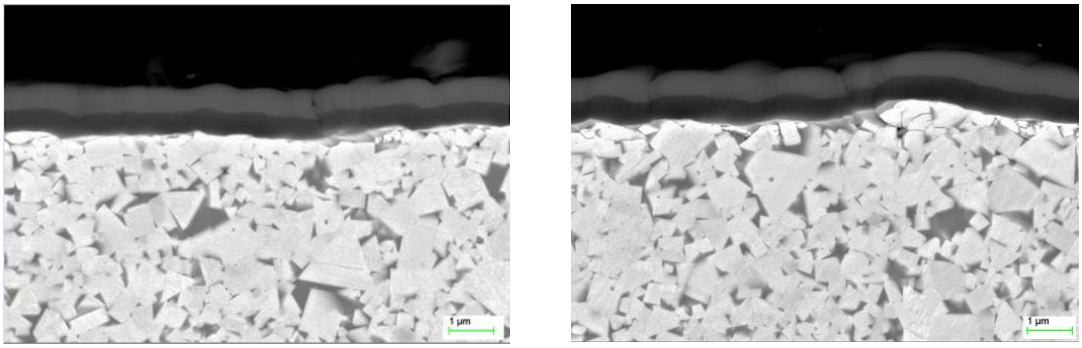
Figure 4.2: FESEM micrograph of the H13 steel microstructure with the corresponding XRD pattern shown in (b).

4.3 Characterisation of the Ru and Mo ion implanted cutting tool inserts

This section presents the results of the materials characterisation tests conducted on the cutting tools inserts after Ru and Mo ion implantation. The results are compared to those of the non-implanted cutting tools inserts.

4.3.1 FESEM and EDS analyses

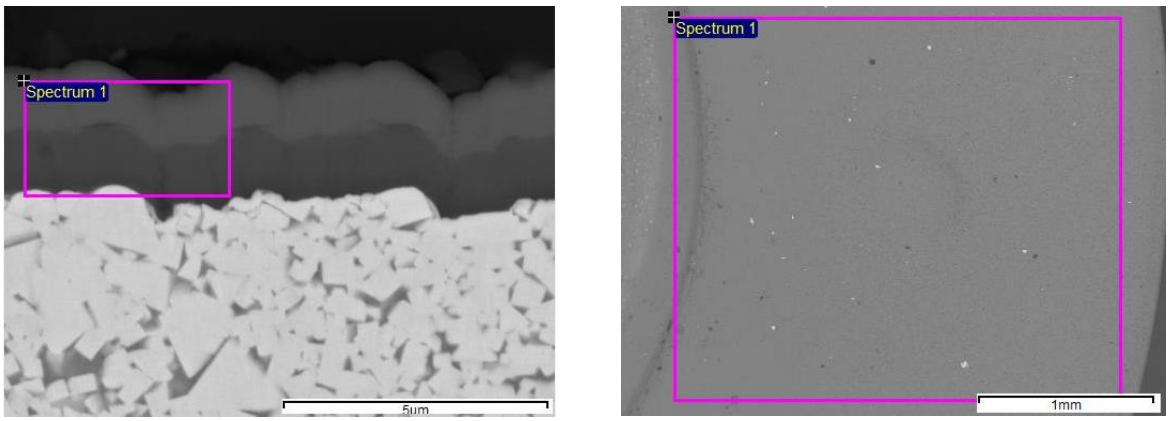
Figure 4.3(a) is an FESEM micrograph of the non-implanted cutting tool insert and (b) is a micrograph of the ion implanted insert at ion implantation dosages of 1E+17 ions/cm^2, there is no visible physical change on the microstructure. This was observed with all the other dosages in both sets of inserts (coated and uncoated) as shown in Appendix A.



(a) (b)

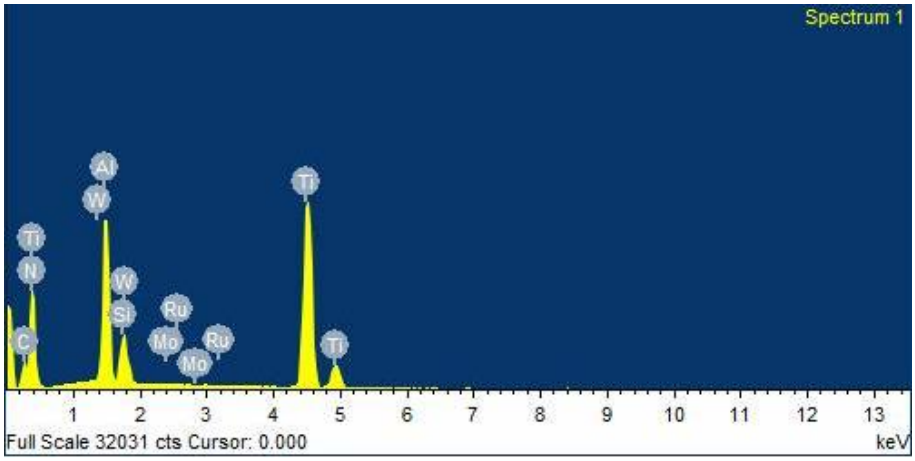
Figure 4.3: FESEM micrograph of (a) non-implanted inserts and (b) insert with ion implantation dosage of 1E+17 ions/cm^2.

Energy dispersive spectroscopy (EDS) was used to determine the elemental composition on the cross-section and the coated surface of the insert with ion implantation dosage of 1E+17 ions/cm^2 as shown in Figure 4.4 (a) and (c). The corresponding EDS spectra are shown by Figure 4.4 (b) cross-section and (d) coating; both EDS spectra images show the presence of the Ru and Mo. As expected the cross section show less Ru and Mo compared to the coating as shown in Figure 4.5, as Ru and Mo in cross-section were 67% and 95% less than that of the coating respectively, due to the short distance travelled by ions and distance of penetration during EDS scan.



(a) (c)

(b)



(d)

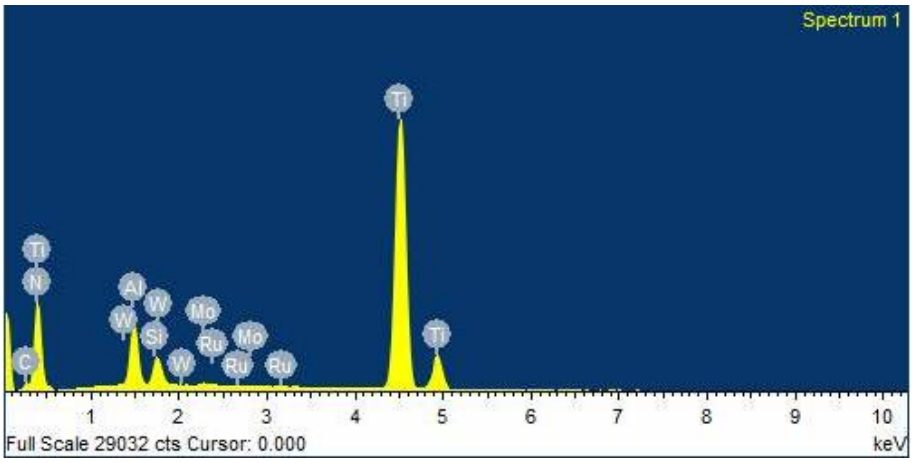


Figure 4.4: (a) FESEM micrograph of the cross-section, (b) corresponding EDS spectrum (c) FESEM micrograph of coating and (d) corresponding EDS spectrum of the insert with ion implantation dosage of 1E+17 ions/cm^2.

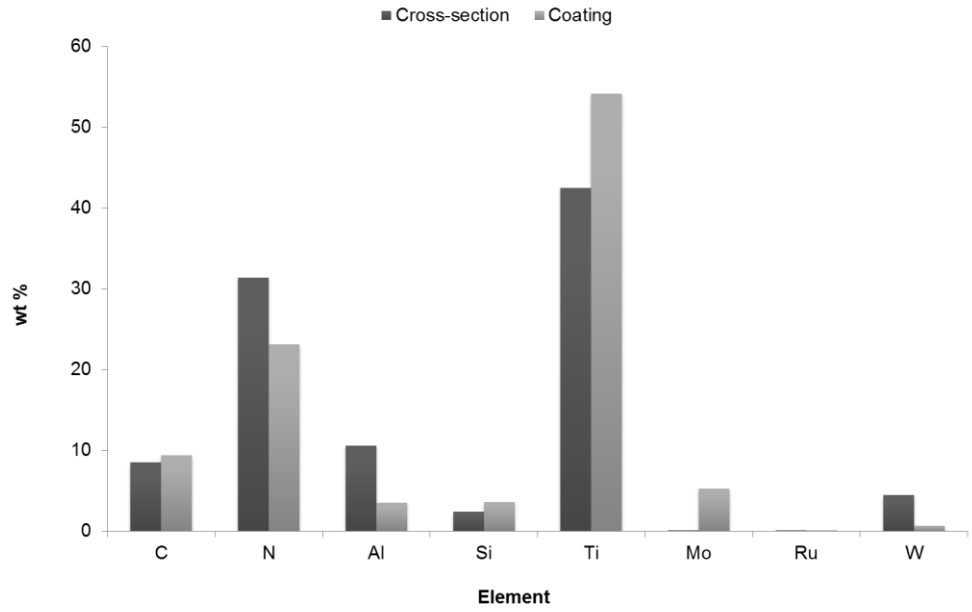


Figure 4.5: Elemental composition of the cross-section compared to that of the coating of the insert with ion implantation dosage of 1E+17 ions/cm^2.

Figure 4.6 is the composition of Ru and Mo in the coating of the inserts at different ion implantation dosages. Initially, the composition of both Ru and Mo increased with increasing ion implantation dosage until the ion implantation dosage of 1E+16 ions/cm^2 where the Mo composition was 31% lower compared to the Mo in the ion implantation dosage of 8E+15 ions/cm^2. However, the composition of Ru was 64% higher than that of the Ru in the ion implantation dosage of 8E+16 ions/cm^2. The compositions of Ru and Mo of the insert implanted at 2E+16 ions/cm^2 and acceleration voltage of 120 keV are 5 and 57% lower than that of insert with ion implantation dosage of 2E+16 ions/cm^2 and acceleration voltage of 100 keV. The composition of Ru and Mo for the insert with ion implantation dosage of 1E+17 ions/cm^2 were significantly higher compared to the other dosages.

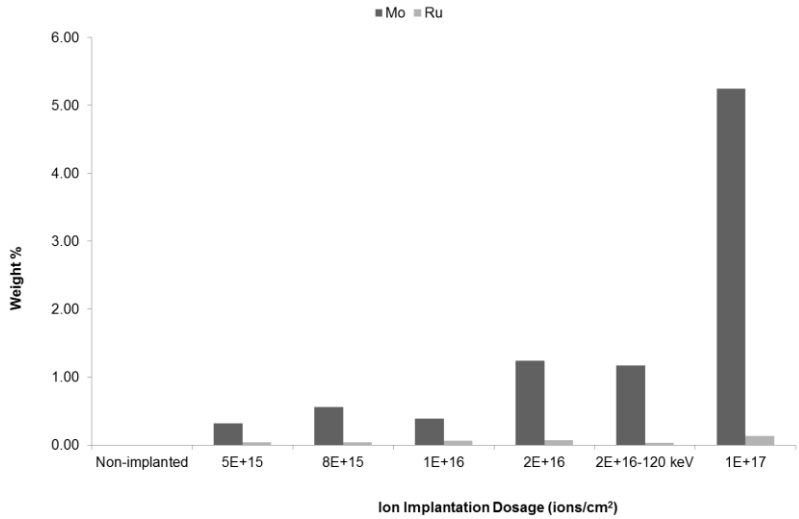
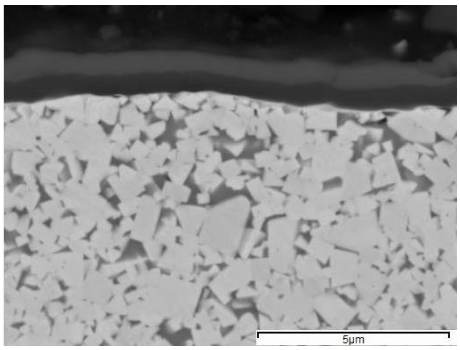
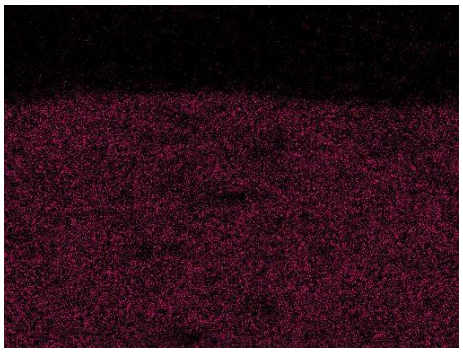


Figure 4.6: Ru and Mo composition at different ion implantation dosages.

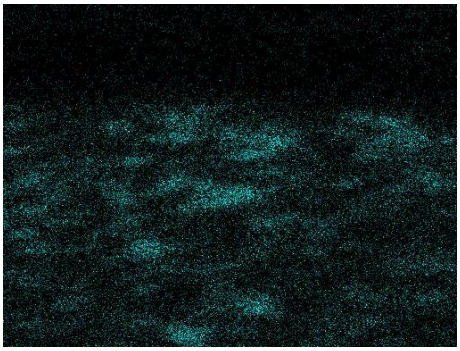
Elemental mapping was done on the cross-section of the insert with ion implantation of 1E+17 ions/cm^2, results are shown in Figure 4.7. Due to the low quantities of the ion implanted elements the maps showed no traces of Ru and Mo as shown in Figure 4.7 (g) and (h) respectively.



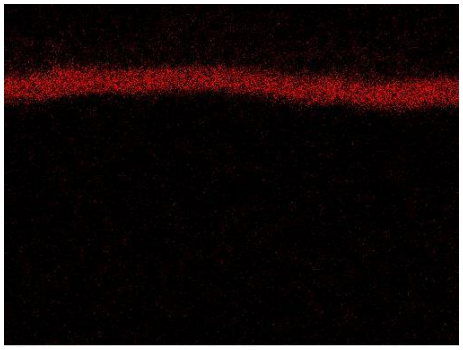
*(a)



(b)



(c)



(d)

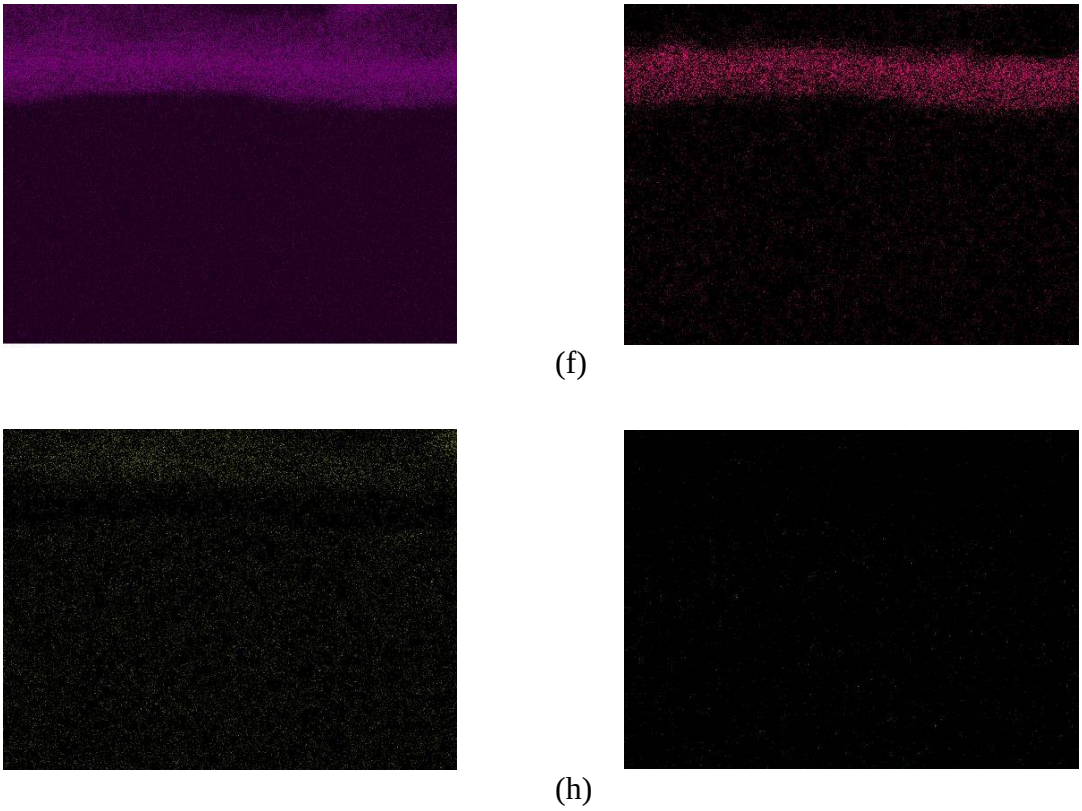


Figure 4.7: Elemental mapping of the cutting tool insert with ion implantation dosage of 1E+17 ions/cm^2 (a) FESEM micrograph of the scanned, and the elemental mapping of (b) tungsten (W), (c) cobalt (Co), (d) aluminium (Al), (e) titanium (Ti), (f) nitrogen (N), (g) molybdenum (Mo) and (h) ruthenium (Ru).

4.3.2 Rutherford Backscattering Spectroscopy (RBS)

Rutherford backscattering spectroscopy was used in an attempt to quantify the amount of Ru and Mo implanted into the inserts, and to compliment the EDS results, which are presented in section 4.3.1. Figure 4.8 and Figure 4.9 show the RBS results spectra for the coated and uncoated inserts implanted with 2E+16 Ru and Mo ions at an acceleration voltage of 100 keV, while Figure 4.10 shows the RBS spectra for the coated inserts implanted with the same ion dosage at an acceleration voltage 120 keV. The RBS spectra for the remaining inserts are shown in Appendix B. In the figures the y-axis 'Yield counts' represents the quantities of the different elements, while the x-axis represents the binding energies that correspond to the different elements, as indicated by the vertical lines. As expected the Ru and Mo yield increased from 3 to 22 as the ion implantation dosage increased for the coated inserts. An increased acceleration voltage did not appear to increase the amount of ions implanted where

* The scale bar in Figure 4.7 (a) applies to all the images in the figure

yield of 8 counts was measured for the coated inserts and a yield 5 counts was measured for the 120 keV inserts. In the RBS spectra of the uncoated inserts binding energy of the Ru and Mo is indicated by the dotted lines, as shown in Figure 4.9, which corresponds to the position where these elements should be detected. Due to the high atomic mass and high yield of W in the inserts, the yields for the Ru and Mo could not be quantified for the uncoated inserts.

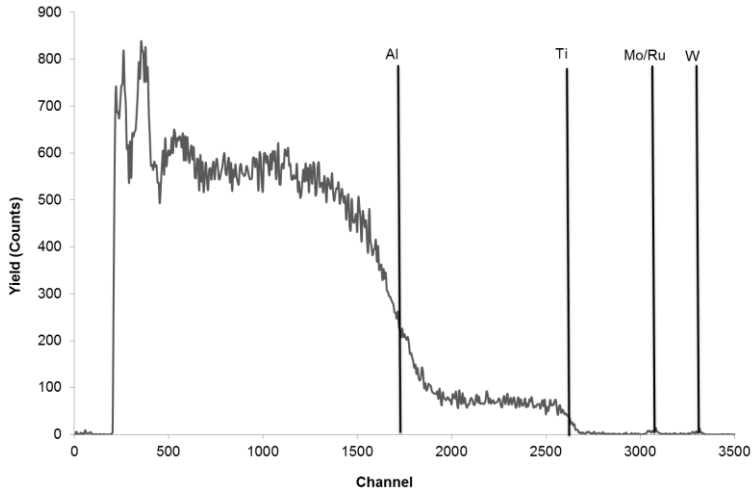


Figure 4.8 RBS of the coated cutting tool inserts implanted at an ion implantation dosage of 2E+16 ions/cm^2.

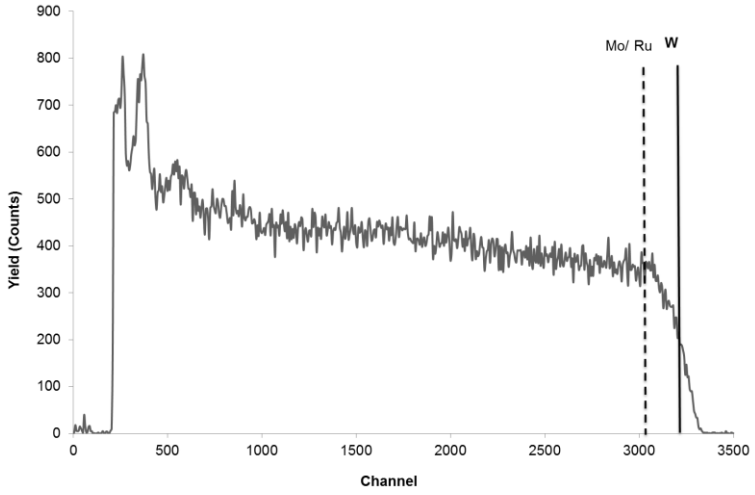


Figure 4.9: RBS results of the uncoated cutting tool inserts implanted at 2E+16 ions/cm^2.

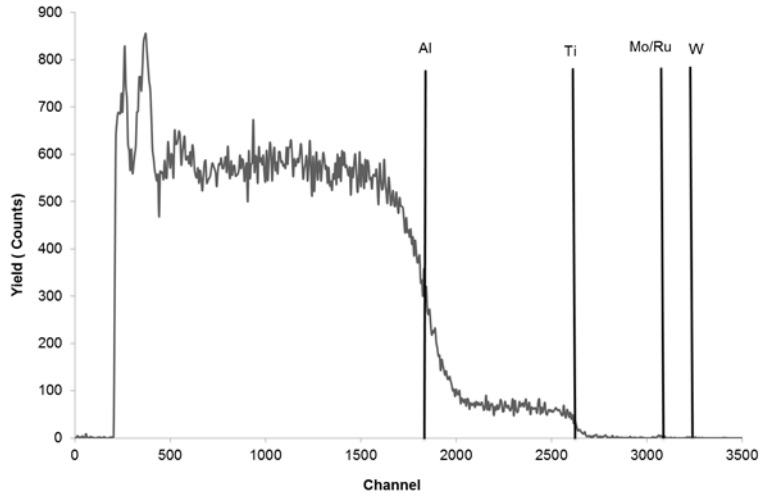


Figure 4.10 RBS of the coated cutting tool inserts implanted at ion implantation dosage of 2E+16 ions/cm^2 at 120 keV.

4.3.3 Micro-hardness of the cutting tool inserts

Figure 4.11 shows the Vickers micro-hardness of the coated and uncoated cutting tool inserts after ion implantation. An increase in hardness of 9 to 32% was achieved in both sets of inserts for the ion dosage range implanted. The relationship between hardness increase and increasing ion implantation dosage was not linear for both sets of inserts. When comparing both sets of inserts, the minimum and maximum hardness increase was achieved at 5E+15 and 8E+16 ions/cm^2 respectively for coated inserts, while minimum and maximum hardness increase were achieved at 2E+16 and 8E+16 ions/cm^2 respectively for uncoated inserts. However, the maximum hardness increase for coated inserts was at an implantation dosage of 1E+17 ions/cm^2, only coated inserts were implanted at this dosage. The hardness of implanted inserts was higher than that of non-implanted. Uncoated implanted inserts had the highest hardness increases with respect to the non-implanted uncoated insert.

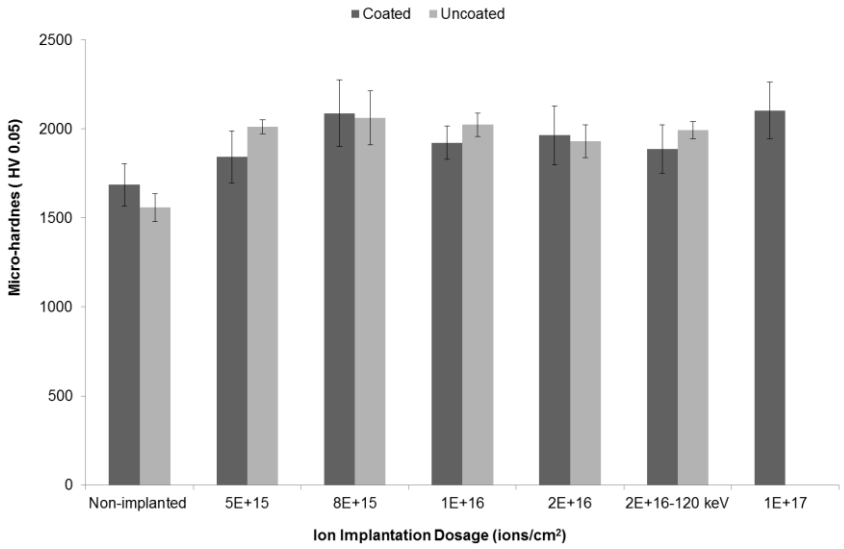
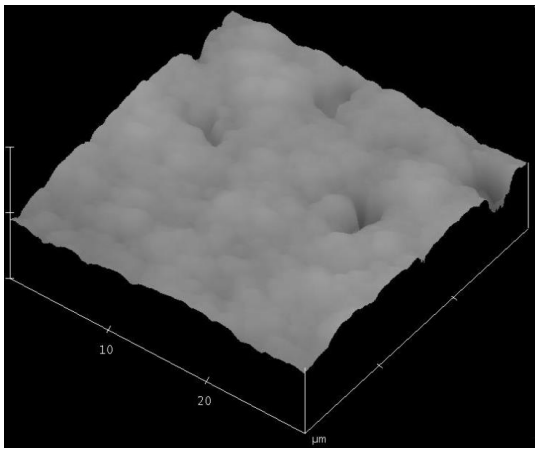


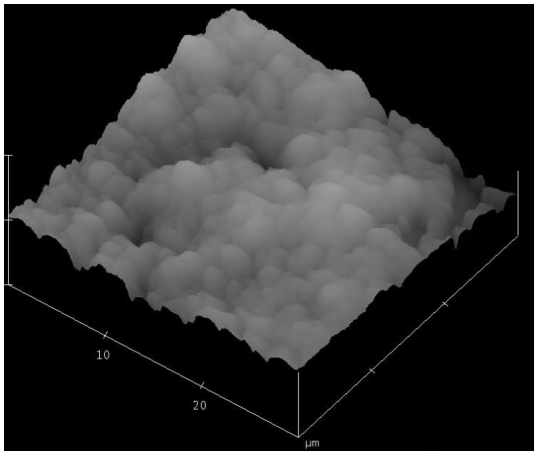
Figure 4.11: Vickers Micro-hardness of the Ru + Mo ion implanted cutting inserts at different ion implantation dosages.

4.3.4 Surface Roughness

The surface topography of both non-implanted and ion implanted inserts is shown in Figure 4.12 and Figure 4.13 for the coated and uncoated inserts respectively. In general, ion implantation led to an increase in the surface roughness which produced non-uniform surfaces. The average surface roughness for the inserts is illustrated in Figure 4.14.



(a)



(b)

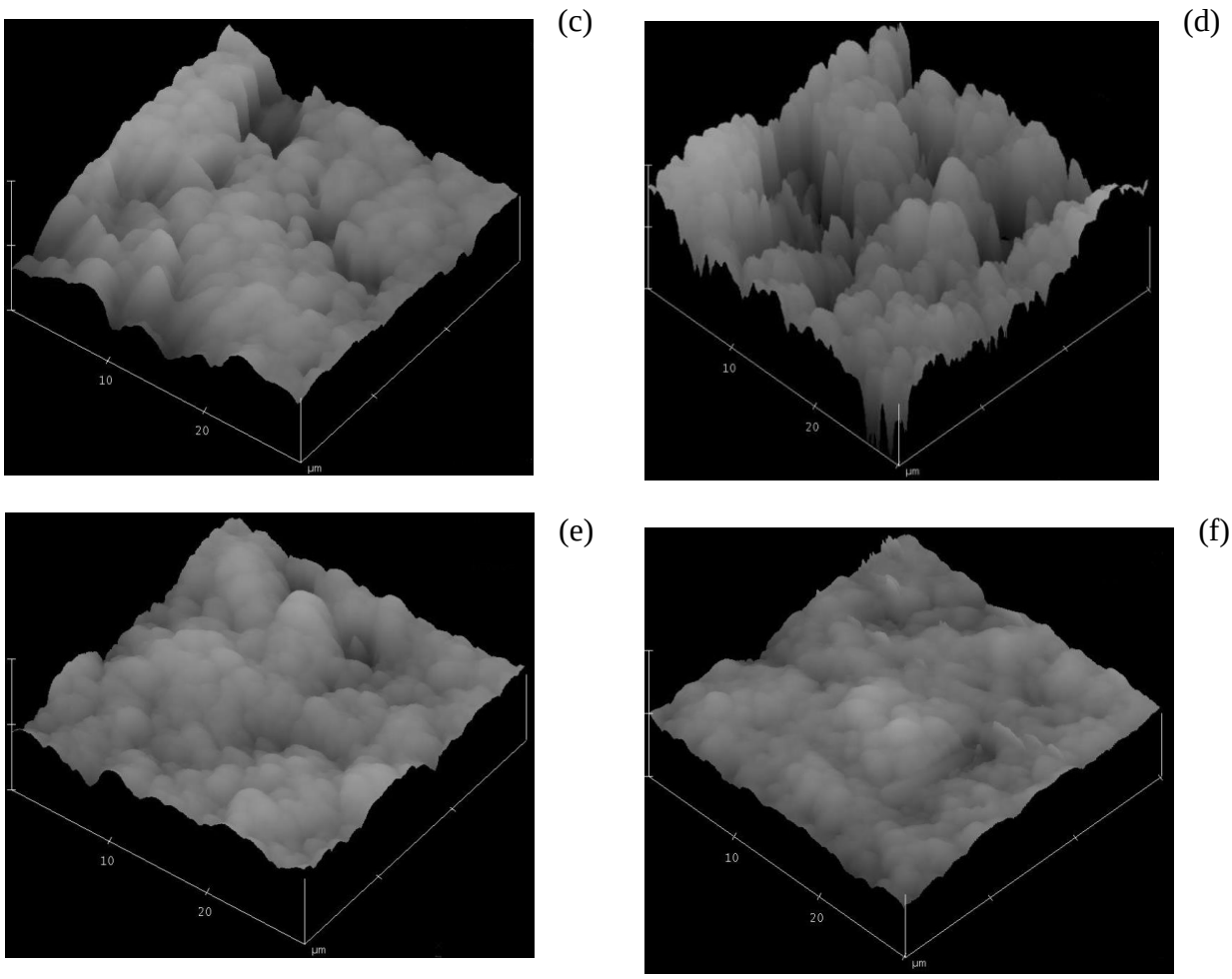


Figure 4.12: AFM images of the coated cutting tool inserts showing surface at topography at different ion implantation dosage s (a) non-implanted, (b) 5E15, (c) 8E15, (d) 1E16, (e) 2E16 and (f) 1E17 ions/cm^2.

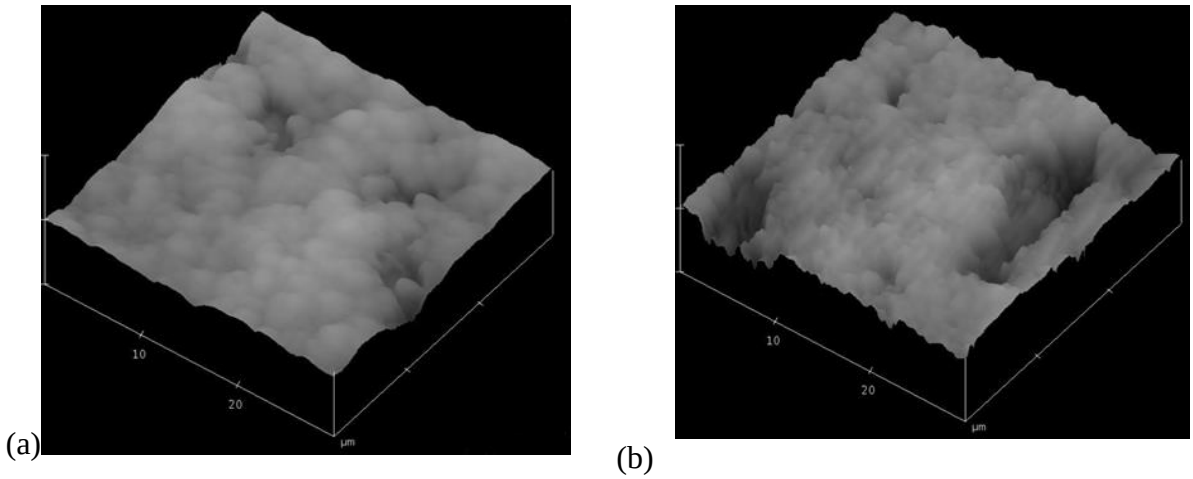


Figure 4.13: AFM images of the cutting tool inserts showing the surface morphology. (a) Non-implanted (b) ion implantation of 1E+16.

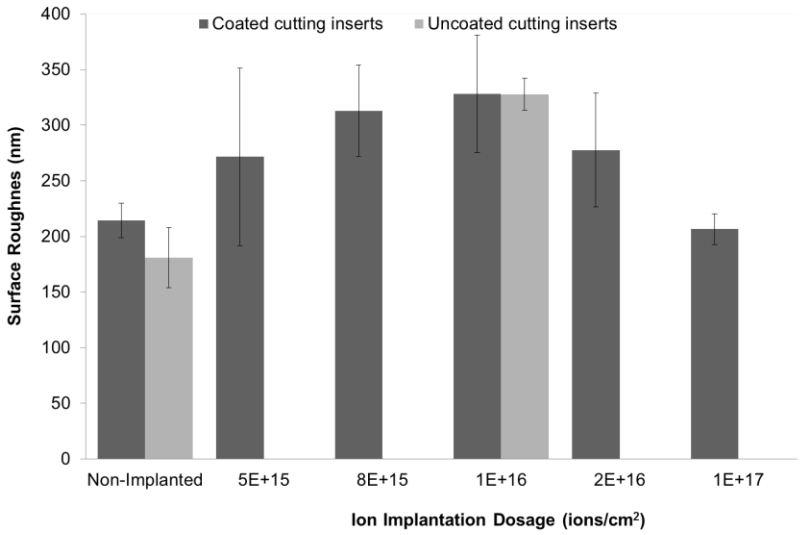


Figure 4.14: Average surface roughness at different Ru + Mo ion implantation.

4.3.5 Residual Stresses

Due to the surface topography changes that were observed with ion implantation, it was decided to measure the residual stresses of the coated inserts. Figure 4.15 provides a comparison of the residual stresses in the inserts showing that all stresses were compressive, ranging from 587 to 1097 MPa. An increase in residual stresses of 5 to 40% and a decrease of 8 to 25% were observed. There is no direct relationship between increasing ion implantation dosage and stress. The residual stresses for ion implantation of 5E+15, 8E+15 and 1E+16 were the same, minimum residual stresses of 587 MPa were observed at ion implantation dosage of 2E+16–120 keV and maximum residual stresses of 1097 MPa were observed at an ion implantation dosage of 2E+16-100 keV. Due to the difference in acceleration voltage, a 510 MPa difference in the residual stresses between ion implantation dosage of 2E+16 and 2E+16-120 keV was observed.

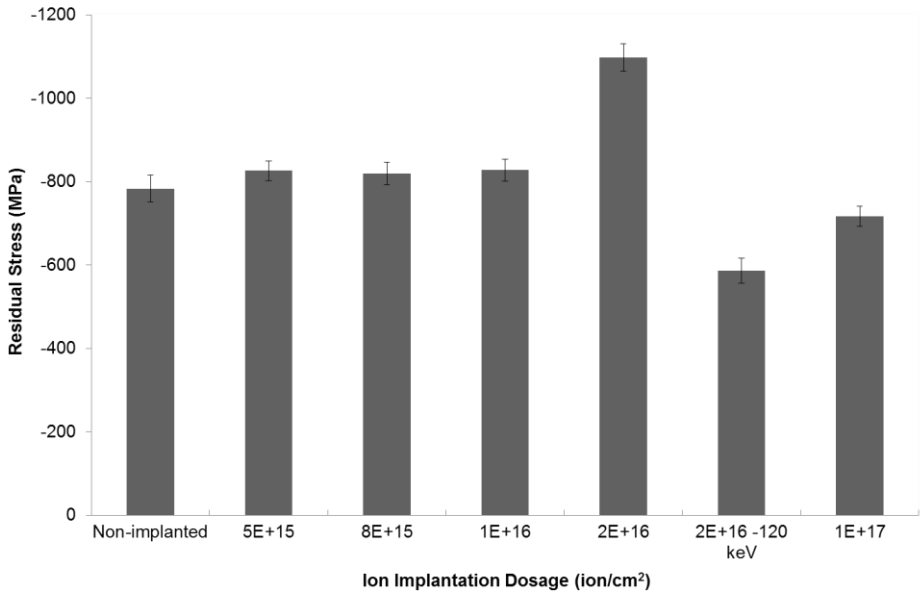


Figure 4.15: Residual stresses of the Ru and Mo ion implanted coated cutting tool inserts.

4.3.6 Grazing Incident X-ray Diffraction (GIXRD)

The grazing incident x-ray diffraction patterns of four inserts are shown in Figure 4.16 to Figure 4.19 with respect to 5 different grazing incident angles. The XRD patterns for remaining inserts are provided in Appendix C. Figure 4.16 and Figure 4.17 are patterns of the coated non-implanted and coated ion implanted inserts respectively, while Figure 4.18 and Figure 4.19 are the patterns of the uncoated inserts. Figure 4.17 and Figure 4.19 represent the 2E+16 ions/cm^2 ion implantation dosages for the coated and uncoated cutting tool inserts respectively. In the diffraction patterns of all the coated inserts the WC, TiN and TiAlN phases were identified, while only the WC phase was detected in all the uncoated inserts. None of the diffraction patterns showed the presence of Ru and Mo, which was implanted into the inserts. Even the employment of 5 different grazing angles during the XRD analyses did not lead to the detection of these elements. This implies that Ru and Mo did not form any crystalline phase during ion implantation. It was observed that the crystallinity of the inserts increased with increasing grazing incident angle. At low grazing angle it mostly showed beam deflection and the beam penetrated a few nanometres of the target, which was not crystalline.

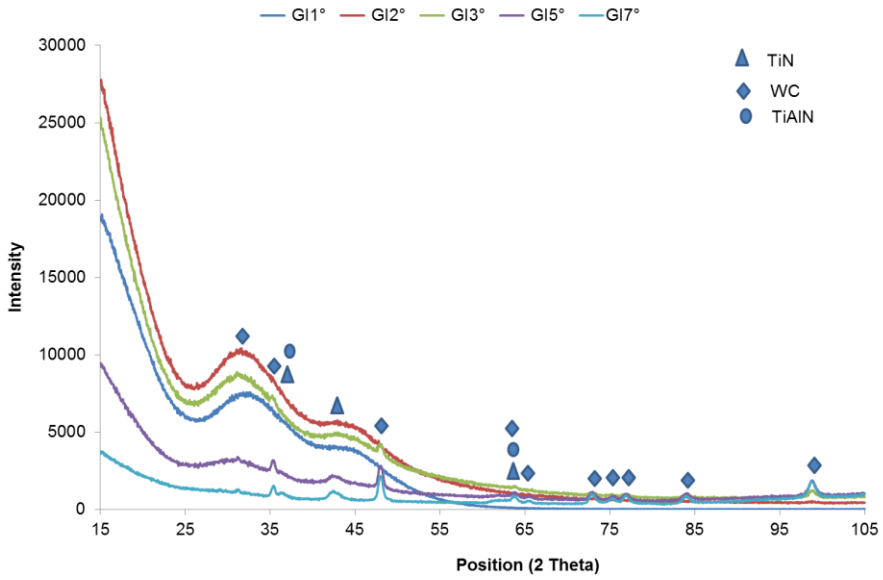


Figure 4.16: X-ray diffraction pattern analysis of coated non-implanted cutting inserts.

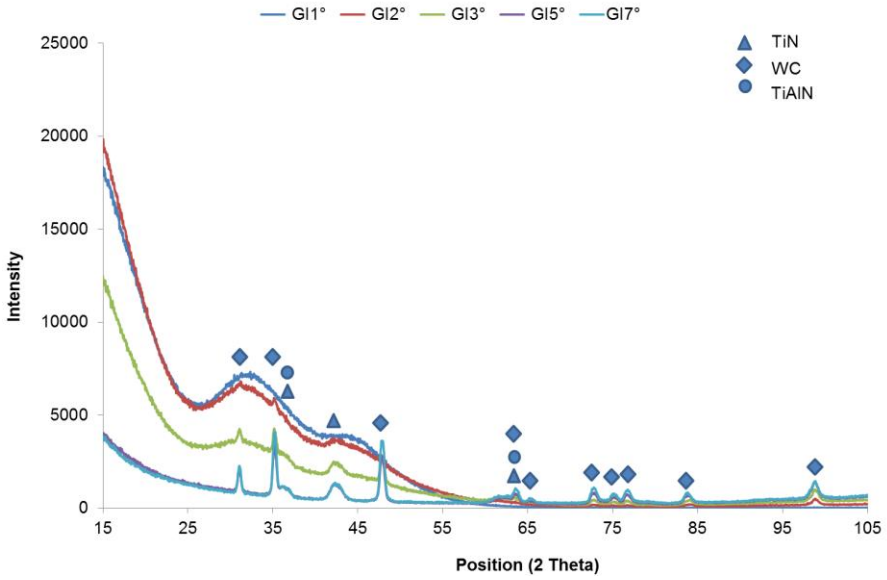


Figure 4.17: X-ray diffraction pattern analysis of the coated cutting tool inserts implanted at 2E+16 ions/cm^2 dosage.

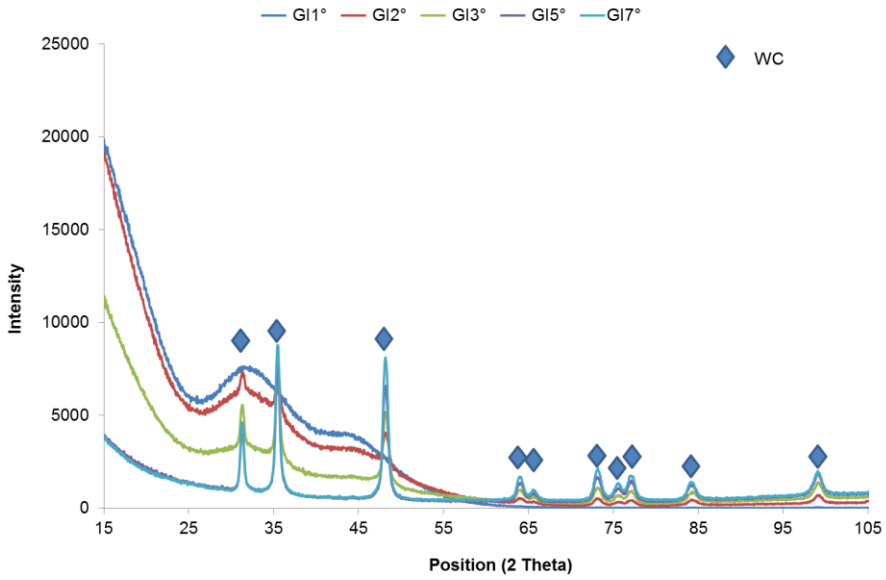


Figure 4.18: X-ray diffraction pattern analysis of the non-implanted uncoated cutting tool insert.

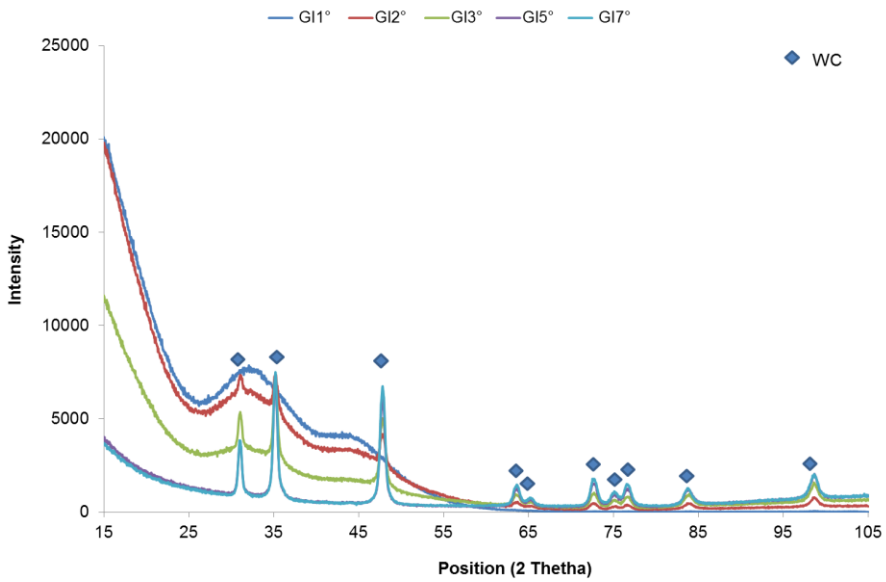


Figure 4.19:X-ray diffraction pattern analysis of the uncoated cutting tool inserts implanted at 2E+16 ions/cm^2.

4.3.7 X-ray Photoelectron Spectroscopy (XPS)

In an attempt to identify possible phases created by the implantation of Ru and Mo three coated inserts were subjected to XPS analyses. Figure 4.20 is the XPS spectrum for the non-implanted coated insert, which served as the benchmark for comparison. Figure 4.21 is the XPS spectrum of the highest ion dosage of 1E+17 ions/cm^2 at 100 keV, while Figure 4.22 shows the XPS spectrum for the ion dosage of 2E+16 ions/cm^2 implanted at an acceleration voltage of 120 keV. The binding energy on the

x-axis was used to determine the corresponding chemical states. The binding energies in Figure 4.20 show elemental spectra lines of O, Ti, N and Al, which are elements present in the coatings. Figure 4.21 shows binding energies corresponding with elemental line spectra of Ti, O, N, Mo, Co and Al. Figure 4.22 shows the binding energies corresponding with O, Ti, Mo, N and Al. Both ion implanted XPS spectra in Figure 4.21and Figure 4.22 did not show any binding energy corresponding to the elemental line spectra of Ru.

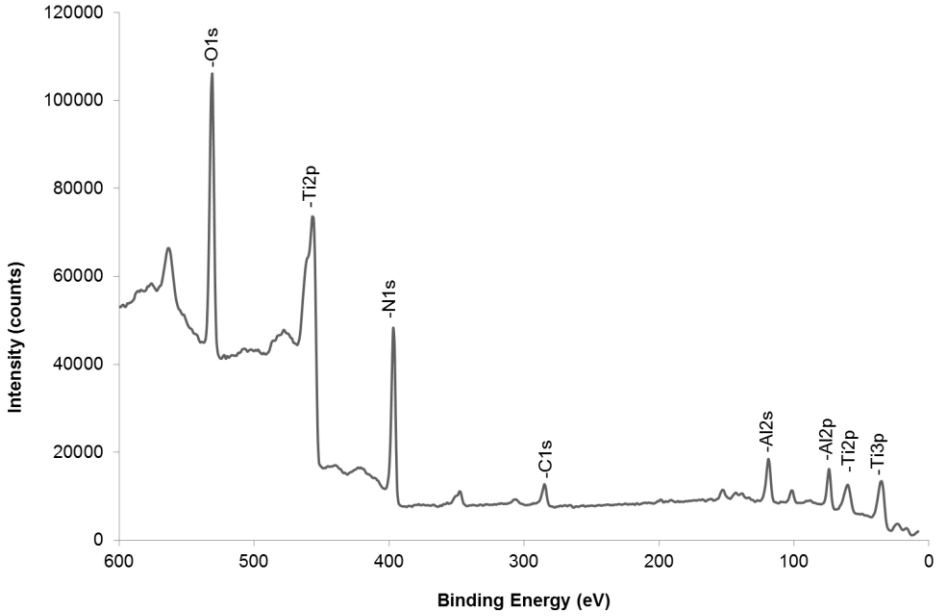


Figure 4.20: XPS spectra of the surface layer of the non-implanted cutting tool insert.

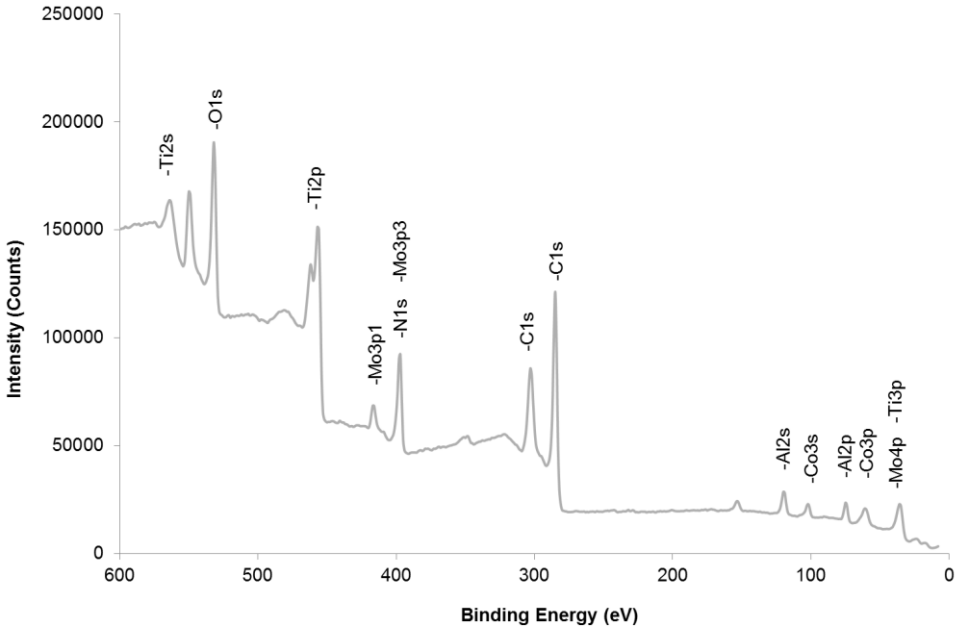


Figure 4.21: XPS spectra of the surface layer of the Ru + Mo ion implanted cutting tool insert at implantation dosage of 2E+16 ions/cm^2 at 120 keV.

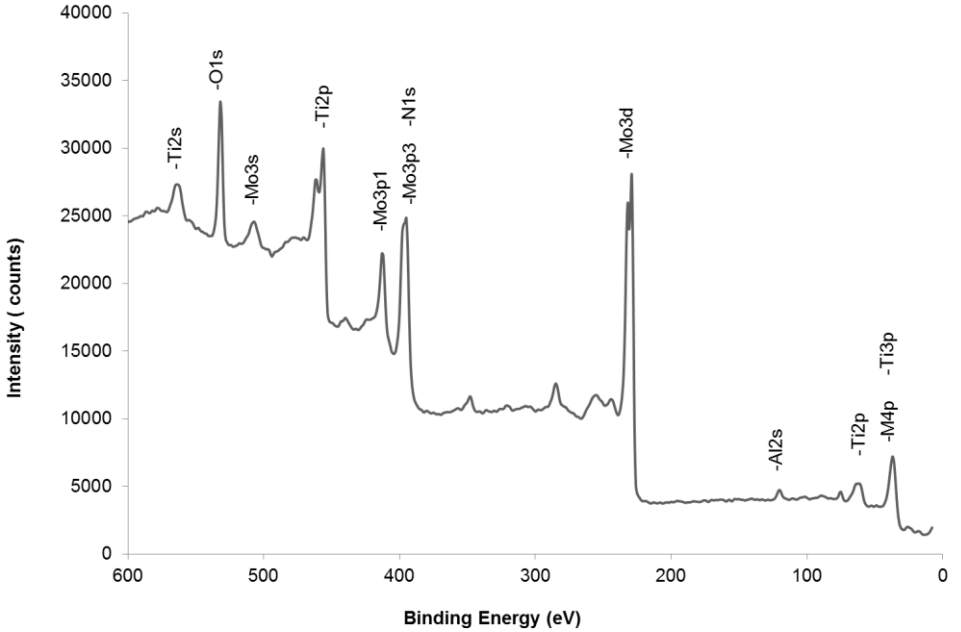


Figure 4.22: XPS spectra of the surface layer of the Ru + Mo ion implanted cutting tool insert at implantation dosage of 1E+17 ions/cm^2.

4.3.8 Time of Flight Secondary Ion Mass Spectroscopy

The quantity and depth of the Ru and Mo elements into the coated inserts was studied using TOFSIMS. Figure 4.23 shows the distribution of elements in the non-implanted inserts, while Figure 4.21 and Figure 4.22 show the distribution of the Ru and Mo in the coated inserts implanted with dosages of 5E+15 and 2E+16 ions/cm^2 respectively The TOFSIMS results of the remaining coated inserts can be found in Appendix D. In the figures the y-axis 'Intensity' represents the amount of each element at a specific distance below the material surface, while the x-axis 'Time' indicates the depth in nm, where two thousand seconds represent 125 nm. Figure 4.23 shows that amount of Ti started decreasing after 10 000 s (0.625 µm or 625 nm), amount of Al starts increasing after 4 000 s (0.25 µm or 250 nm), amount of N remains relatively low and uniform, amount of W and Co starts increasing after 10 000 s (0.625 µm or 625 nm). This is a result of the TiN and TiAlN coating. Figure 4.24 and Figure 4.25 shows that the amount of Ru and Mo behaved the same despite the different ion implantation dosage, Ru intensity is low just below the surface and it starts increase after 4 000 s (0.25 µm or 250 nm).

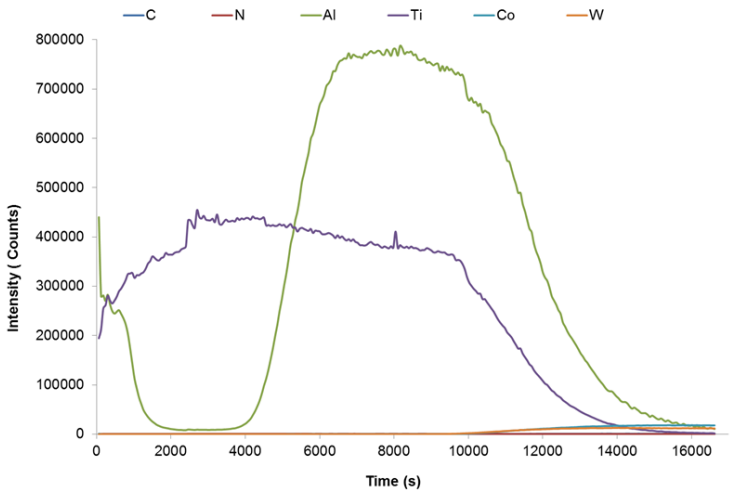


Figure 4.23: TOFSIMS results of the non-implanted cutting tool inserts.

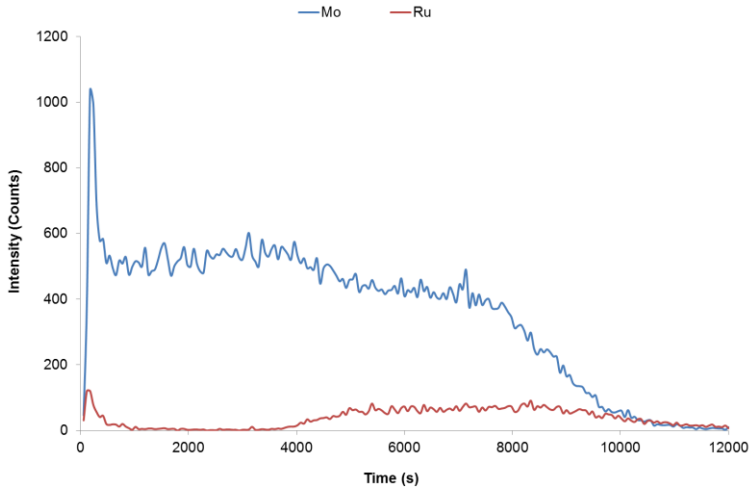


Figure 4.24: TOFSIMS results of the cutting tool inserts implanted at an ion implantation dosage of the 5E+15 ions/cm^2.

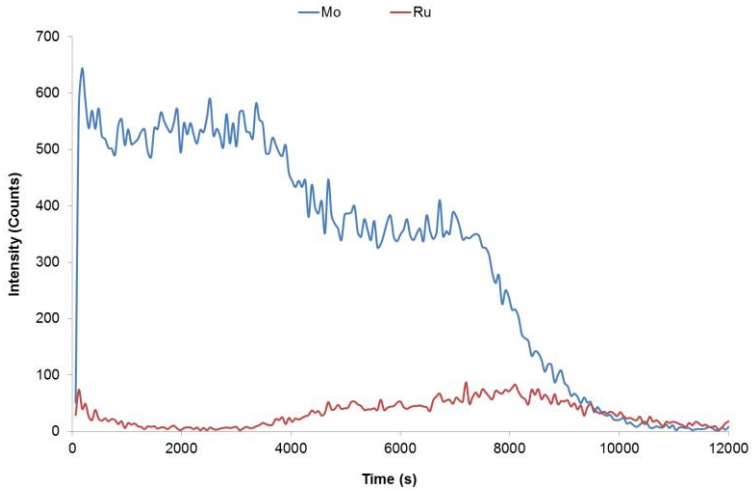


Figure 4.25: TOFSIMS results of the cutting tool inserts implanted at an ion implantation dosage of 2E+16 ions/cm^2.

4.4 Face Milling Test Results

4.4.1 Machining Analyses

The induced cutting forces experienced by the tool inserts during machining are shown in Figure 4.26 for both the coated and uncoated inserts. An increase in cutting force of 3 to 14% and a negligible (1 to 2%) decrease in the coated inserts was observed. The decrease in cutting forces was experienced by inserts ion implanted at 2E+16-120 keV and 1E+17 ions/cm^2. The relationship between cutting forces and the ion implantation dosage was not linear, as the highest cutting forces were experienced at ion implantation dosages of 5E+15 and 2E+16 ions/cm^2. A 5% increase in cutting force and a decrease of 3 to 16% was observed for the uncoated cutting tools. The relationship between the ion implantation dosage and the cutting force of the uncoated inserts was not linear as well. The insert ion implanted using the acceleration voltage of 120 keV experienced the highest cutting forces and all the other ion implantation dosages experienced low cutting forces compared to the non-implanted insert. The coated non-implanted insert experienced low cutting forces compared to the non-implanted uncoated insert and most of the ion implanted uncoated inserts except for the inserts implanted at 2E+16 ions/cm^2.

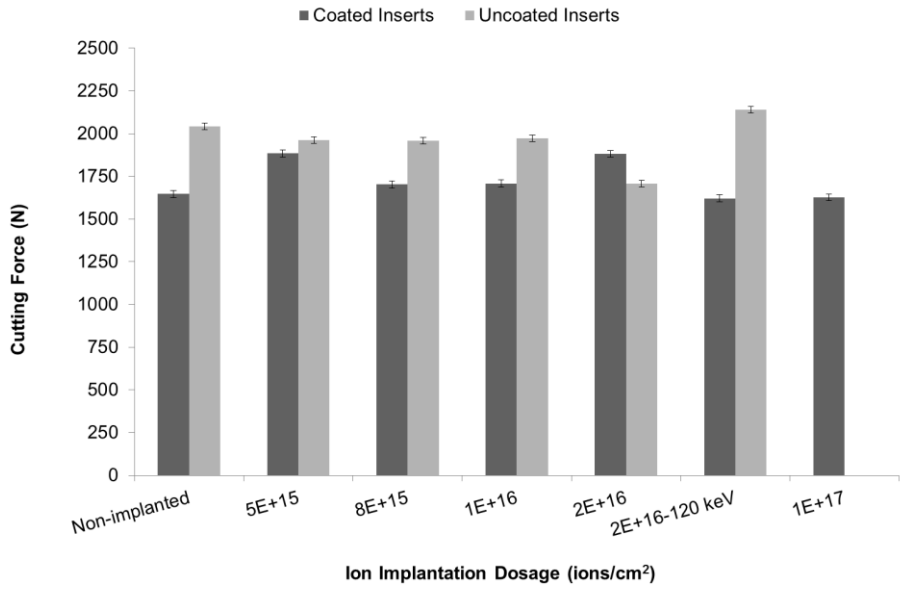


Figure 4.26: Induced cutting forces experienced by cutting tool inserts during machining.

The average heat generated at the tool-workpiece interface during machining is shown in Figure 4.27 for both the coated and uncoated inserts. An increase in heat generated of 1 to 22% and a decrease of 4 to 37% were observed in the coated inserts. An increase in heat generated of 31 to 44% was observed for the uncoated inserts. The relationship between heat generated at tool-workpiece interface and the ion implantation dosages in both sets of inserts was not linear.

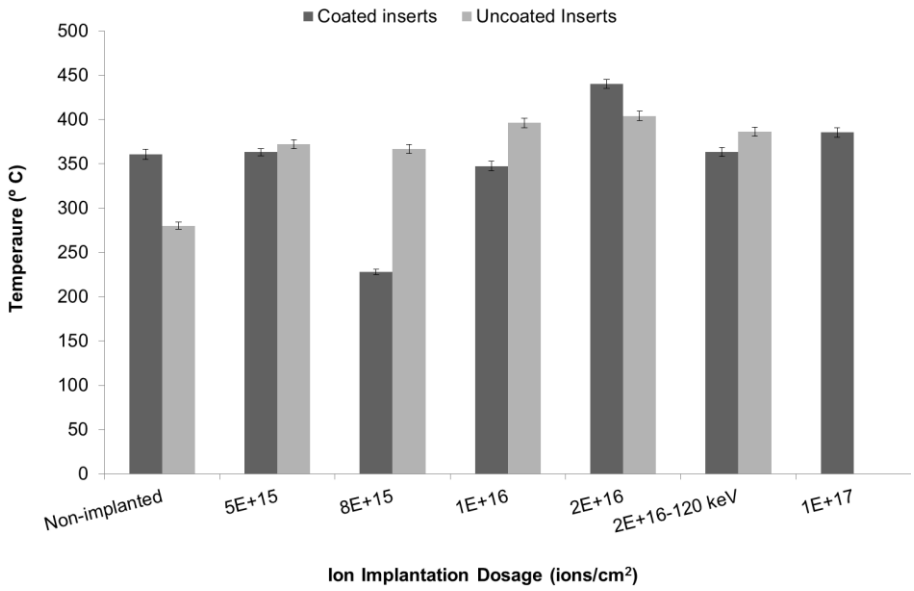


Figure 4.27: Heat generated at the tool–workpiece interface during machining.

Figure 4.28 shows the flank wear (VB) of the inserts at different ion implantation dosages. The non-implanted insert had the largest flank wear compared to the ion implanted inserts, this is complemented by Figure E.0.1 in Appendix E as it shows the largest width of the bright area (showing abrasion of coating) compared to the rest of insert. A 61% decrease in flank wear was observed for the ion implantation dosage of 5E+15 ions/cm^2. However, from the ion implantation dosage of 8E+15 to 2E+16-120 keV there is linear trend in flank wear increase of ± 10%. A sharp decrease of 58% in flank wear was observed at the ion implantation dosage of 1E+17 ions/cm^2. Increasing the acceleration voltage resulted in 26% decrease in the flank wear, however the flank wear was still 23% higher compared to the insert implanted at the same dosage using 100 keV. The flank wear of the uncoated inserts could not be measured due to the excessive chipping on the cutting edge that extended to the flank face as shown by Figure E.0.2 in Appendix E.

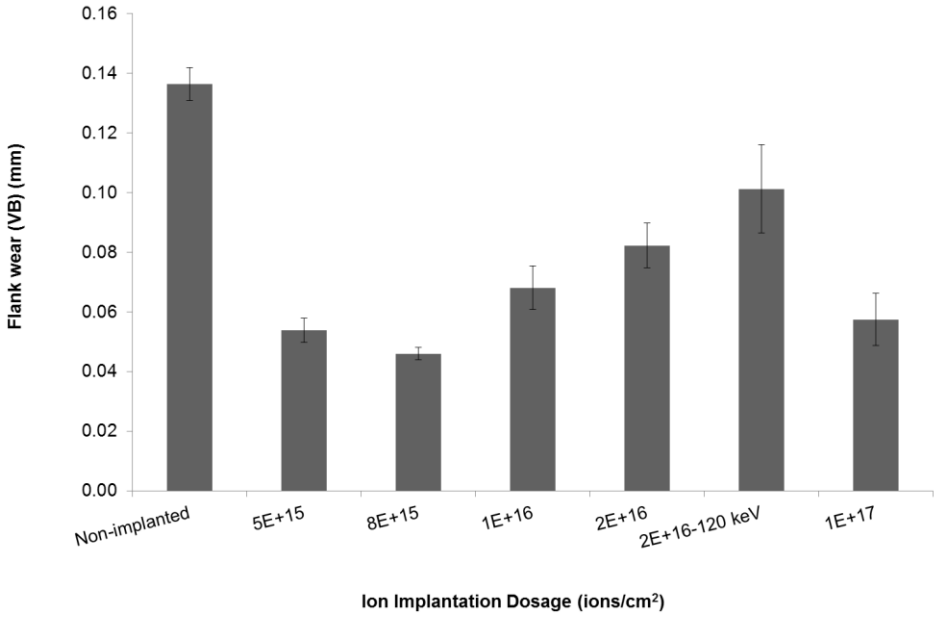


Figure 4.28: Flank wear (VB) of the coated cutting tool inserts.

Residual stress analyses were only limited to the coated inserts and the results are shown in Figure 4.29. A decrease in residual stresses of 36% after machining was observed in the non-implanted inserts. An increase in residual stresses of 14 to 47% occurred in the ion implanted inserts, however, the cutting tool inserts implanted at 2E+16 ions/cm^2 had residual stresses decrease after machining. This was observed also for the inserts implanted at 2E+16–120 keV. The maximum decrease in residual stresses after machining was observed in the cutting tool inserts implanted at 2E+16 ions/cm^2, minimum increase in residual stresses after machining was observed at an ion implantation dosage of 8E+15 ions/cm^2.

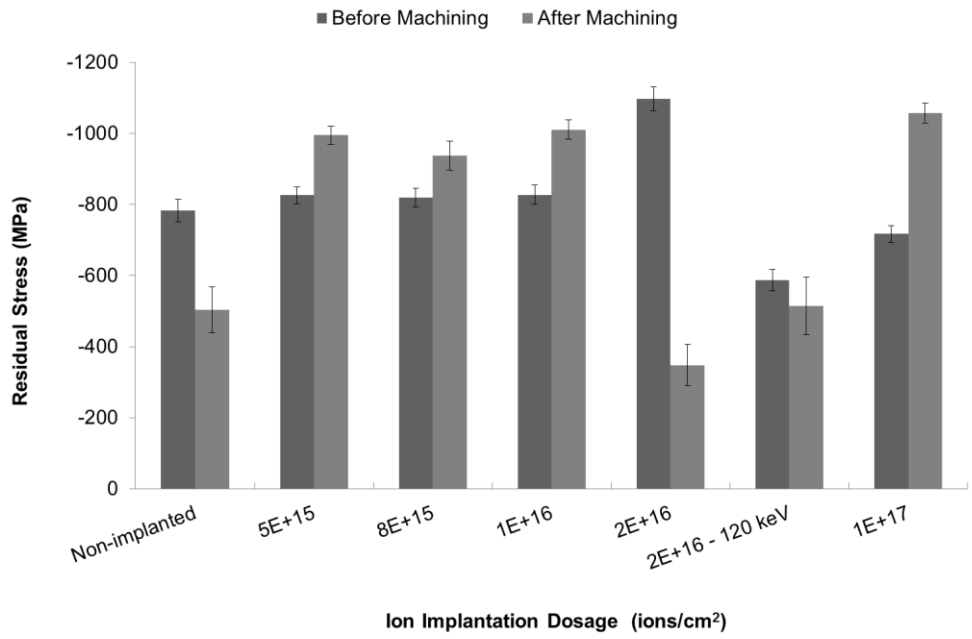
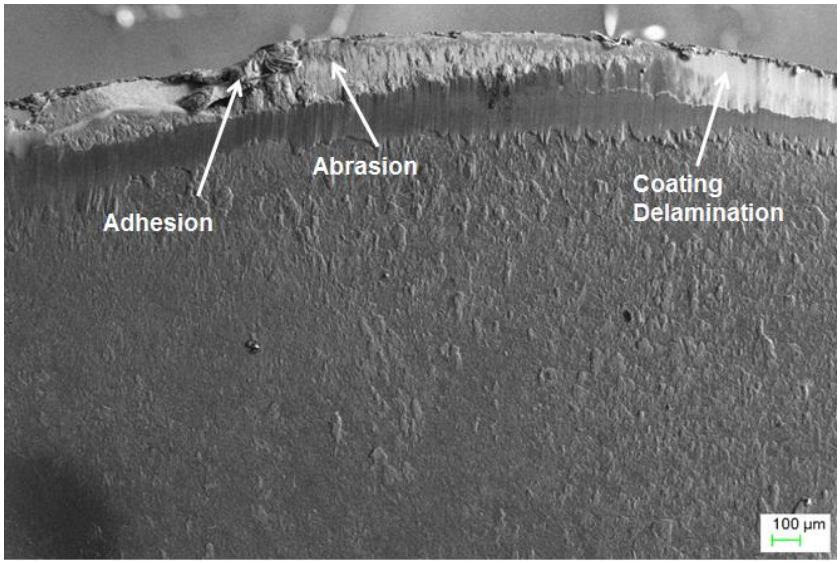


Figure 4.29: Residual stress measurements in the coated inserts before and after machining.

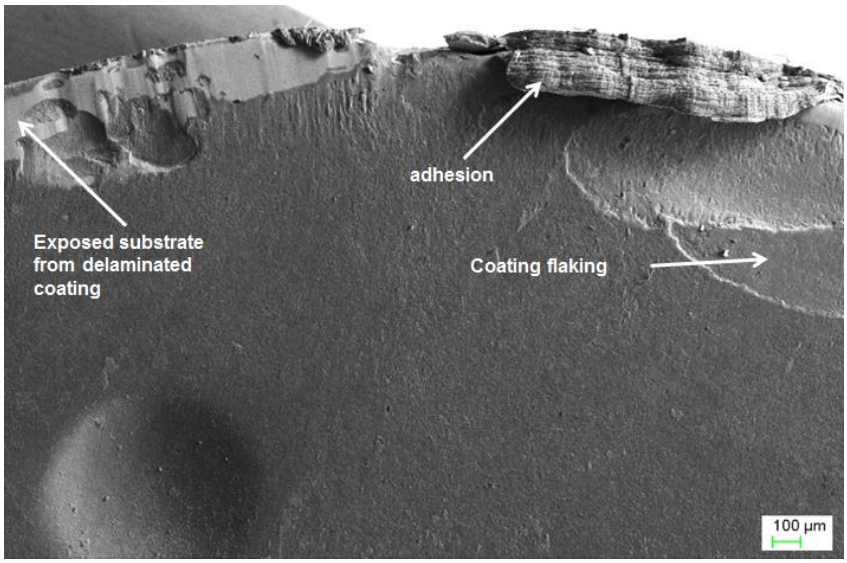
4.4.2 Tool Inserts Failure Mechanisms

Figure 4.30 shows the failure mechanisms experienced by both sets (coated and uncoated) of non-implanted cutting tool inserts on the rake face. Abrasion, flaking, coating delamination and chipping were the common failure mechanisms experienced by the non-implanted coated cutting tool inserts as shown in Figure 4.30 (a) and (b). Adhesion of cutting chips occurred after delamination or abrasion of the coating [76]. Excessive chipping extending to the cutting edge and flaking were the common failure mechanisms experienced by the uncoated non-implanted cutting tool inserts as shown in Figure 4.30 (c) and (d). As expected, an increase in cutting chips adhesion on the rake face was observed due to the uncoated surface.

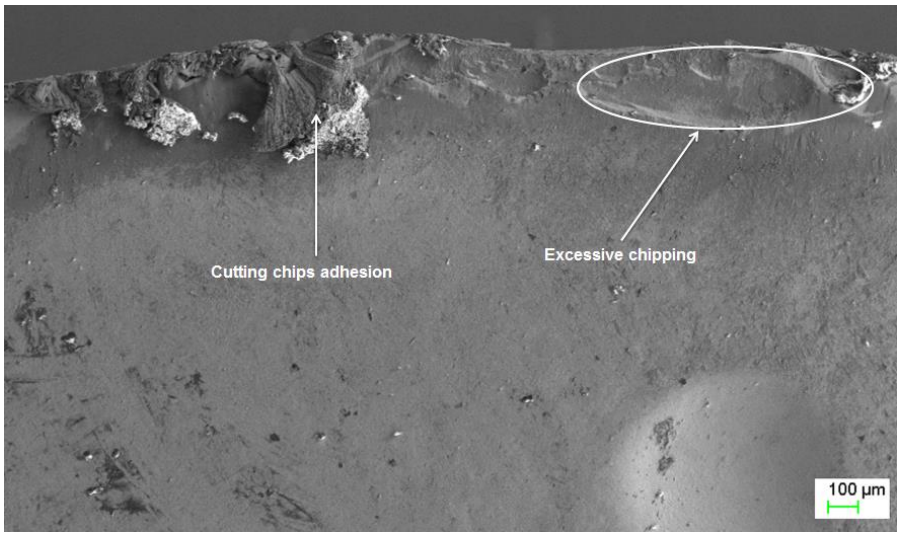
(a)


Adhesion
Abrasion
Coating
Delamination
100 µm

(b)


Exposed substrate
from delaminated
coating
adhesion
Coating flaking
100 µm

(c)


Cutting chips adhesion
Excessive chipping
100 µm

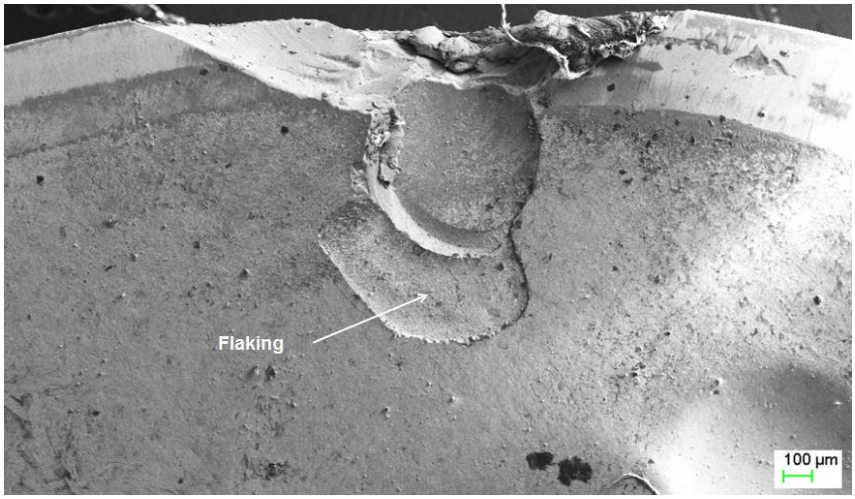
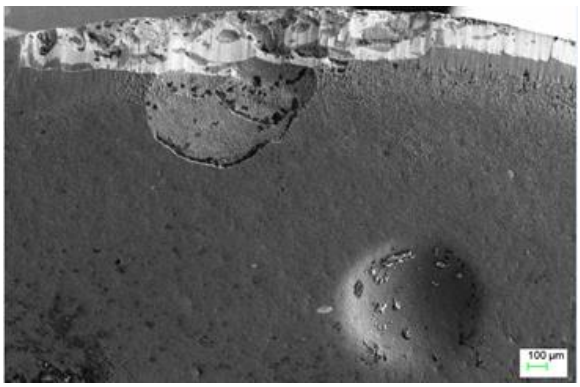
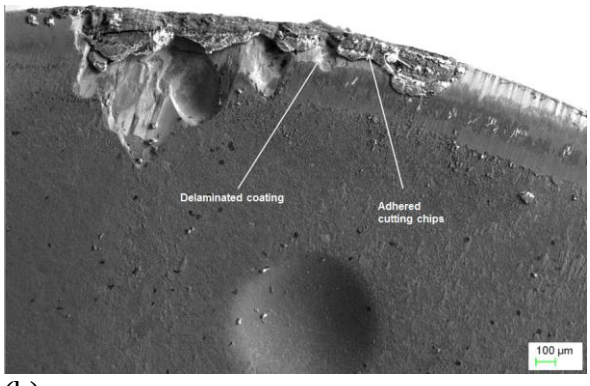
(d) 

Figure 4.30: (a) and (b) Failure mechanism experienced by the coated, (c) and (d) failure mechanisms experienced by the non-implanted uncoated cutting tool inserts on the rake face.

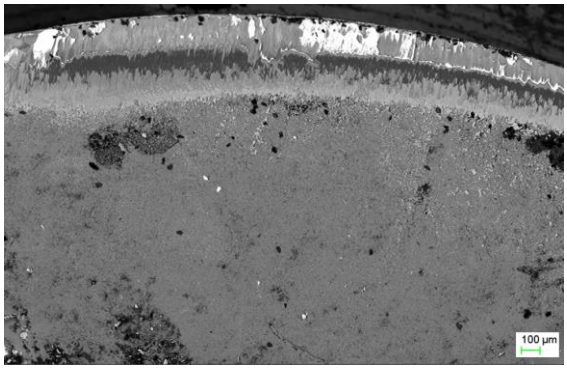
Figure 4.31 shows the failure mechanisms experienced by the ion implanted inserts. The inserts experienced (Figure 4.31 (a), (b) and (d)) abrasion, flaking and delamination of the coating, subsequently resulting in adhesion of the cutting chips as shown in Figure 4.31 (b). Minor smearing of the cutting chips on the rake face was observed as shown in Figure 4.31 (c). The abrasion on the rake face, some abrasion did not extend to the flank face as shown in Figure 4.31(c) as the coating provided protection from abrasion [33] (c) and (d). However for some inserts the abrasion extended to the flank face as shown in Appendix E. Not all of the 5 cutting tool inserts used per test experienced or failed at the same rate as some inserts did not fail at all just adhesion of the cutting chips as shown in Figure 4.31 (c) and Appendix F.



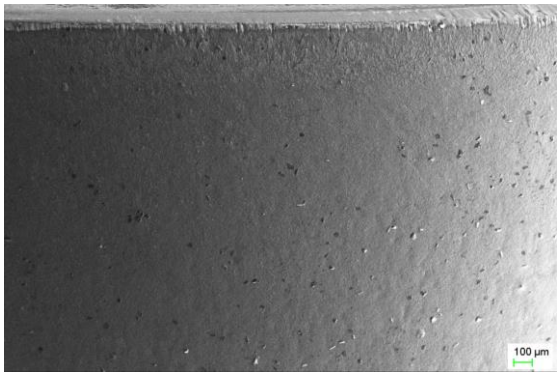
(a)



(b)



(c)



(d)

(e)

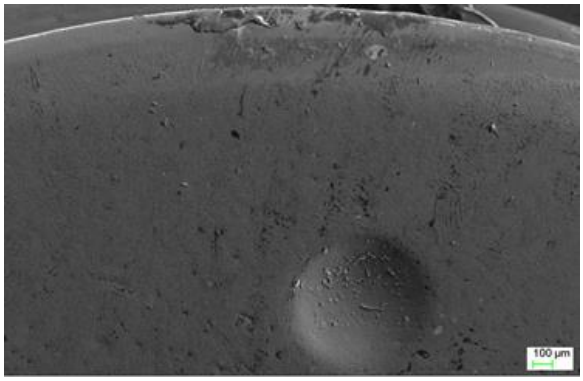
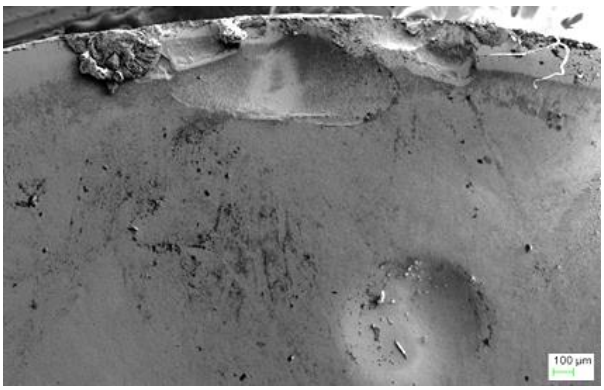
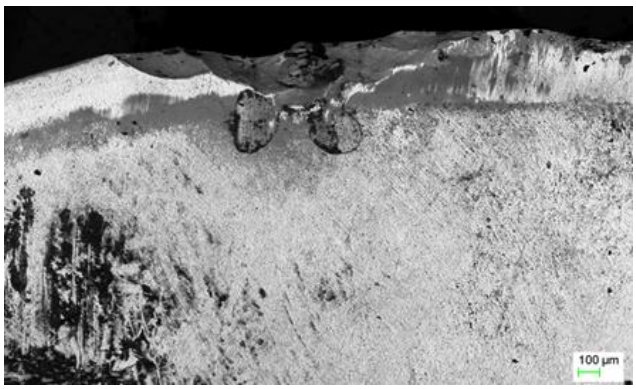


Figure 4.31: Failure mechanisms experienced by the coated ion implanted cutting tool inserts.

Figure 4.32 is the failure mechanism experienced by the uncoated ion implanted inserts. The uncoated ion implanted inserts experienced excessive chipping, flaking and cutting edge chipping as shown in Figure 4.32 (a), (b) and (c). Adhesion of the cutting chips was also observed. Thermal stress fatigue was observed as shown by the cracks perpendicular to the cutting edge as shown in Figure 4.32 (d). Similar to the coated ion implanted inserts, not all 5 inserts failed at the same rate as shown in Appendix F.



(a)



(b)

(c) (d)

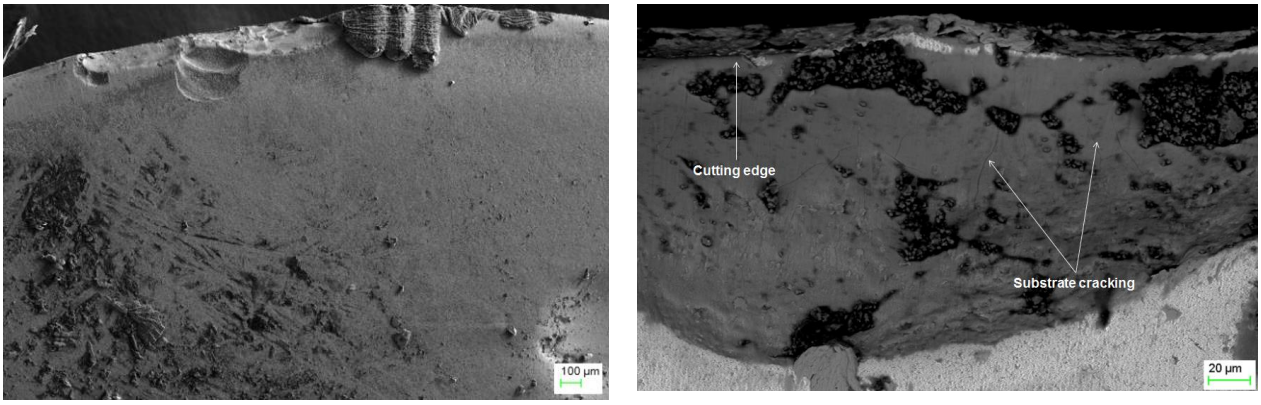
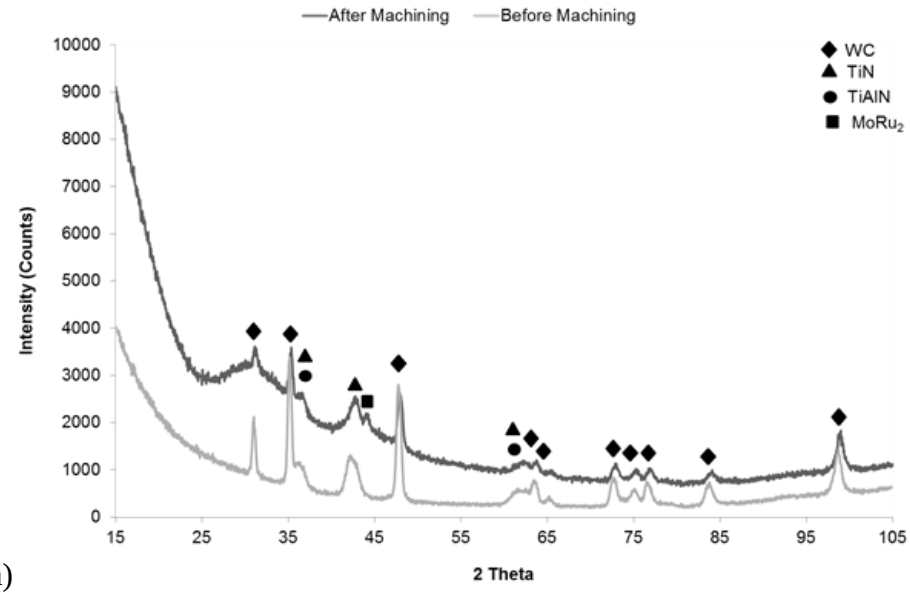
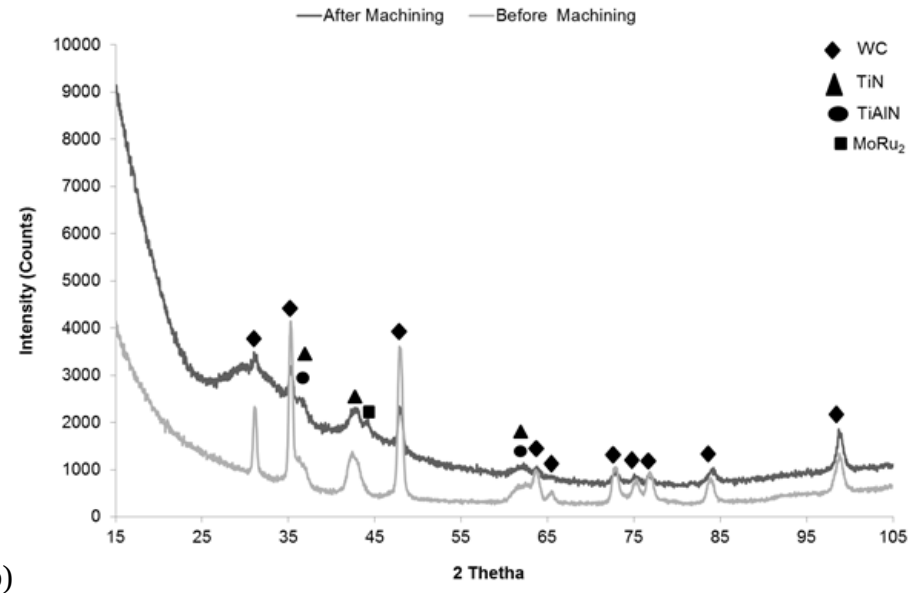


Figure 4.32: Failure mechanisms experienced by the uncoated ion implanted inserts.

Crystal phase analyses of the wear scar was limited to coated inserts and were conducted at a grazing incident angle of 5 °C. Figure 4.33 shows the diffraction patterns of the 2E+16 ions/cm^2 ion implantation dosages done at acceleration voltages of 100 and 120 keV respectively. The formation of a MoRu alloy was detected in both alloys after machining. This alloy formation was not found in the GIXRD patterns of the remaining alloys shown in Figure 4.34 .



(a)



(b)

Figure 4.33: GIXRD pattern using ion implantation dosage of 2E+16 ions/cm^2 (a) 100 and (b) 120 keV.

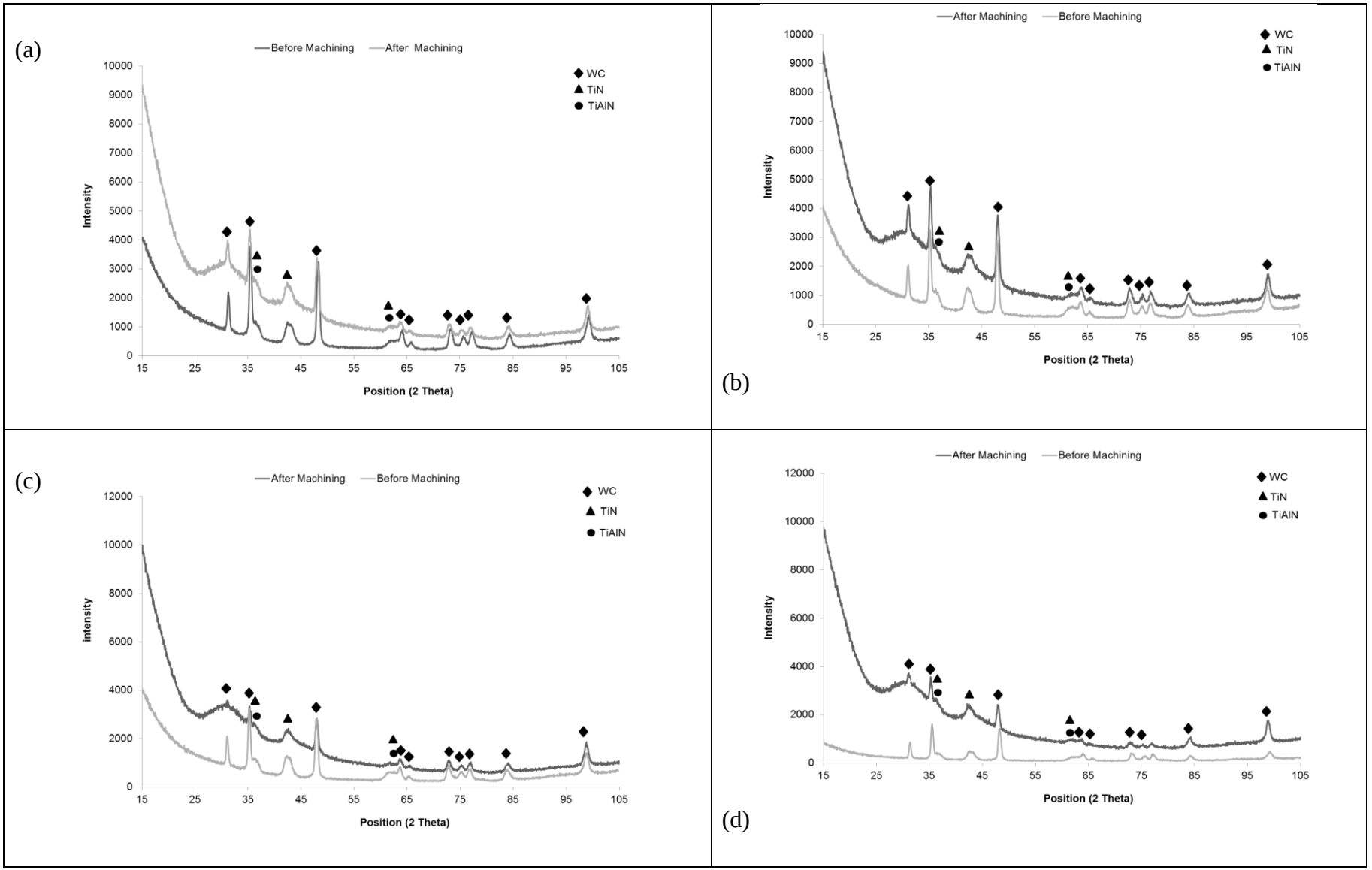
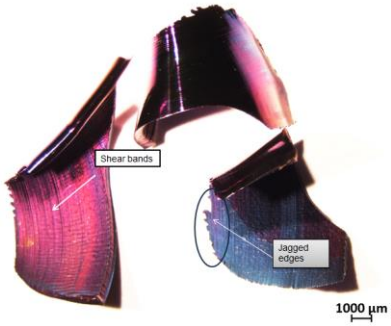


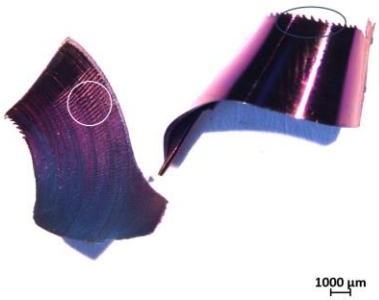
Figure 4.34:X-ray diffraction pattern (a) 5E+15, (b) 8E+15, (c) 1E+16 and (e) 1E+17 ions/cm^2.

4.4.3 Cutting Chips Analyses

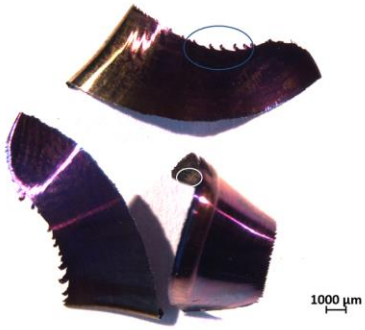
Figure 4.35 and Figure 4.36 are images of the cutting chips collected during machining process of the coated and uncoated inserts respectively. The colours of both sets of chips varied from golden brown to purple, blue and darker blue which indicated that most of the heat generated was absorbed by the cutting chips [86]. The cutting chips of the coated inserts shown in Figure 4.35 (a) to (g) were generally semi-continuous with jagged edges; the images show both the free surface (matt with shear fronts) and back surface (smooth and shiny surface). The cutting chips of the uncoated inserts shown in Figure 4.36 (a) to (f) were generally discontinuous with jagged edges; the images show both the free surface (matt with shear fronts) and back surface (smooth and shiny).



(a)



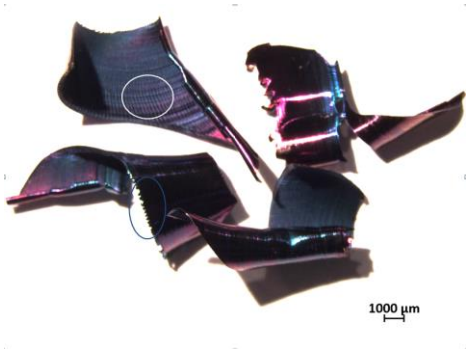
(b)



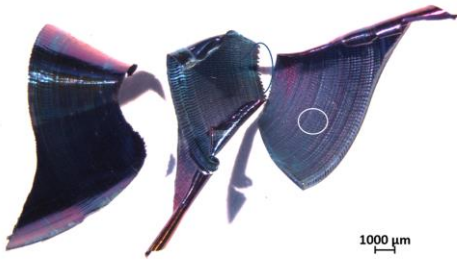
(c)



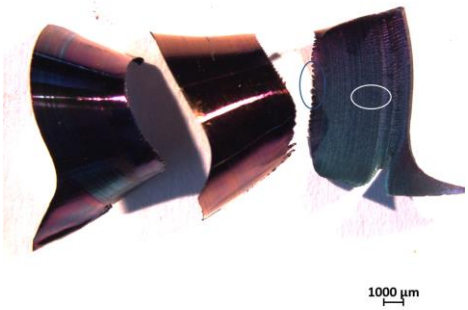
(d)



(e)



(f)

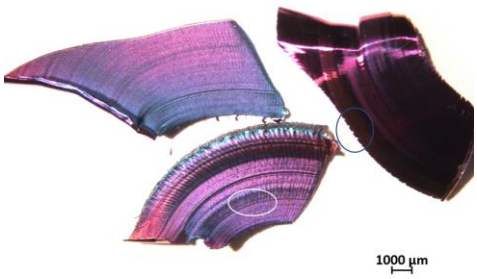


(g)

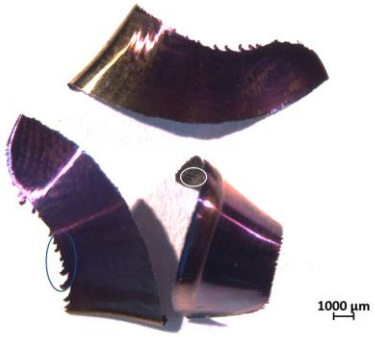
Figure 4.35: Purple to dark blue cutting chips collected while using different coated cutting tool inserts (a) non-implanted, (b) 5E+15, (c) 8E+15, (d) 1E+16, (e)2E+16 and (f) 1E+17 ions/cm^2 at 100 keV. (f) 2E+16 ions/cm^2 at 120 keV.



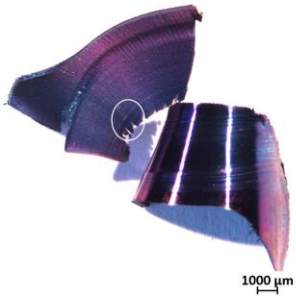
(a)



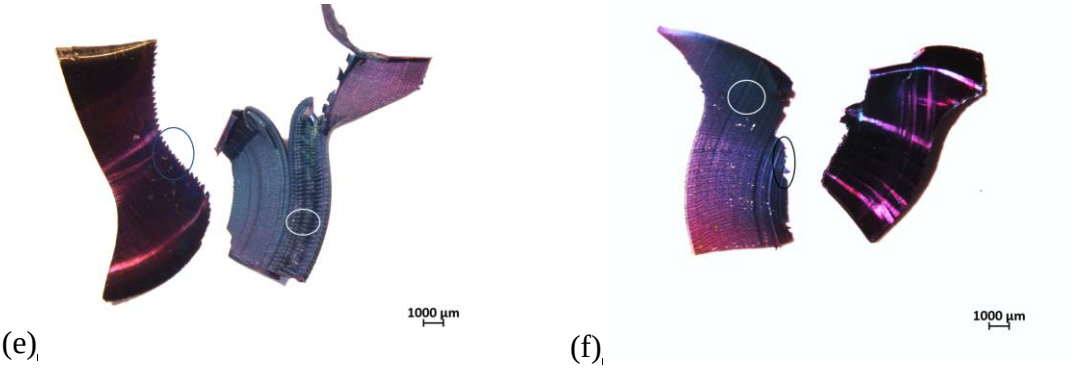
(b)



(c)



(d)



(e) (f)

Figure 4.36: Blue to purple cutting chips collected while using different uncoated cutting inserts (a) non-implanted, (b) 5E+15, (c) 8E+15, (d) 1E+16, (e)2E+16 and (f) 1E+17 ions/cm^2 at 100 keV. (f) 2E+16 ions/cm^2 at 120 keV, the circles show the jagged edges and the shear fronts.

The cutting chip compression ratio (ς) was calculated using Equation 4.1 where $t_1$is the undeformed chip thickness (feed per tooth) and t_2 is the deformed chip thickness (measured using a Vernier Callipers). The ζ results are shown in Figure 4.37 for both sets of inserts where ς was found to be less than 1 for all the cutting tool inserts except the uncoated insert ion implanted at 1E+16 ions/cm^2, which was exactly 1. The relationship between chip compression ratio and ion implantation dosages for both sets of inserts was not linear. An increase in compression ratio of 1 to 7% and a decrease in compression ratio of 1 to 6% were observed in the coated inserts. An increase in chip compression ratio of 9 to 53% was observed in the uncoated inserts and the chip compression ratio at the ion implantation dosage of 8E+15 ions/cm^2 was the same as that of the non-implanted uncoated inserts.

$$\varsigma = \frac{t_1}{t_2} \qquad \text{Equation 4.1}$$

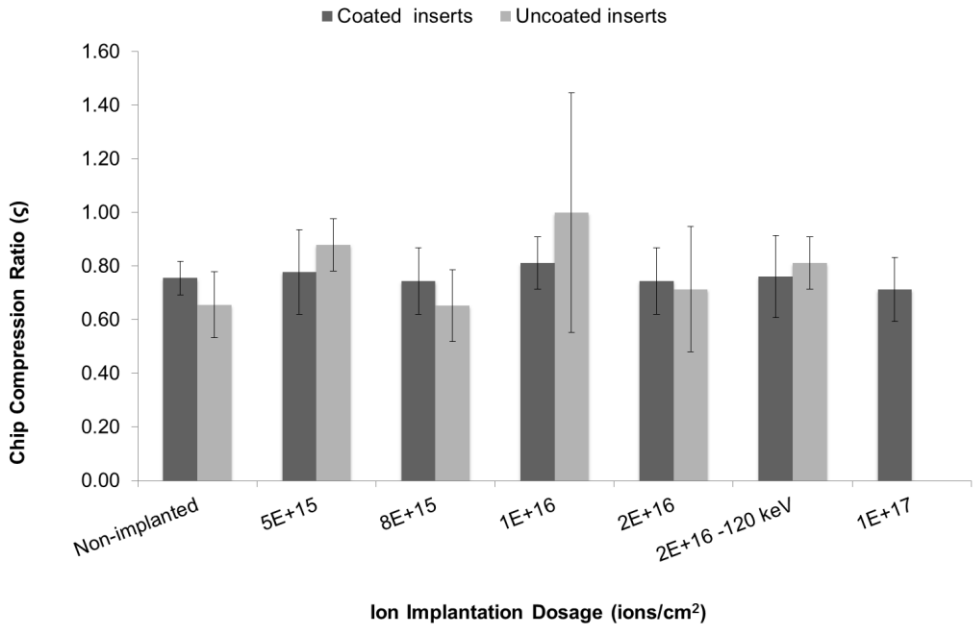


Figure 4.37: Chip compression ratios of the cutting chips collected during machining.

The phases of the cutting chips were examined using XRD and the results are shown in Figure 4.38. The diffraction pattern shows the cubic Fe.

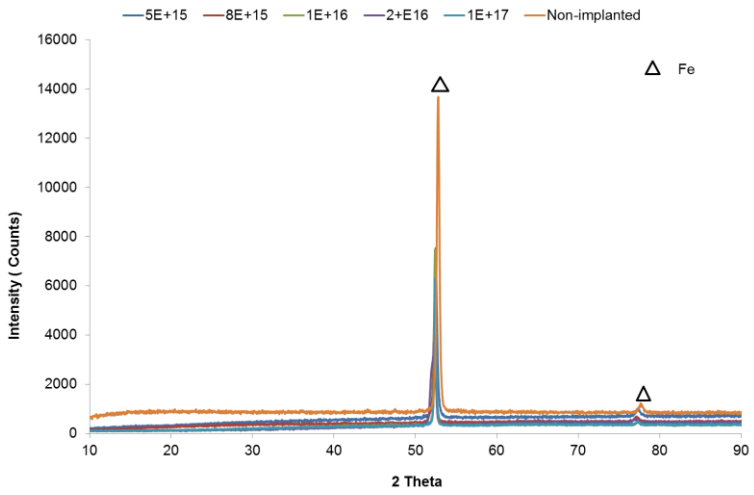


Figure 4.38: X-ray diffraction pattern of the cutting using different cutting inserts as indicated on the graph.

The microscopic analyses of the free surface of the cutting chips are shown by FESEM micrographs in Figure 4.39 to Figure 4.40. The cutting chips generally had shear bands and a lamellar structure.

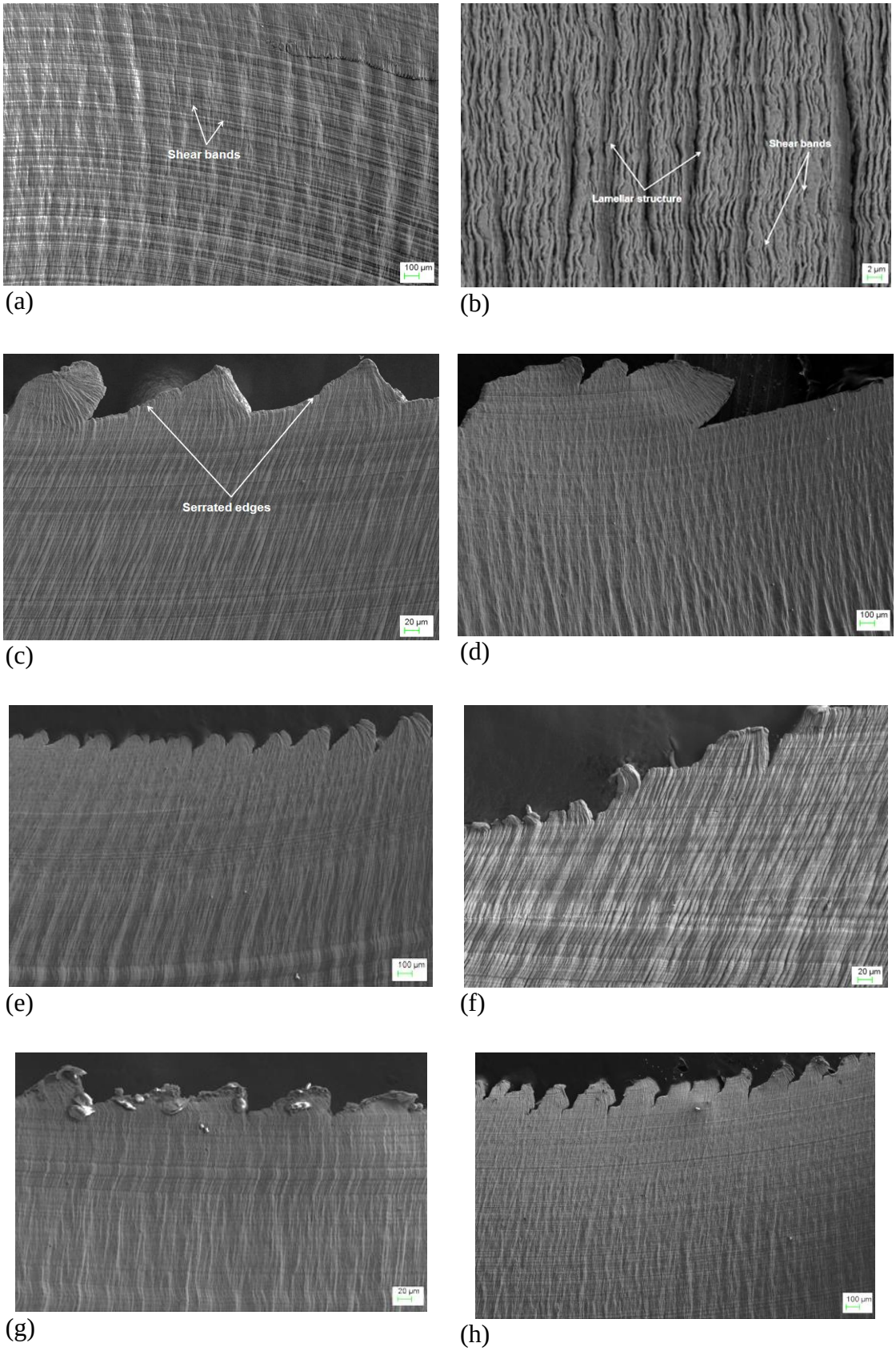


Figure 4.39: FESEM micrographs of the cutting chips free surface of the coated cutting tool inserts (a) and (b) non-implanted, (c) 5E+15, (d) 8E+15, (e) 1E+16, (f)2E+16 and (h) 1E+17 ions/cm^2 at 100 keV. (g) 2E+16 ions/cm^2 at 120 keV.

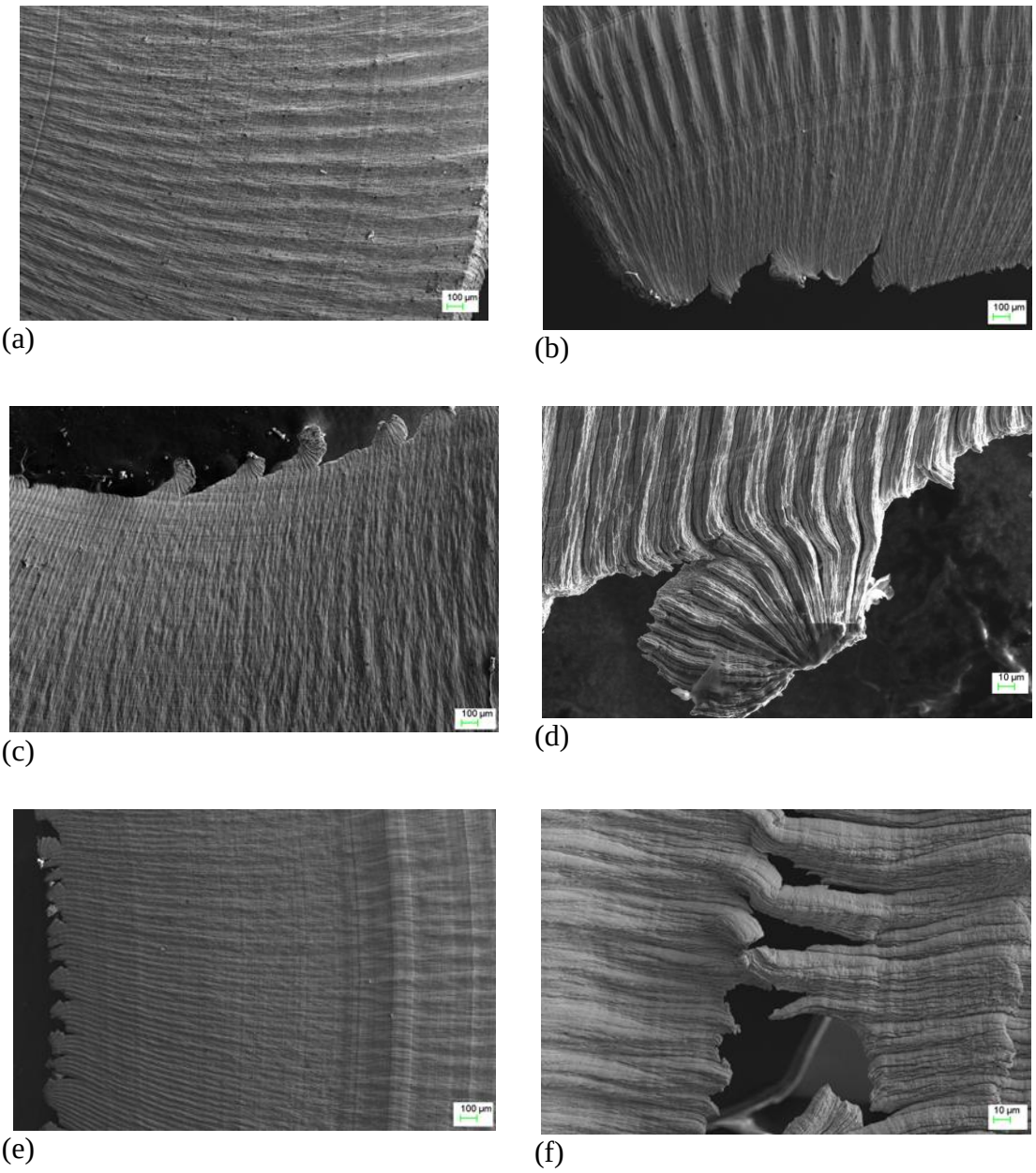


Figure 4.40: FESEM micrographs of the cutting chips free surface of uncoated tool inserts (a) non-implanted, (b) 5E+15, (c) 8E+15, (d) 1E+16, (e)2E+16 ions/cm^2 at 100 keV and (f) 2E+16 ions/cm^2 at 120 keV.

4.4.4 Steel Machined Surface Analyses

The characterisation tests of the machined steel surfaces were limited to the machining tests conducted using the coated inserts. Figure 4.41 shows the average surface roughness of the machined surface as a function of the different inserts used during machine. The surface roughness (Ra) of the coated inserts was similar to that of the non-implanted inserts. The highest surface roughness increase was observed when using inserts ion implanted at 2E+16 ions/cm^2.

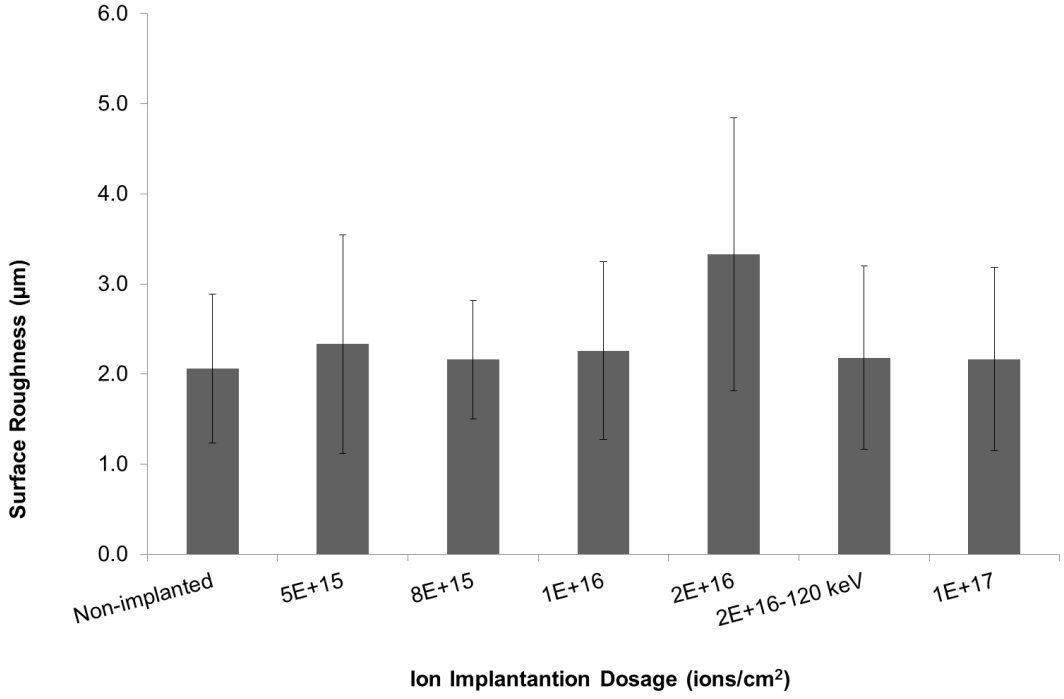


Figure 4.41: Surface of the workpiece at different ion implantation dosages.

Figure 4.42 shows the XRD analyses of the machined steel surface while Figure 4.43 shows FESEM images of the microstructure of the machined steel. The x-ray diffraction pattern analysis in Figure 4.42 shows that the crystalline phase of the workpiece did not change during machining as only the Fe peak was identified. There was no difference in the microstructure at the different ion implantation dosages including the non-implanted inserts. The microstructure shows undissolved carbides in the grain boundaries.

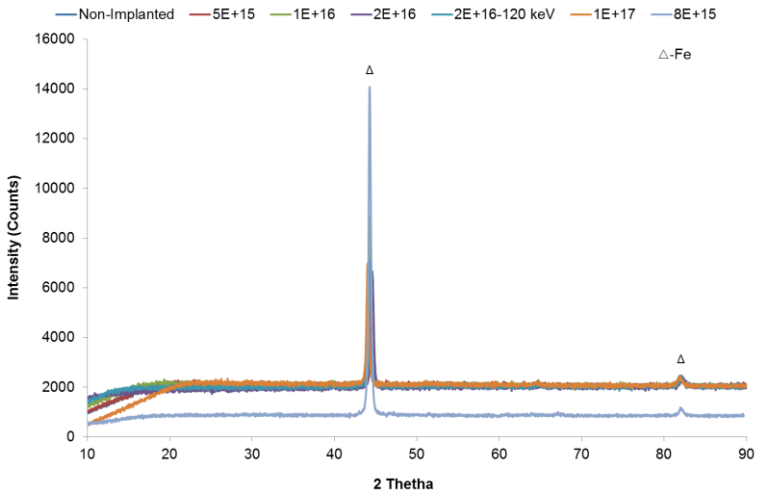
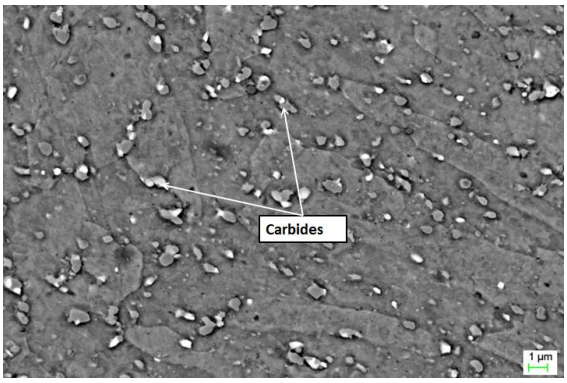
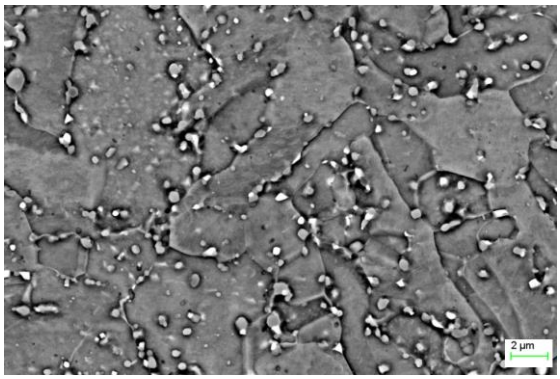


Figure 4.42: X-ray diffraction pattern of the workpiece machined surfaces.

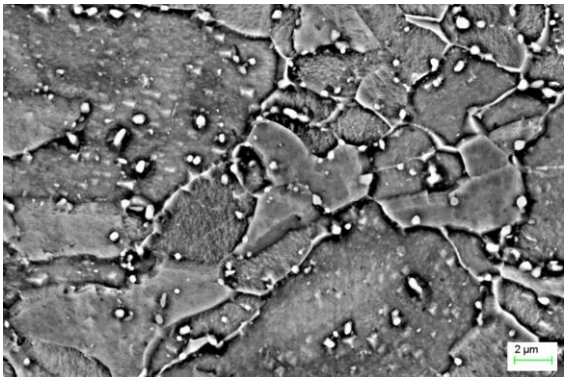
(a)



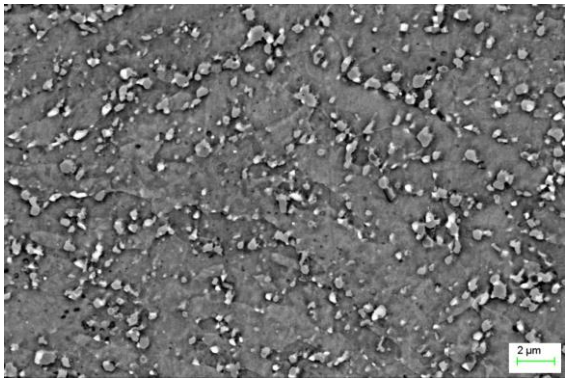
(b)



(c)



(d)



(e)

(f)

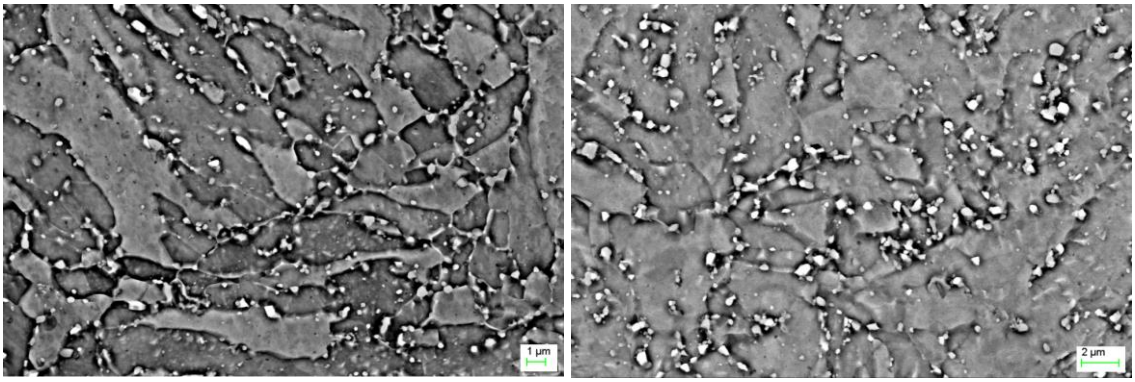


Figure 4.43: FE-SEM micrographs of the machined workpiece using different cutting tool inserts (a) non-implanted, (b) 5E+15 , (c) 1E+16, (d) 2E+16 and (f) 1E+17 ions/cm^2 at 100 keV and (e) 2E+16 ions/cm^2 at 120 keV.

Chapter 5 Discussion

This chapter provides an in-depth analysis of the results reported in Chapter 4 by discussing the effect of Ru and Mo ion implantation on the material properties and machining performance WC-6wt%Co coated and uncoated inserts.

5.1 Influence of Ru and Mo ion implantation on the material properties of WC-6wt%Co cutting tool inserts

5.1.1 Coated cutting tool inserts

The purchased coated cutting tool inserts were ion implanted at five different ion implanted dosages at an acceleration voltage of 100 keV and single ion implanted dosage of 2E+16 ions/cm^2 using an acceleration voltage of 120 keV. There was no visible change in the substrate microstructure of the implanted cutting tool inserts at all the ion implantation dosages as shown by the FESEM micrographs in Figure 4.3 and Appendix A, as the effect of ion implantation is known to go a few microns beyond the ion implanted zone [18, 47].

The acceleration voltage of the implanted ions decreases as it moves in the target; this is due to the collisions with target atoms. Therefore, the concentration of the ion implanted elements is expected to be higher on the surface and decrease as the ions move towards the core or centre of the target [18]. This was supported by the TOFSIMS results as they show that the concentration (represent by the intensity) was decreasing with depth of penetration as shown in Figure 4.24 and Figure 4.25. The concentration on the surface increased with increasing ion implantation dosages except at ion implantation dosage of 1E+16 ions/cm^2, where concentration of Mo was lower compared to the previous ion implantation of 8E+15 ions/cm^2, as the dosages had intensity counts 600 and 700 on the surface respectively. This was further supported by the elemental composition using EDS in Figure 4.6 as it shows that Mo wt.% at 1E+16 was 5% lower than at 8E+15 ions/cm^2 and while Ru increased significantly by 57%. Since Ru and Mo were deposited simultaneously and the

instrument chose the element to deposit based on the atomic mass including all isotopes, Ru and Mo isotopes have overlapping atomic masses [87], there is high possibility that mostly Ru ions and its isotopes were deposited at the ion implantation dosage of 1E+16 ions/cm^2. This was inline with experimental setup as the Mo sputtering target was larger than that of Ru to ensure large surface area for Mo ions extraction. All the TOFSIMS results show that Mo was constantly higher compare to Ru and this was supported by elemental composition using EDS. The results also show that high implantation dosage resulted to high concentration of ions implanted into the surface compared to the low dosage, with intensity of the Mo for the cutting inserts implanted at 1E+17 ions/cm^2 100keV to be over 40% higher than that of Mo at the low dosages and not influence depth of penetration [18, 88]. This explains the composition of the Ru and Mo using EDS being lower on the cross section compared to the composition in the surface of the coating. Similar observation was made on the cross section when using elemental mapping as the Ru and Mo were not detected.

The Vickers micro-hardness of the ion implanted inserts in Figure 4.11 was higher that of non-implanted inserts. The increase in hardness was due to dislocation and defects movement resulting from energy transfer caused by the implanted ions [45–47]. There was no direct correlation between Vickers micro-hardness and the Ru and Mo dual ion implantation dosage, as shown in Table 5.1. The scatter relationship of the Vickers micro-hardness and the ion implantation dosage is mostly due to the different interaction between ion implanted atoms and that of the target [48, 50] depending on the position occupied by implanted ions whether interstitial or lattice site. Other factors such as ion implantation dosage also play a role in the scatter relationship. The insert ion implanted with dosage of 1E+17 ions/cm^2 experienced micro-hardness decrease due to critical dosage effect, where by ion implantation results to amorphization [52]. The Ru and Mo ion implantation increased the micro-hardness of the coated WC-Co cutting tool insert and hardness is an important property in wear resistance [4, 6].

Table 5.1: Vickers micro-hardness % increase of the ion implanted cutting tool inserts compared to non-implanted cutting tool inserts

Ion Implantation Dosage (ions/cm^2) at 100keV	% increase of Micro-hardness of ion implanted cutting inserts with respect to non-implanted cutting tool inserts
5E+15	29%
8E+15	32%
1E+16	30%
2E+16	24%
1E+17	5%

The surface roughness initially increased with increasing ion implantation dosage as shown in Figure 4.12. However, the surface roughness of the cutting tool inserts was within the allowable limit of less than 25 μm [61]. The surface roughness increased until the ion implantation dosage of 1E+16 ions/cm^2, the surface roughness is due to sputtering where some of substrate atoms are ejected during ion implantation [46]. Sputtering results in a formation of hillocks [89], as the ion implantation increases the ions starts hitting the hillocks until dynamic equilibrium is reached [45] where a maximum of 30% implanted atoms occupy the substrate, which subsequently reduces surface roughness [90].

The residual stresses after ion implantation were compressive as shown in Figure 4.15, the residual compressive stresses of the ion implanted cutting inserts were higher than that of the non-implanted cutting tool inserts. The increase in the residual stresses was due to the ion implanted atoms occupying the interstitial site and forming a crystal structure inside the substrate lattice structure, which resulted in swelling of the lattice structure which increased the compressive stresses [45, 49–51]. It was noted that the residual stress initially increased with an increasing ion implantation dosage until the ion implantation dosage of 2E+16 ions/cm^2 with residual stresses of 1097 MPa, which were 40% higher than that of non-implanted inserts. The residual compressive stresses at ion implantation dosage of 1E+17 ions/cm^2 started decreasing and it was 6% less than that of non-implanted inserts. The decrease in residual

compressive stresses was due to the high dosage and the long exposure to radiation (see Table 5.2) that resulted in an amorphous mess or lattice damage [91] causing the stresses to relax. The increased compressive stresses are advantageous during interrupted cutting, research has shown that compressive stresses increase fracture toughness as it is known to close micro-voids subsequently stopping propagation of cracks [45, 49].

Table 5.2: Ion implantation time at different ion implantation dosages.

Ion implantation dosage (ions/cm^2)	Time (min)
5E+15	12
8E+15	22
1E+16	30
2E+16	50
1E+17	150

During implantation the ions sometimes form bonds with the target atoms [88]. X-ray photoelectron spectroscopy (XPS) was used to identify the compounds present after ion implantation. The XPS results of the coated inserts ion implanted at 2E+16 ions/cm^2 120 keV and 1E+17 ions/cm^2 100 keV are shown in Figure 4.21 and Figure 4.22 respectively. The binding energies showed presence of Mo based compounds in the ion implanted surface; this can be due to the Ru based compounds being below the detectable compounds limit. The binding energy and the elemental line spectra in conjunction with NIST X-ray Photoelectron Spectroscopy Database [92] were used to identify the compounds as shown in Table 5.3. Molybdenum did not form any compounds with the coating as it was only found in its oxide form and its pure state. Molybdenum oxide form is known to be lubricious.

Table 5.3: Chemical states.

Binding Energy	Elemental Spectra Line	Chemical compound
37.5	Ti 3p	TiO_2
40.5	-Mo 4p	MoO_3
119.3	Al 2s	Al_2O_3
229.2	-Mo 3d	MoO_2
395.6	-Mo 3p3	Mo
455.5	-Ti 2p	TiN
506.3	-Mo 3s	Mo
531.3	-O 1s	MoO_2
561.0	-Ti 2s	Ti

Due to sputtering that occurs during implantation, the ion implanted inserts had high crystallinity compared to the non-implanted cutting tool inserts as shown in Figure 4.16 and Figure 4.17. The surface oxidize over time as shown by the XPS results (Table 5.3) and the oxidized thin layer is not crystalline or too thin for the grazing incident angle to penetrate [16]. This explains the increase in crystallinity with increasing grazing incident angle. Since ion implantation exposes the surface below the non-crystalline oxide layer, it explains the presence of chemical states of the substrate in Figure 4.21 and Figure 4.22 as it shows chemical states of Co, while Figure 4.20 shows no chemical states of the substrate in the XPS results.

5.1.2 Effect of increased voltage during ion implantation

The concentration of the Ru and Mo for the ion implantation dosage of 2E+16 ions/cm^2 at 120 keV was lower than that of ion implantation dosage of 2E+16 ions/cm^2 at 100 keV as shown by the RBS results in Figure 4.8 and Figure 4.10 and elemental composition in Figure 4.6. This was due to depth of penetration increase by an increase in acceleration voltage [93], however, the increase in acceleration voltage at an ion implantation dosage of 2E+16 ions/cm^2 did not result to visible microstructural change in the substrate as shown by FESEM micrographs in Figure A.0.1 in Appendix A.

The increase in acceleration voltage resulted to reduced micro-hardness for the coated inserts; this is due to the depth of penetration. Although the concentration remain the same distribution changed, hence reduction in micro-hardness. The effect of increased acceleration voltage was different for the uncoated inserts. Overall the effect is similar, increased micro-hardness, the results are still dependant on the interaction of implanted ions and substrate atoms as well as the lattice structure [46, 47] The acceleration voltage did not influence the degree of crystallinity with respect to the 5 different grazing incident angles. In the uncoated cutting tool inserts acceleration affected the crystallinity of the insert as shown in Appendix C. The insert at 4 grazing incident angles (1°, 2 °, 3° and 5°) was mostly amorphous. The uncoated implanted insert at acceleration voltage of 100keV was only amorphous at grazing incident angle of 1° due to the beam deflection. Due to the instrument (D8) setup which result to x-rays shallow depth of penetration.

5.1.3 Comparison between coated and uncoated inserts

Both sets (coated and uncoated) of inserts showed an increase in the average Vickers micro-hardness. The average Vickers micro-hardness of the ion implanted uncoated inserts was higher than that of non-implanted inserts. However, no direct correlation was observed between Ru and Mo ion implantation dosage and the average Vickers micro-hardness as observed for the coated ion implanted cutting tools. Table 5.4 shows the% difference in the average Vickers micro-hardness between coated and uncoated inserts, which complements the average micro-hardness results in Figure 4.11. The average Vickers micro-hardness of the uncoated non-implanted cutting tool insert was 9% lower than that of the coated non-implanted inserts, i.e. the coating employed increase hardness of the cutting tool insert [6, 12, 32]. There was a negligible difference in average Vickers micro-hardness between the coated and uncoated inserts with ion implantation dosages, 5E+15, 8E+15, and 2E+16-120 keV ions/cm^2 as the difference was 1 and 3%. A 5% difference in average Vickers micro-hardness of the inserts with ion implantation dosage of 1+E16 ions/cm^2 was achieved. This difference is also result of interaction between implanted ions and substrate atoms or lattice structure.

Table 5.4: Average Vickers micro-hardness comparison between coated and uncoated ion implanted inserts.

Ion implantation dosage	Coated	Uncoated	% Difference
Non-implanted	1685	1558	9%
5E+15	1841	2012	-3%
8E+15	2088	2061	3%
1E+16	1922	2024	-4%
2E+16	1963	1930	5%
2E+16-120 keV	1887	1994	-1%

Similarly, both sets of cutting tool inserts showed an increase in surface roughness, however only 1 ion implantation dosage was used for the uncoated cutting tool inserts, and the surface roughness of both sets of inserts was within the allowable limit of 25µm [61]. The GIXRD pattern analysis showed that the ion implanted uncoated cutting tool inserts had high crystallinity compared to the coated inserts except for the cutting tool insert with ion implantation dosage of 2E+16 at 120 keV which was highly amorphous as discussed above. The crystalline phases of the Mo or Ru based phases were not detected for the uncoated ion implanted cutting tool inserts. The RBS spectra did not show Ru and Mo due to the difference in atomic masses, between Mo 95.94, Ru 101.07 and W 183.84 [94] and the quantity (intensity), Ru and Mo were significantly small compared to W.

5.2 Machining performance of coated cutting tool inserts

During each machining test, 5 inserts were used. Each test was 15 minutes long and 135000 mm^3 or $1.35x10^{-4}$ m^3 volume of material was cut, the tests were stopped after catastrophic failure on the rake face of the non-implanted insert, which was characterised by excessive chipping and flaking. This was then used as the benchmark for cutting duration. Induced forces were measured using a Kistler force plate and heat generated was estimated using a FLIR thermal imaging camera.

5.2.1 Coated Cutting tool inserts

An increase in induced cutting forces of the ion implanted inserts compared to the induced cutting forces of non-implanted inserts was observed as shown in Figure 4.26. These were contrary to expected results based on the inserts properties and the machining conditions. The average Vickers micro-hardness of the ion implanted inserts was higher than those of the non-implanted inserts and the machining tests were conducted under unlubricated conditions. Machining under unlubricated conditions keeps the workpiece relatively hot as 10-15% of the generated heat is absorbed by the cutter and the workpiece and the rest by cutting chips [95, 96]. Steel is known to decrease its hardness at elevated temperatures. Therefore, when a similar insert with increased Vickers micro-hardness is employed under similar machining conditions to those of non-implanted cutting insert with lower Vickers micro-hardness, the induced forces are to be lower. The increase in induced forces can be attributed to the increased shear area due to chipping of the cutting edge during machining [97] as result of fracture toughness reduction during the post processing (ion implantation) surface modification and that coated inserts have lower fracture strength [12].

The estimation of heat generated at the tool-workpiece interface is shown in Figure 4.27. There was no direct relationship between generated heat and the ion implantation dosages as a result of the factors involved in heat generation during machining. Heat generated at the tool and chip interface is a synergy of deformation during shearing mechanism, the surface roughness (Ra) of the inserts and worn out flanks which generates heat at the workpiece-tool interface [66]. Therefore, the final amount of heat generated is still dependant on the failure experienced by the cutting tool insert. This is clearly shown by the analysis of the each set of inserts at different ion implantation dosages of different dosages in the following section.

A set of non-implanted inserts experienced several failure mechanisms as mentioned in Section 4.4.2. These included abrasion, coating delamination, adhesion, flaking and chipping on the rake face, however, the chipping of the cutting edge and flank face was minimal. The progression of the inserts failure included oxidation of the coatings at temperatures above 450 °C [13, 82] as the tests were conducted in an oxidative environment (CNC machine doors were kept open). The impact resulting from

constant engaging and disengaging of the cutting tool insert with the workpiece resulted in oxidized coating cracking due to thermal fatigue and thermal stress since radial depth was 15 mm (30%) of the cutter [30]. Cracking of the coating resulted in coating delamination which exposed the WC-Co substrate and reduced lubrication, subsequently causing cutting chips or swarf adhesion onto the cutting tool insert substrate and subsequently flaking and chipping of the substrate on the rake face [6, 12, 32, 33]. This failure sequence was also observed in the ion implanted cutting tool inserts as shown in Figure 4.31 and Appendix F from Figure F.0.2 to Figure F.0.7.

Figure F.0.2 is the failure mechanism on the flank and rake face experienced by the cutting tool inserts implanted at the dosage of 5E+15 ions/cm^2. The inserts that experienced excessive chipping on the cutting edge of the rake face had the cutting edge chipping as shown in Figure F.0.2 (a) rake face and (b) flank face. However, the cutting edge of the cutting tool inserts that experienced abrasion and minor coating delamination on the rake face was not damaged as shown in Figure F.0.2 (c) and (d). The rest of the inserts that experienced abrasion and coating delamination only had cutting chips or swarf adhesion on the cutting edge and minor abrasion as shown in Figure F.0.2 (e) to (f). The minor cutting edge chipping explains the 4 and 1% increase of induced cutting forces and cutting temperature compared to those non-implanted inserts respectively. Cutting edge chipping increases shear area which increases the induced forces during cutting and the chipping edges generates friction heat [97].

The failure mechanism on the rake face shown in Figure F.0.3 experienced by the inserts implanted at 8E+15 ions/cm^2 shows (a) abrasion, coating delamination (c), minor cutting edge chipping (b), (d) and (e), although substrate chipping on the rake face was observed, it was minimal on the cutting edge and the flank face. The minimal damage on the cutting edge and the absence of the cutting chips or swarf adhesion on the rake face plus the increased in micro-hardness explains the 14% increase in induced forces (Figure 4.26) and 37% decrease in heat generated (Figure 4.27) respectively.

The failure mechanisms experienced by the inserts implanted at 1E+16 ions/cm^2 is shown Figure F.0.4. The inserts experienced coating delamination, flaking and chipping on the rake face that extended to the cutting edge (a) and (c). As mentioned

earlier that each set of cutting tool inserts did not experience similar failure mechanism or fail at the same rate, one of the cutting tool inserts (d) had microscopic abrasion as the failure could not be observed with the naked eye. Although the cutting chips or swarf adhesion was observed in most of the cutting tool inserts and cutting edge chipping, a 4% decrease in generated heat was observed and 4% increase in cutting forces. This may be due to the chipping and adhesion occurring at a later stage of cutting. Figure F.0.5 shows abrasion, coating delamination ((a)-(c)) and excessive cutting edge chipping (d) and (e) of the cutting inserts implanted at 2E+16 ions/cm^2. The excessive chipping of cutting edge, which increases shear area explains the 14% increase in induced forces during cutting and subsequently increasing estimated heat generated by 22% during cutting [30, 97].

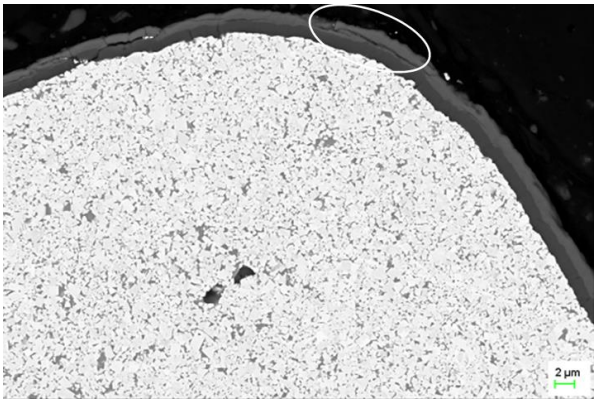
The failure mechanism on the rake face experienced by the cutting tool inserts implanted at 1E+17 ions/cm^2 shown in Figure F.0.7, show abrasion, delamination, adhesion and chipping of rake face that extends to the cutting edge and the flank face (b, d and e). However, the induced forces and estimated generated heat remained relatively low/similar to that of non-implanted inserts as the cutting force was negligible (1%) lower and estimated generated heat was 7% higher, which is probably due to the increased micro-hardness and the increased lubrication with formation of molybdenum oxides Figure 4.22 [16, 98].

The machining tests were stopped after catastrophic failure on the rake face as discussed in section 5.2. However, the inserts still experience flank wear in spite protection by the coating [33]. The ion implanted inserts experienced lower flank wear and width of the wear scar on the rake face of the ion implanted cutting tool inserts was lower compared to that of the non-implanted inserts. This can be attributed to the increased micro-hardness as shown in Figure 4.11 and the increased compressive stresses which are known close micro-crack propagation and improving fracture toughness of the cutting tools [99].

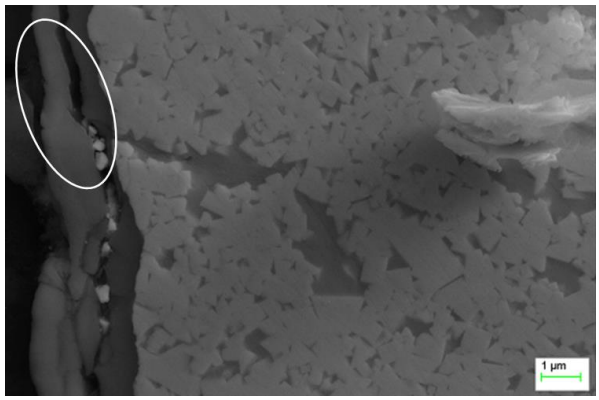
The residual stresses after machining test were studied per ion implantation dosage as shown in Figure 4.29. The residual stresses were compressive; the non-implanted cutting tool inserts' compressive stresses decreased after machining. However, the implanted cutting tool inserts that had compressive stress that was below 1000 MPa before machining showed an increase in residual stresses after machining. The

excessive chipping which was observed on the cutting edge extending to the flank face of the ion implanted cutting tool inserts explains the reduction in residual stresses.

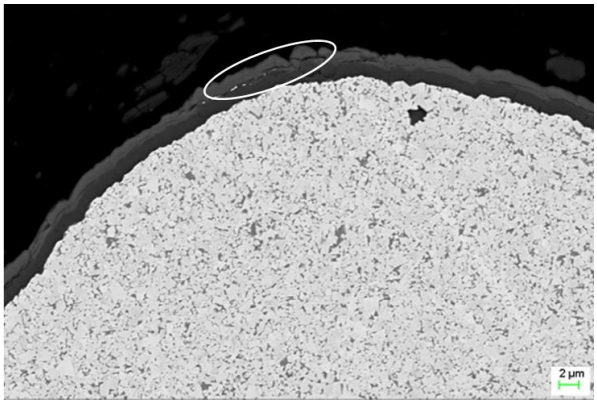
The GIXRD results from Figure 4.34 showed no formation of oxide phases in all the ion implantation dosages except for cutting tools implanted at 2E+16 ions/cm^2 at both acceleration voltages (100 and 120 keV), which showed a formation of MoRu alloy after machining. The x-ray diffraction pattern of the cutting tool inserts were more amorphous after machining compared to before machining. This was a result of the coating slowly detaching from the substrate and coating layers detaching from each other as shown by the micrographs in Figure 5.1. The encircled area shows the detaching of the coating of the inserts at different ion implantation dosages. The EDS results on the wear scars showed the presence of O but no oxidation phase was observed due to the thickness of the oxide layer



(a)



(b)



(c)



(d)

(e)

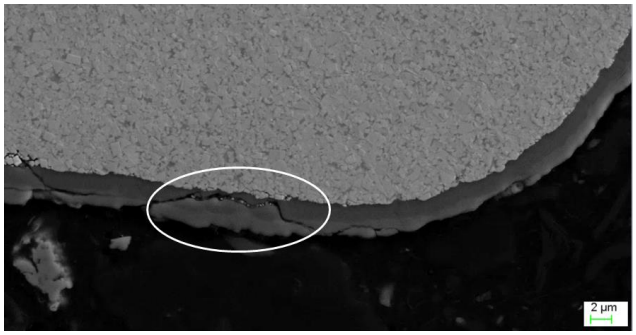


Figure 5.1: FESEM micrographs of the cross-section of the used coated cutting tool inserts (a) non-implanted, (b) 5E+15 , (c) 8E+15 (d) 1E+17 and (e) 2E+16 ions/cm^2 at 100 keV.

Figure 4.35 is the semi spiral cutting chips with jagged edges. The cutting chips had various colours such as golden brown, purple and darker blue, the various colours indicated different oxidation states [86, 96, 100, 101]. Literature has shown that about 85% of heat generated during cutting is absorbed by the cutting chips while 10-15% is absorbed by the workpiece and the cutter [96]. Oxidation of the cutting chips is more evidence that heat generated during heating was absorbed by the cutting chips, which resulted in oxidation when exposed to air and an oxide layer formed. The oxidation of the cutting chips occurred as follows [86].

$$2Fe(s) + O_2(g) \rightarrow 2FeO(s) \qquad \text{Equation 5.1}$$

$$4Fe(s) + 3O_2 \rightarrow 2Fe_2O_3 \qquad \text{Equation 5.2}$$

$$3Fe(s) + 2O_2(g) \rightarrow Fe_3O_4(s) \qquad \text{Equation 5.3}$$

The degree of oxidation reaction is dependent on time, surface area, mass transfer and temperature [86]. The back surface of the cutting chips was shiny and smooth as a result of the constraint provided by the rake face unlike the free surface, which curled away from the rake face and ended up with shear fronts. The oxide layer formed was too thin to be picked up by the x-ray diffraction as shown in Figure 4.38, although EDS results also shown presence of O, which is at least 4% in the cutting chips as shown from Figure 5.2.

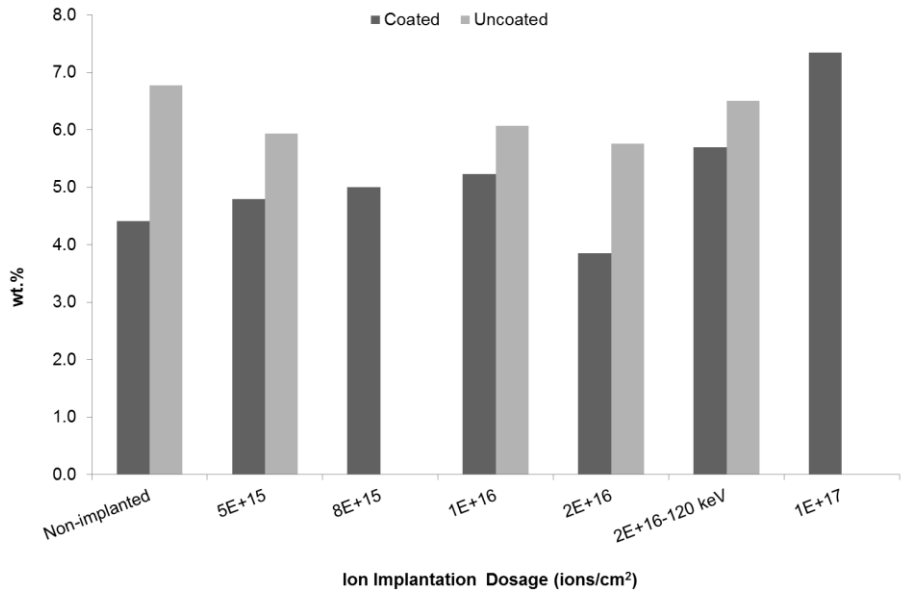


Figure 5.2: Oxygen wt.% in cutting chips.

Microscopic analyses of the cutting chips free surface in Figure 4.39 shown by the FE-SEM micrographs, shows adiabatic shear bands and serrated edges which indicates the difficulty of machining and that the heat rate and the cooling rate were not the same, due to cutting chips with low thermal properties [30, 102]. A lamellar structure characterised by the jagged and rough surfaces is a result of shearing mechanisms [102]. The lamellar structure is thicker than the shear bands which are formed along the width of the cutting chips and perpendicular to their direction. The thicker lamella is an indication of high speeds, high deformation of material and saw-tooth formation which is characterised by the serrated edges [61, 86]. A similar mechanism was observed in all the ion implantation dosages. The chip compression ratio (CCR) was less than, ideally the CCR must be as close to 1 as possible. The CCR at all ion implantation dosages including the non-implanted cutting tool insert were higher or rather close to 1 which indicated a large shear plane angle [32, 95], i.e. a high shear plane angle indicates thin high-velocity chips. The cutting chip thickness variation was due to load variation [86].

The cutting chips morphology further explains why the advantages of unlubricated cutting conditions were not fully realised as the cutting forces remained higher although the workpiece remained relatively warm. Since most of generated heat was absorbed by the cutting chips and the workpiece having low thermal properties as

shown by the shear bands formation, it explains the higher cutting forces and even micro-hardness was increased.

The workpiece surface roughness generated while using the ion-implanted cutting tool was similar to that of non-implanted cutting tool inserts except for the dosage of 2E+16 ions/cm^2 which was higher as shown in Figure 4.41, but it was within acceptable tolerances. The evidence of generated heat absorbed by the cutting chips is shown by the absence of phase or microstructural change as shown in Figure 4.42. The XRD pattern analysis and FE-SEM micrographs in Figure 4.43 show the carbides on the grain boundaries of the ferrite phase.

5.2.2 Effect of increased acceleration voltage during ion implantation

The failure mechanism of the cutting inserts implanted at 2E+16 ions/cm^2 at 120 keV shown in Figure F.0.6 showed coating delamination with cutting chips adhesion (a) and (b) and cutting edge chipping (c and d), similar to the cutting tool inserts implanted with 100 keV at the same ion implantation dosage. However, a 14% and 17% decrease in induced forces and heat generated respectively was achieved while using cutting inserts with high acceleration voltage. This showed that the cutting edge chipping and adherence of cutting chips happened at a later stage of the cutting time. This occurred even though the insert implanted at 120 keV had lower Vickers micro-hardness compared to the insert ion implanted at 100 keV. This could be due to the acceleration voltage which increased the depth of the modified surface [46, 48, 51, 99, 103]. The effect of increased depth of the modified surface was shown by the% decrease residual stresses after machining which was 12%, while the cutting tool inserts ion implanted at 100 keV had a 68% decrease. The benefits of acceleration voltage were further shown by the width of the wear scar as a decrease of 12% was achieved.

5.2.3 Comparison between coated and uncoated cutting tool inserts

The micro-hardness increase after ion implantation on the uncoated inserts was almost similar to that of the coated inserts as discussed in Section 5.1.1. Machining tests were

then conducted using uncoated inserts. Since high cutting speeds were employed, it is known that built–up-edge (BUE) formation is more pronounced at low cutting speeds, as the low cutting speeds triggers pressure that favours weldability of the cutting chips onto the cutting tool insert [6, 96].

The non-implanted uncoated inserts failed in less than 5 minutes after cutting a volume of 1.35E-5 $m^3$of steel which was 90% (1.35E-4 m^3) less than the volume of material machined by the coated inserts. This amount of material was then used as a benchmark for the machining tests on uncoated ion implanted inserts at all ion implantation dosages. Although the uncoated cutting tool inserts both non-implanted and ion implanted machined 90% less material compared to the coated cutting tool inserts they still experienced more damaged compare to the coated (both implanted and non-implanted) inserts as shown in Figure 4.30 and Figure 4.32. Although a crater was observed on the rake face of the uncoated inserts (Figure F.0.8 to Figure F.0.12) based on the equipment available for this research, it was not possible to accurately measure crater depth.

The adhesion of the cutting chips or swarf on the cutting tool inserts resulted in diffusion wear. Diffusion wear occurred due to the fact that diffusion wear is known to increase with increasing cutting speeds [6] and these tests were conducted at fairly high speeds of 180 m/min. Effect of diffusion wear is shown by the crater wear as shown in Figure F.0.8 to Figure F.0.12. Oxidation of the cutting tool was observed since W tend to oxidise at temperatures above 300 °C and that resulted in cracking of the cutting tool on the rake face at impact. Application of uncoated ion implanted cutting inserts is still a no-go for machining of tool steel especially under dry/ unlubricated machining conditions. Tests can be considered when using tool-grade under flooding conditions to ensure that the cutting chips or swarf is washed away from the cutting tool inserts.

The forces induced during machining for the uncoated ion implanted cutting tool inserts were relatively high compared to those of coated ion implanted cutting tool inserts as shown in Figure 4.26. The induced forces were at least 4% higher, however the induced forces experienced by the uncoated insert at ion implantation dosage of 2E+16 ions/cm^2 were 9% lower than those of coated cutting tool inserts at the same dosage. The severe cutting edge chipping increased the shear area during cutting

which subsequently increasing the induced cutting forces. The increase in shear area resulted in increased estimated heat generation during cutting as shown in Figure 4.27. However, the estimated cutting temperature of uncoated cutting tool inserts at the ion implantation dosages of 2E+16-100 keV and 2E+16-120 keV ions/cm^2 at 120 keV was 20 and 42% lower than that of the coated cutting tool insert ion implanted respectively at the same dosage. This was because the cutting edge chipping was not as severe as that of the coated insert at the same ion implantation dosages as shown in Figure F.0.6 and Figure F.0.12. Most of the heat generated during machining was absorbed by the cutting chips as shown by the discontinuous purple and blue cutting chips in Figure 4.36.

Chapter 6 Conclusions

The main aim of this research study was to increase the cutting tool life of coated WC-6wt%Co straight grade inserts by reducing the wear experienced by the cutting tool inserts during face milling of H13 steel. This aim was achieved by successfully implanting various dosages of Ru and Mo ions simultaneously into the cutting tool inserts. A summary of the major results is listed as in Table 6.1 where the ion implantation was done at an acceleration voltage of 100 keV except for a single dosage implanted at 120 keV as indicated. The values in the table represent the percentage increase or decrease of the material property in reference to the non-implanted insert.

Table 6.1: Summary of the major results at different ion implantation dosages.

Implantation dosage (ions/cm$^{2)}$	**5E+15**	**8E+15**	**1E+16**	**2E+16**	**1E+17**	**2E+16 at 120 keV**
Micro-hardness (HV_{50g})	9↑	24↑	14↑	17↑	25↑	12↑
Compressive residual stresses (before machining) (MPa)	5↑	5↑	6↑	40↑	8↓	25↓
Cutting forces (N)	14↑	3↑	4↑	12↑	1↑	2↑
Cutting temperature (°C)	1↑	37↓	4↓	22↑	7↑	1↑
Flank wear (mm)	61↓	66↓	50↓	40↓	58↓	26↓
Ra- workpiece (µm)	13↑	5↑	9↑	61↑	5↑	6↑

From the table the general conclusions that can be drawn are as follows:

Ion implantation improved the tool life of the cutting tool inserts as shown by the decrease in the flank wear achieved at all ion implantation dosages. This was achieved through the synergy between the increased micro-hardness, induced molybdenum oxides and increased compressive stresses. Although the surface roughness of the H13 steel workpiece increased, it remained within acceptable commercial tolerances for all dosages. The surface roughness increase was due to adhesion and chipping of the

cutting edge. The chipping and flaking of the inserts also resulted in an increase in induced forces and estimated heat generated at tool-workpiece interface. The optimum ion implantation dosages of the coated inserts were 8E+15, 1E+17 and 2E+16-120 keV as these had smaller flank wear, lower induced forces and surface roughness of the workpiece compared to the other implanted inserts.

Ion implantation did not change the microstructure of the coated inserts, as they were similar to those of the non-implanted inserts. This was due to the depth of penetration by the implanted ions and how the ions interacted with target lattice structure. The same was observed with the microstructure of the inserts where no microstructural change was observed.

The coated ion implanted inserts performed exceptionally well compared to the uncoated implanted inserts. The coated ion implanted inserts machined 90% more material compared to the uncoated ion implanted inserts and yet the failure of the uncoated ion implanted was excessive. This resulted in an increase of at least 4% in induced cutting forces compared to those of the uncoated ion implanted inserts except for the insert with ion implantation of 2E+16 ions/cm^2. This was due to less chipping of the cutting edge extending to the flank face compared to that of the ion implanted inserts. An increase of at least 4% in estimated heat generated of the ion implanted uncoated inserts compared to those of the ion implanted coated inserts was observed except for the uncoated inserts with ion implantation dosage of 2E+16-100 keV and 2E+16-120 keV as a decrease of 20 and 40% respectively in estimated generated heat was observed. This observed because of lack adhesion at those dosages.

Chapter 7 Recommendations

To achieve better results, it is worth looking into

- Increasing the acceleration voltage during ion implantation as inserts ion implanted using acceleration voltage of 120 keV showed less chipping of the cutting edge extending to the rake face compare to the rest of the insert.
- Using ion implantation dosages higher than 1E+17 ions/cm^2 as it also showed better machining performance compared to the rest of the ion implanted inserts.
- Use flooding or lubricated (MQL) conditions instead of dry conditions to minimise adhesion of the cutting chips on the rake face.

Chapter 8 References

1. Kagnaya, T., Boher, C., Lambert, L., Lazard, M., Cutard, T.: *Wear mechanisms of WC–Co cutting tools from high-speed tribological tests*. Wear. 267, 890–897 (2009).
2. Vogiatzis, S., Papageorgiou, V., Strakov, H., Auger, M.: *CVD TiAlN technology – Coating properties and applications*. Proceedings of 19th Plansee Seminar, 47, Reutte, Austria, (2017).
3. Abdel-Aal, H.A., Nouari, M., Mansori, M.E.: *The effect of thermal property degradation on wear of WC-CO inserts in dry cutting*. Wear. 265, 1670–1679 (2008).
4. Shetty, D.K., Wright, I.G., Mincer, P.N., Clauer, A.H.: *Indentation fracture of WC-Co cermets*. J. Mater. Sci. 20, 1873–1882 (1985).
5. Sacks, N.: *The wear and corrosive-wear response of tungsten carbide-cobalt hardmetals under woodcutting and three body abrasion conditions.* Phd's thesis. University of Erlangen-Nürnberg. (2002).
6. Upadhyaya, G.S.: C*emented tungsten carbides: production, properties, and testing*. Noyes Publications, Westwood, N.J (1998).
7. Marshall, J. M., Kusoffsky, A., *Binder phase structure in fine and coarse WC–Co hard metals with Cr and V carbide additions*. Int. J. Refract. Met. Hard Mater. 40, 27–35 (2013).
8. Weidow, J., Zackrisson, J., Jansson, B., Andrén, H.-O.: *Characterisation of WC-Co with cubic carbide additions*. Int. J. Refract. Met. Hard Mater. 27, 244–248 (2009).
9. Yang, J., Odén, M., Johansson-Jõesaar, M.P., Esteve, J., Llanes, L.: *Mechanical strength of ground WC-Co cemented carbides after coating deposition*. Mater. Sci. Eng. A. 689, 72–77 (2017).
10. Bobzin, K.: *High-performance coatings for cutting tools*. CIRP J. Manuf. Sci. Technol. 18, 1–9 (2017).
11. Deng, B., Tao, Y., Liu, H., Liu, P.: *Influence of niobium ion implantation on the microstructure and tribological properties of TiAlN coatings*. Surf. Coat. Technol. 228, S554–S557 (2013).
12. Gu, J., Barber, G., Tung, S., Gu, R.-J.: *Tool life and wear mechanism of uncoated and coated milling inserts*. Wear. 225–229, 273–284 (1999).
13. Vereschaka, A., Aksenenko, A., Sitnikov, N., Migranov, M., Shevchenko, S., Sotova, C., Batako, A., Andreev, N.: *Effect of adhesion and tribological properties of modified composite nano-structured multi-layer nitride coatings on WC-Co tools life*. Tribol. Int. 128, 313–327 (2018).
14. IshIda, T., ITakura, T.: *Development of Technologies for Recycling Cemented Carbid*e *Scrap and Reducing Tungsten Use in Cemented Carbide Tools*. SEI.Technical Review. 75, 38-46 (2012).
15. Deng, B., Tao, Y., Wang, Y., Liu, P.: *Study of the microstructure and tribological properties of Mo+C implanted TiN coatings on cemented carbide substrates*. Surf. Coat. Technol. 228, S597–S600 (2013).
16. T Tian, B., Yue, W., Fu, Z., Gu, Y., Wang, C., Liu, J.: *Surface properties of Mo-implanted PVD TiN coatings using MEVVA source*. Appl. Surf. Sci. 280, 482–488 (2013).

17. Manory, R.R., Li, C.L., Fountzoulas, C., Demaree, J.D., Hirvonen, J.K., Nowak, R.: *Effect of nitrogen ion-implantation on the tribological properties and hardness of TiN films*. Mater. Sci. Eng., A 253, 319-327 (1998).
18. Liu, B., Deng, B., Tao, Y.: *Influence of niobium ion implantation on the microstructure, mechanical and tribological properties of TiAlN/CrN nano-multilayer coatings*. Surf. Coat. Technol. 240, 405–412 (2014).
19. Treglio, J.R., Tian, A., Perry, A.J.: *Extending carbide tool lifetime by metal ion implantation*. Surf. Coat. Technol. 62, 438–442 (1993).
20. Li, W.L. Fei, W.D., Sun, Y.: Effects of implantation conditions on the roughness. *J. Mater. Sci. Lett.* [21], 239-241, (2002).
21. Deng, B., Tao, Y., Guo, D.: *Effects of vanadium ion implantation on microstructure, mechanical and tribological properties of TiN coating*s. Appl. Surf. Sci. 258, 9080–9086 (2012).
22. Mitsuo, A., Uchida, S., Yamamoto, S., Aizawa, T.: *Improvement of cutting performance for carbide tools via chlorine ion implantation*. Surf. Coat. Technol. 188–189, 630–635 (2004).
23. Zhu, Y.-C., Fujita, K., Iwamoto, N., Nagasaka, H., Kataoka, T.: *Influence of boron ion implantation on the wear resistance of TiAlN coatings*. Surf. Coat. Technol. 158–159, 664–668 (2002).
24. Schramm, B.C., Scheerer, H., Hoche, H., Broszeit, E., Abele, E., Berger, C.: *Tribological properties and dry machining characteristics of PVD-coated carbide inserts.* Surf. Coat. Technol.188-189, 623-629 (2004).
25. Gajrani, K.K., Suresh, S., Sankar, M.R.: *Environmental friendly hard machining performance of uncoated and MoS_2 coated mechanical micro-textured tungsten carbide cutting tools*. Tribol. Int. 125, 141–155 (2018).
26. Lisovskii, A.F.: *Cemented Carbides Alloyed with Ruthenium, Osmium, and Rhenium*. Powder Metall. Met. Ceram. 39, 428–433 (2000).
27. Liu, C.: *Alternative Binder Phases for WC Cemented Carbides*. Master's thesis. KTH Royal Institute of Technology. (2014).
28. Tesfamichael, T., Ahsan, M., Notarianni, M., Groß, A., Hagen, G., Moos, R., Ionescu, M., Bell, J.: *Gas sensing of ruthenium implanted tungsten oxide thin films*. Thin Solid Films. 558, 416–422 (2014).
29. The top producing countries of precious metals, http://www.miningoilgasjobs.com.au/mining/ last visit 25 March 2019 08:15 am.
30. Groover, M.P. *Fundamentals of Modern Manufacturing: Materials, Processes, and System*s. 4th ed. Hoboken: John Wiley & Sons (2010).
31. Luyckx, S., Sacks, N., Love, A.: I*ncreasing the abrasion resistance without decreasing the toughness of WC–Co of a wide range of compositions and grain sizes*. Int. J. Refract. Met. Hard Mater. 25, 57–61 (2007).
32. Trent, E.M., Wright, P.K.: Metal cutting. Butterworth-Heinemann, Boston (2000).
33. Kudou, K., Ono, T., Okada, S.:*Crater wear characteristics of an Fe-diffused carbide cutting tool* . J Mater Process Technol. 132, 255-261 (2003).
34. Uhlmann, E., Dethlefs, I., Faltin, F., Schweitzer, L.: *Cutting and Drilling of Metals and Other Materials: A Comparison. In: Reference Module in Materials Science and Materials Engineering*. Elsevier (2016).
35. Aihua, L., Jianxin, D., Haibing, C., Yangyang, C., Jun, Z.: *Friction and wear properties of TiN, TiAlN, AlTiN and CrAlN PVD nitride coatings*. Int. J. Refract. Met. Hard Mater. 31, 82–88 (2012).

36. Beake, B.D., Ning, L., Gey, C., Veldhuis, S.C., Komarov, A., Weaver, A., Khanna, M., Fox-Rabinovich, G.S.: *Wear performance of different PVD coatings during hard wet end milling of H13 tool steel*. Surf. Coat. Technol. 279, 118–125 (2015).
37. Lu, L., Wang, Q., Chen, B., Ao, Y., Yu, D., Wang, C., Wu, S., Kim, K.H.: *Microstructure and cutting performance of CrTiAlN coating for high-speed dry milling*. Trans. Nonferrous Met. Soc. China. 24, 1800–1806 (2014).
38. Teppernegg, T., Czettl, C., Michotte, C., Mitterer, C.: *Arc evaporated Ti-Al-N/Cr-Al-N multilayer coating systems for cutting applications*. Int. J. Refract. Met. Hard Mater. 72, 83–88 (2018).
39. Strakov, H., Auger, M., Papageorgiou, V., Vogiatzis, S. *Advanced CVD equipment*. Proceedings of 19th Plansee Seminar, 97, Reutte, Austria, (2017).
40. Glatz, S.A., Bolvardi, H., Kolozsvári, S., Koller, C.M., Riedl, H., Mayrhofer, P.H.: *Arc evaporated W-alloyed Ti-Al-N coatings for improved thermal stability, mechanical, and tribological properties*. Surf. Coat. Technol. 332, 275–282 (2017).
41. Czettl, C., Schleinkofer, U., Schedle, F., Wolf, C., Lechleitner, M., Holzschuh, H., Bürgin, W.: CVD TiAlN – *Development and challenges for use in mass production*. Proceedings of 19th Plansee Seminar, 45, Reutte, Austria, (2017).
42. Grossmann, B., Tkadletz, M., Schalk, N., Czettl, C., Pohler, M., Jamnig, A., Mitterer, C.: *Influence of the Ta content on microstructure, properties and thermal stability of arc evaporated Ti1-x-yAlxTayN hard coatings*. Proceedings of 19th Plansee Seminar, 96, Reutte, Austria, (2017).
43. Hörling, A., Hultman, L., Odén, M., Sjölén, J., Karlsson, L.: *Mechanical properties and machining performance of Ti1−xAlxN-coated cutting tools*. Surf. Coat. Technol. 191, 384–392 (2005).
44. Pemmasani, S.P., Valleti, K., Gundakaram, R.C., Rajulapati, K.V., Mantripragada, R., Koppoju, S., Joshi, S.V.: *Effect of microstructure and phase constitution on mechanical properties of Ti1−xAlxN coatings*. Appl. Surf. Sci. 313, 936–946 (2014).
45. Dearnaley, G.: *Ion implantation for improved resistance to wear and corrosion*. Int. J. Mater. Eng. Appl. 1, 28–41 (1978).
46. Townsend, P.D., Chandler, P.J., Zhang, L.: *Optical effects of ion implantation*. Cambridge Univ. Press, Cambridge (1994).
47. Cassuto, Y. *Ion Implantation Studies in Cemented Carbides*, Master's thesis. University of the Witwatersrand. (1987).
48. Mabena, C.M., *A Rutherford backscattering study on radiation damage and the diffusion of krypton implanted into 6H-SiC*. Master's thesis. University of Pretoria. (2014).
49. Perry, A.J., Treglio, J.R., Valvoda, V., Rafaja, D.: *Residual stress in metal ion implanted titanium nitride films studied by glancing incidence x-ray diffraction*. J. Vac. Sci. Technol. Vac. Surf. Films. 13, 1067–1072 (1995).
50. Rafaja, D., Valvoda, V., Perry, A.J., Treglio, J.R.: *Depth profile of residual stress in metal-ion implanted TiN coatings*. Surf. Coat. Technol. 92, 135–141 (1997).
51. Manory, R.R., Mollica, S., Ward, L., Purushotham, K.P., Evans, P., Noorman, J., Perry, A.J.: *The effects of MEVVA ion implantation on the tribological properties of PVD-TiN films deposited on steel substrates*. Surf. Coat. Technol. 155, 136–140 (2002).

52. Ward, L.P., Purushotham, K.P., Manory, R.R.: *Studies on the surface modification of TiN coatings using MEVVA ion implantation with selected metallic species*. Nucl. Instrum. Methods Phys. Res. Sect. B Beam Interact. Mater. At. 368, 37–44 (2016).
53. Poletika, M.F., Vesnovsky, O.K., Polestchenko, K.N.: I*on implantation for cutting tools*. Nucl. Instrum. Methods Phys. Res. Sect. B Beam Interact. Mater. At. 61, 446–450 (1991).
54. Vesnovsky, O.K.: *Ion implantation of cutting tools*. Surf. Coat. Technol. 52, 297–299 (1992).
55. Treglio, J.R.: *High dose metal ion implantation*. Nucl. Instrum. Methods Phys. Res. Sect. B Beam Interact. Mater. At. 40–41, 567–570 (1989).
56. Popovic, M., Novakovic, M., Bibic, N. *Annealing effects on the properties of TiN thin films*. Process. Appl. Ceram.9 2, 67-71 (2015).
57. Chubb, J.P., Billingham, J. *Coated cutting tools - A study of wear mechanisms in high speed machining* . Wear. 61, 283-293 (1980).
58. Dearnley, P.A.: *Rake and Flank Wear Mechanisms of Coated Cemented Carbides*. Surf. Eng. 1, 43–58 (1985).
59. Wang, C.Y., Xie, Y.X., Qin, Z., Lin, H.S., Yuan, Y.H., Wang, Q.M.: *Wear and breakage of TiAlN- and TiSiN-coated carbide tools during high-speed milling of hardened steel*. Wear. 336–337, 29–42 (2015).
60. König, U., Wolf, G.K.: *Effects of ion implantation in cemented carbides and cobalt alloys*. Surf. Coat. Technol. 33, 501–509 (1987).
61. ASM Handbook, Vol 16 - Machining Processes.
62. Geoffrey Boothroyd, W.A.K.: *Fundamentals of Machining and Machine Tools*. CRC Press, Taylor & Francis Group, 270 Madison Avenue, New York, NY 10016 (2006).
63. Kurlov, A.S., Gusev, A.I.: H*ardmetals WC–Co Based on Nanocrystalline Powders of Tungsten Carbide WC. In: Tungsten Carbides*. pp. 191–237. Springer International Publishing, Cham (2013).
64. Stocker, W.M., Hicks, T.: *Metalcutting: Today's techniques for engineers and shop personnel*. 1st ed. New York, McGraw-Hill, (1979).
65. www.slideshare.net/palanivendhan/metal-cutting. last visit 03 March 2019 08:48 am.
66. Tian, X., Zhao, J., Zhao, J., Gong, Z., Dong, Y.: *Effect of cutting speed on cutting forces and wear mechanisms in high-speed face milling of Inconel 718 with Sialon ceramic tools*. Int. J. Adv. Manuf. Technol. 69, 2669–2678 (2013).
67. Astakhov, V.P.: *Effects of the cutting feed, depth of cut, and workpiece (bore) diameter on the tool wear rate*. Int. J. Adv. Manuf. Technol. 34, 631–640 (2006).
68. Mechanics of metal cutting, https://www.slideshare.net/ last visit 27 February 2019 2:09 pm.
69. www.slideshare.net/manoj18biet/mechanics-of-metal-cutting. last visit 03 March 2019 09:54 pm.
70. Melo, A.C.A. de, Milan, J.C.G., Silva, M.B. da, Machado, Á.R.: *Some observations on wear and damages in cemented carbide tools*. J. Braz. Soc. Mech. Sci. Eng. 28, 269–277 (2006).
71. Larsen-Basse, J.: *Effect of Composition, Microstructure, and Service Conditions on the Wear of Cemented Carbides*. JOM. 35, 35–42 (2013).

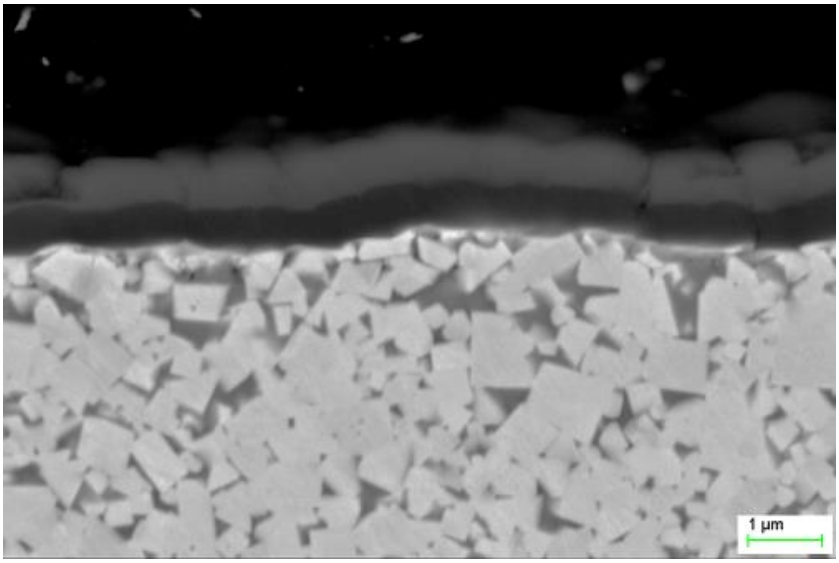
72. Farid, A. A., Sharif, S., Ashrafi, S. Idris, M. H.: *Statistical analysis, modeling, and optimization of thrust force and surface roughness in high-speed drilling of Al-Si alloy*. Proc. Inst. Mech. Eng. B J Eng. Manuf. 227 (6), 808-820 (2013).
73. Hard Prep, https://www.ctemag.com/news/articles/hard-prep last visit 18 March 2019 01:00 pm.
74. International Organisation of Standards. ISO 8688-1:1989. *Tool life testing in milling- Part 1: Face milling*. Switzerland: International Organisation of Standards (1989).
75. Genga, R.M.: *Microstructure and properties of selected WC-cemented carbides manufactured by SPS method*. Phd's thesis. University of the Witwatersrand. (2014).
76. Jawaid, A., Koksal, S. and Sharif, S. *Cutting performance and wear characteristics of PVD coated and uncoated carbide tools in face milling Inconel 718 aerospace alloy*. J. Mater. Process. Technol. 116, 2–9 (2001).
77. Sean J. Bailey, N.C.B.: Annual Book of ASTM Standards, Non Ferrous Metal Products. ASTM International, United States of America (2010).
78. Roebuck, B, Gee, M, Bennett, E.G. and Morrel, l. R. *Mechanical Tests for Hardmetals*. Measurement good practice guide no.20, Crown, UK (1999).
79. Gerard, D.A., Koss, D.A.: *The influence of porosity on short fatigue crack growth at large strain amplitudes*. Int. J. Fatigue. 13, 345–352 (1991).
80. International Organisation of Standards. ISO 3878: 1983. *Hardmetals - Vickers hardness test*. Switzerland: International Organisation of Standards (1983).
81. International Organisation of Standards. ISO 28079:2009. *Hardmetals - Palmqvist toughness test*. Switzerland: International Organisation of Standards (2009).
82. Ait-Djafer, A.Z., Saoula, N., Aknouche, H., Guedouar, B., Madaoui, N.: *Deposition and characterization of titanium aluminum nitride coatings prepared by RF magnetron sputtering*. Appl. Surf. Sci. 350, 6–9 (2015).
83. Yoon, S.-Y., Lee, K.O., Kang, S.S., Kim, K.H.: *Comparison for mechanical properties between TiN and TiAlN coating layers by AIP technique*. J. Mater. Process. Technol. 130–131, 260–265 (2002).
84. Wei, Y., Li, C., Gong, C., Tian, X., Yang, S.: *Microstructure and mechanical properties of TiN/TiAlN multilayer coatings deposited by arc ion plating with separate targets*. Trans. Nonferrous Met. Soc. China. 21, 1068–1073 (2011).
85. Bouzakis, D., Mirisidis, I., Hadjiyiannis, S., Skordaris, G., Michailidis, N., Erkens, G., Cremer, R.: *Improved Coating Properties and Optimized Substrate Data, Essential Conditions for High Performance Cutting Tools*. Tribol. Ind. 25, 1-17 (2003).
86. Zhang, S., Guo, .B.A*n experimental and analytical analysis on chip morphology, phase transformation, oxidation, and their relationships in finish hard milling*. Int. J. Mach. tool. Manu. 49, 805–813 (2009).
87. Fujii, T., Moynier, F., Telouk, P., Albarede, F.: *Mass-Independent Isotope Fractionation of Molybdenum and Ruthenium and the Origin of Isotopic Anomalies in Murchison* The Astrophysical Journal. 674, 1506-1516 (2006).
88. Bai, M., Zhao, Y., Jiao, B., Zhu, L., Zhang, G., Wang, L.: *Research on ion implantation in MEMS device fabrication by theory, simulation and experiments*. Int. J. Mod. Phys. B. 32, 1850170 (2018).
89. Kang, T.J., Kim, J.-G., Lee, H.-Y., Lee, J.-S., Lee, J.-H., Hahn, J.-H., Kim, Y.H.: *Modification of optical and mechanical surface properties of sputter-deposited*

aluminum thin films through ion implantation. Int. J. Precis. Eng. Manuf. 15, 889–894 (2014).
90. Gardner, P.R.: *A review of ion implantation applications to engineering materials*. Mater. Des. 8, 210–219 (1987).
91. Courboin, D., Grouillet, A., Andre, E.: *Surface roughness of ion implanted 〈100〉 silicon studied by atomic force microscopy*. Surf. Sci. 342, L1111–L1115 (1995).
92. Powell, C.: *X-ray Photoelectron Spectroscopy Database XPS, Version 4.1, NIST Standard Reference Database 20*, http://srdata.nist.gov/xps/, (1989) last visit 14 March 2019 20:15.
93. Chang, C.-L., Wang, D.-Y.: *Characterization of surface enhancement of carbon ion-implanted TiN coatings by metal vapor vacuum arc ion implantation*. Nucl. Instrum. Methods Phys. Res. Sect. B Beam Interact. Mater. At. 194, 463–468 (2002).
94. Dynamic Periodic Table, //www.ptable.com/ last visit 26 March 2019 10:00 am.
95. Eckowitz, J. *Optimization of the Machining of Ti-6Al-4V under MQL and Flood Cooling Conditio*ns, Master's thesis. University of the Witwatersrand. (2013).
96. Toh, C.K.: *Comparison of chip surface temperature between up and down milling orientations in high speed rough milling of hardened steel*. J. Mater. Process. Technol. 167, 110–118 (2005).
97. Genga, R.M., Akdogan, G., Polese, C., Garrett, J.C., Cornish, L.A.: *Abrasion wear, thermal shock and impact resistance of WC-cemented carbides produced by PECS and LPS*. Int. J. Refract. Met. Hard Mater. 49, 133–142 (2015.
98. Gassner, M., Schalk, N., Tkadletz, M., Pohler, M., Czettl, C., Mitterer, C.: *Influence of cutting speed and workpiece material on the wear mechanisms of CVD TiCN/α-Al_2O_3 coated cutting inserts during turning*. Wear. 398–399, 90–98 (2018).
99. Figueroa, R., Abreu, C.M., Cristo'bal, M.J. Pena, G. *Effect of nitrogen and molybdenum ion implantation in the tribological behavior of AA7075 aluminum alloy*. Wear. 276–277, 53–60 (2012).
100. Ning, Y., Rahman, M., Wong, Y..: *Investigation of chip formation in high speed end milling*. J. Mater. Process. Technol. 113, 360–367 (2001).
101. Chen, X., Zhao, J., Liu, S., Dong, Y., Wang, F.: *Investigation on the chip formation concerning tool inclination angles in ball end milling of H13 die stee*l. Proc. Inst. Mech. Eng. Part B J. Eng. Manuf. 228, 337–355 (2014).
102. Liyao, G., Minjie, W., Chunzheng, D.: *On adiabatic shear localized fracture during serrated chip evolution in high speed machining of hardened AISI 1045 steel*. Int. J. Mech. Sci. 75, 288–298 (2013).
103. Sharkeev, Y.P., Didenko, A.N., Kozlov, E.V.: *High dislocation density structures and hardening produced by high fluency pulsed-ion-beam implantation*. Surf. Coat. Technol. 65, 112–120 (1994).

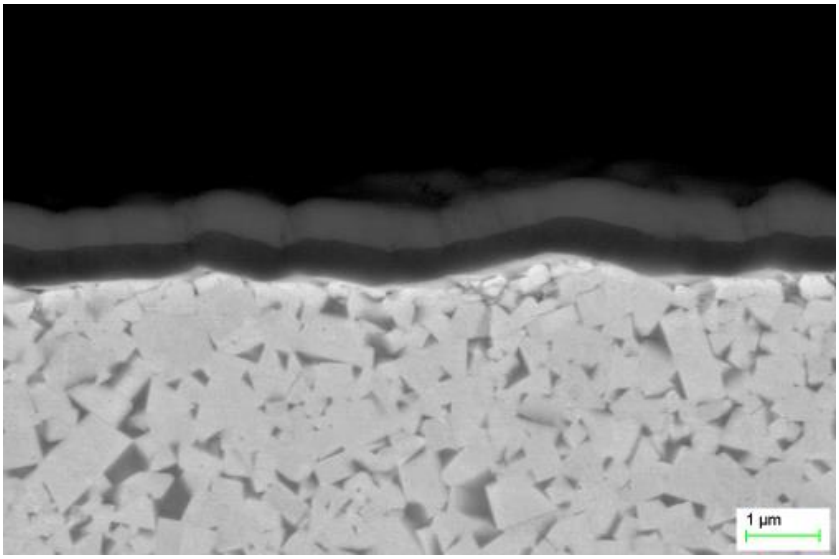
Appendix A

FESEM micrographs of the coated ion implanted cutting tool inserts cross-sections

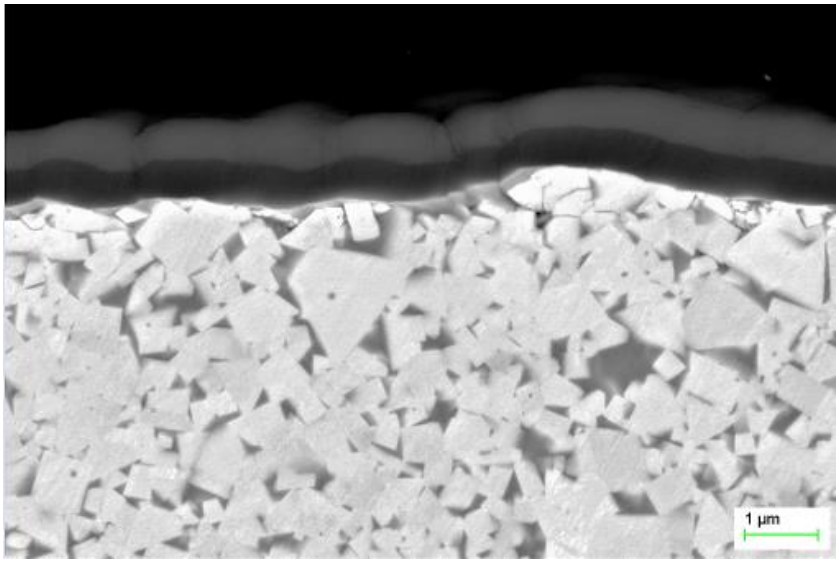
(a)



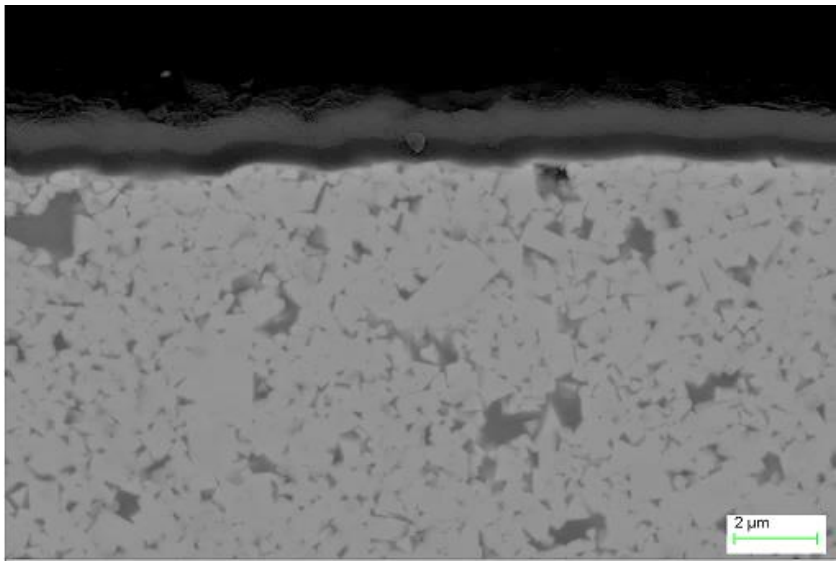
(b)



(c)



(d)



(e)

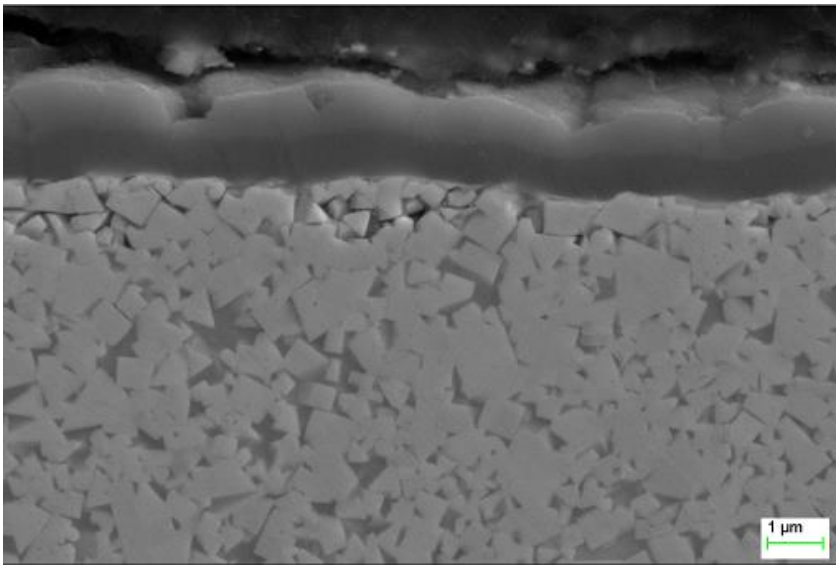
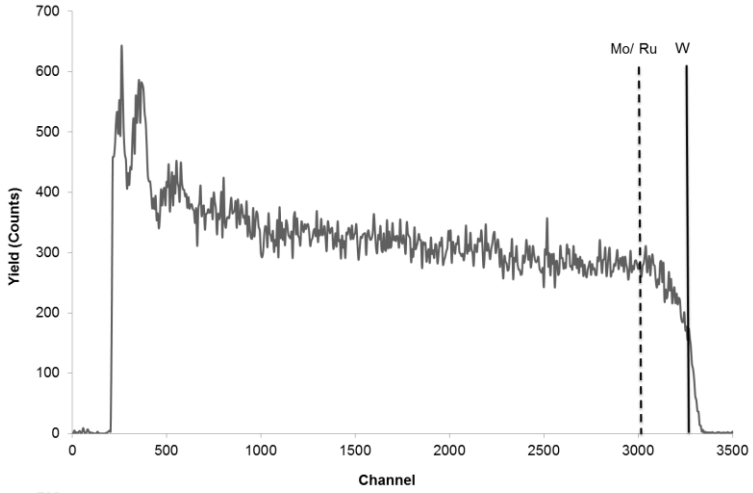


Figure A.0.1: FESEM Micrographs of the ion implanted inserts (a) 5E+15 (b) 8E+15 (c) 1E+16 (d) 2E+16 ions/cm^2 at 100 keV and (e) 2E+16 ions/cm^2 at 120 keV.

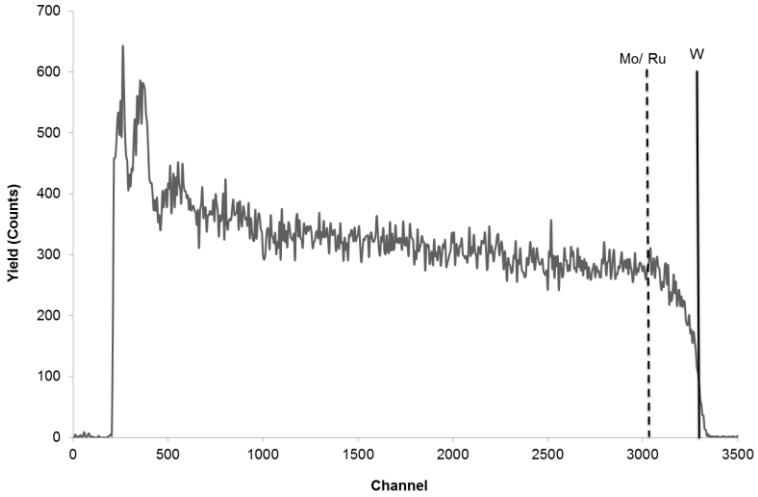
Appendix B

Rutherford Backscattered Spectroscopy (RBS)

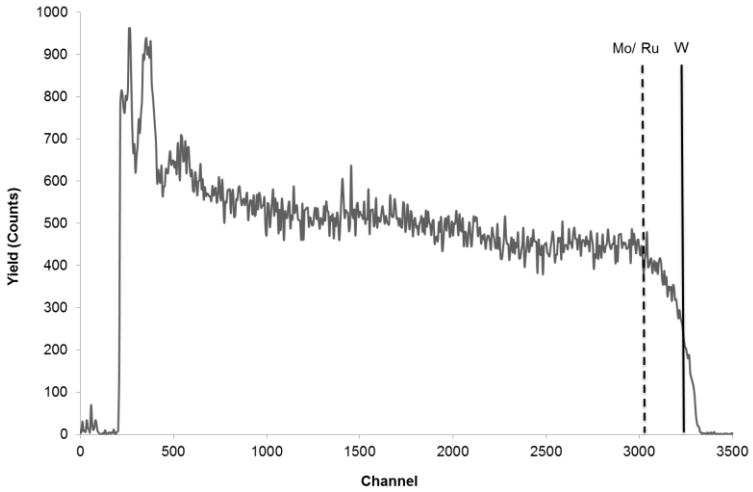
(a)



(b)



(c)



(d)

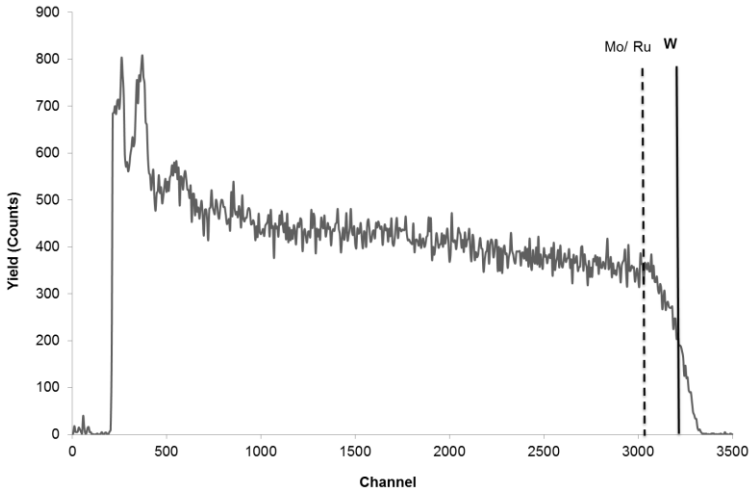
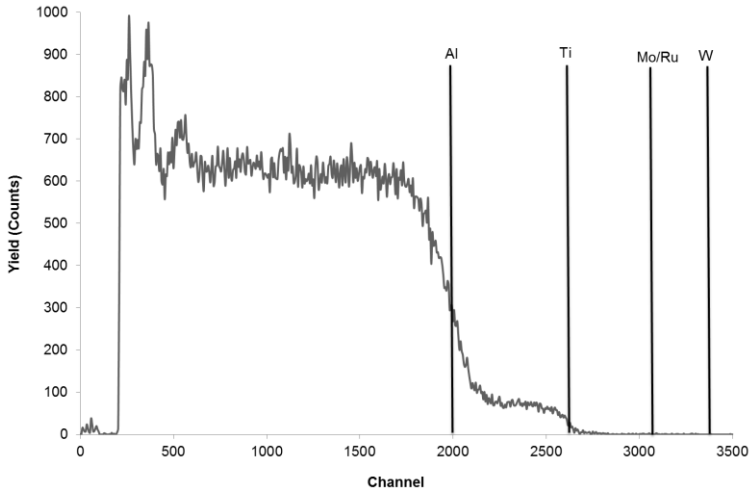
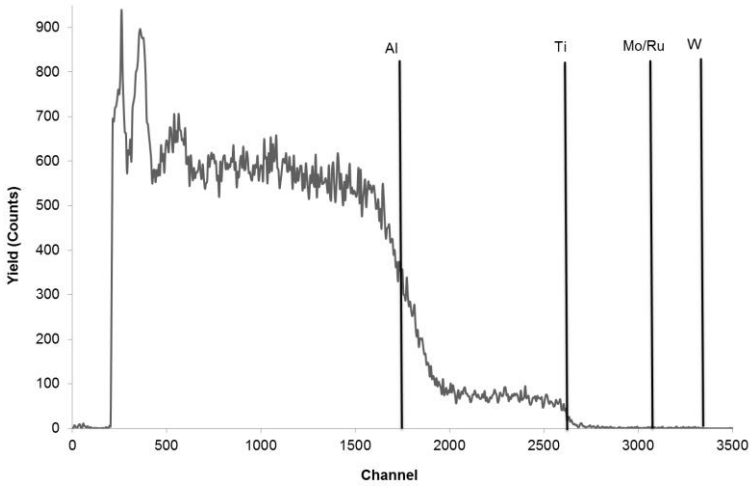


Figure B.0.1: RBS of the uncoated tool inserts implanted (a) 5E+15, (b) 8E+15, (c) 1E+16, and (d) 2E+16 ions/cm^2.

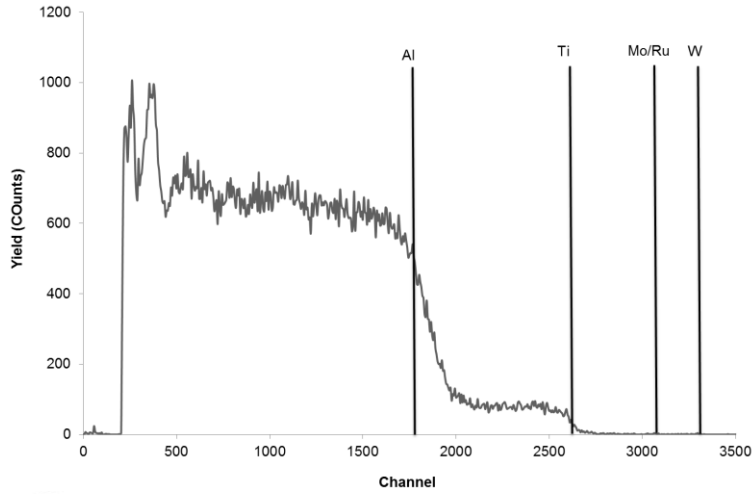
(a)



(b)



(c)



(d)

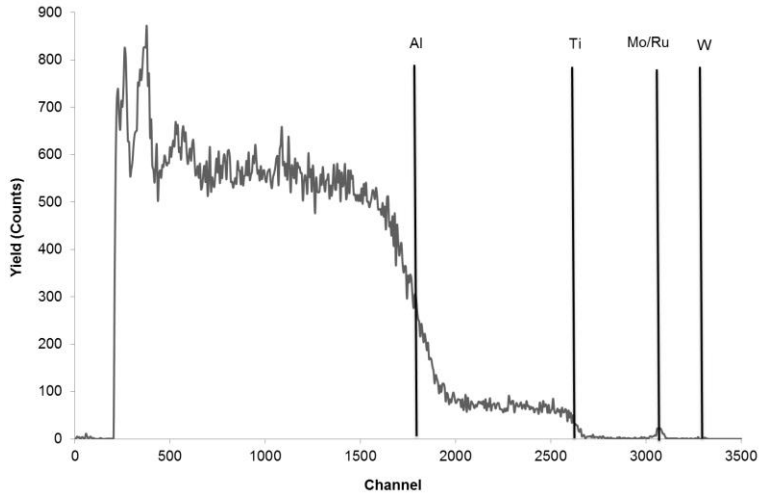
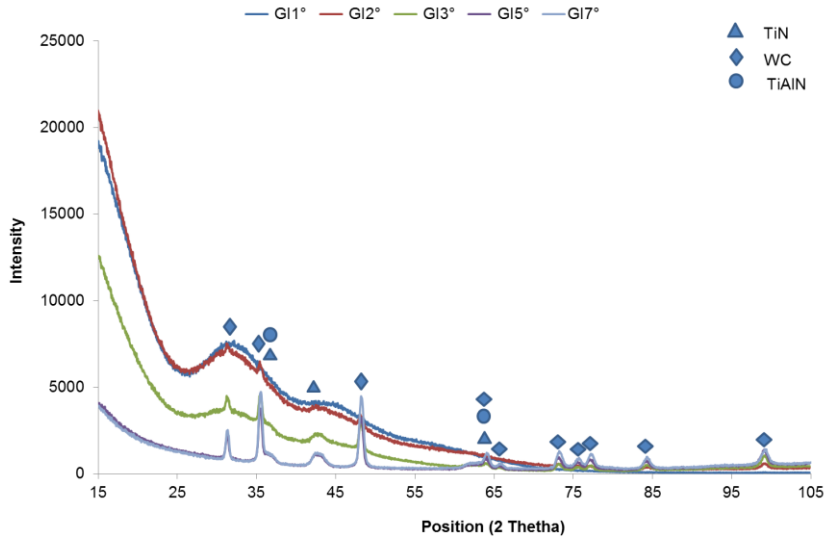


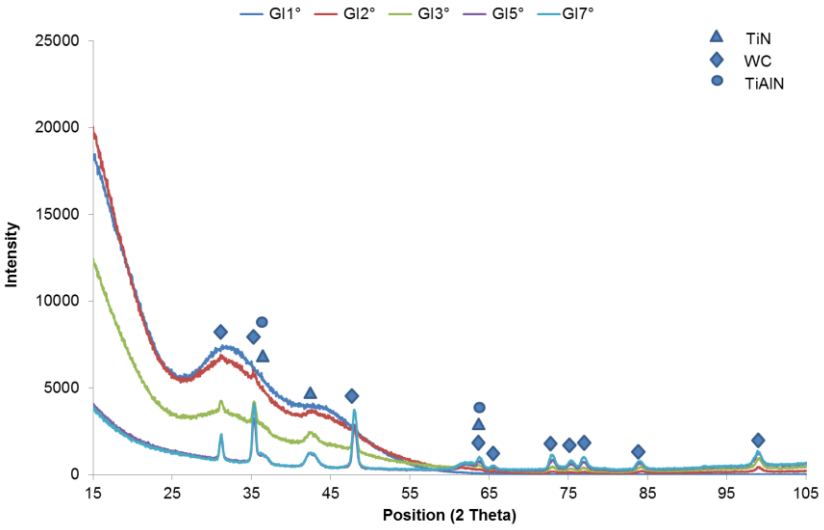
Figure B.0.2: RBS of the coated tool inserts implanted (a) 5E+15, (b) 8E+15, (c) 1E+16, and (d) 1E+17 ions/cm^2.

Appendix C

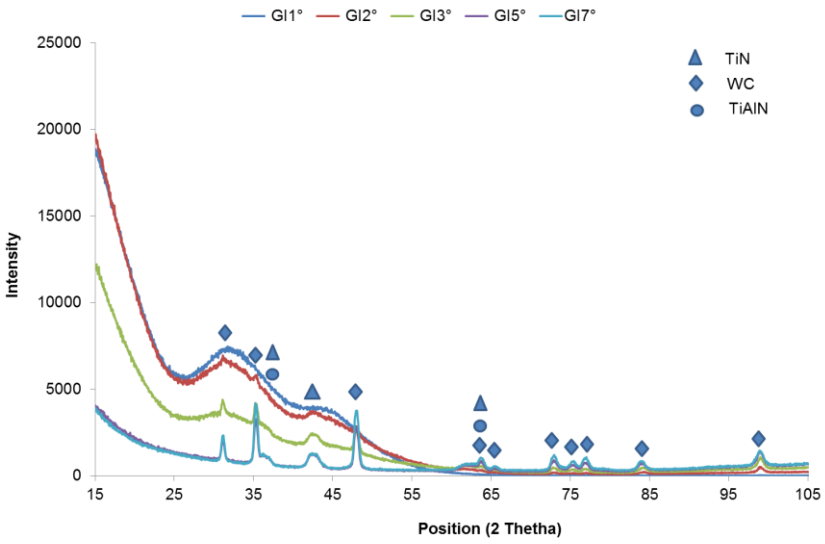
Grazing incident X-ray Diffraction Patterns



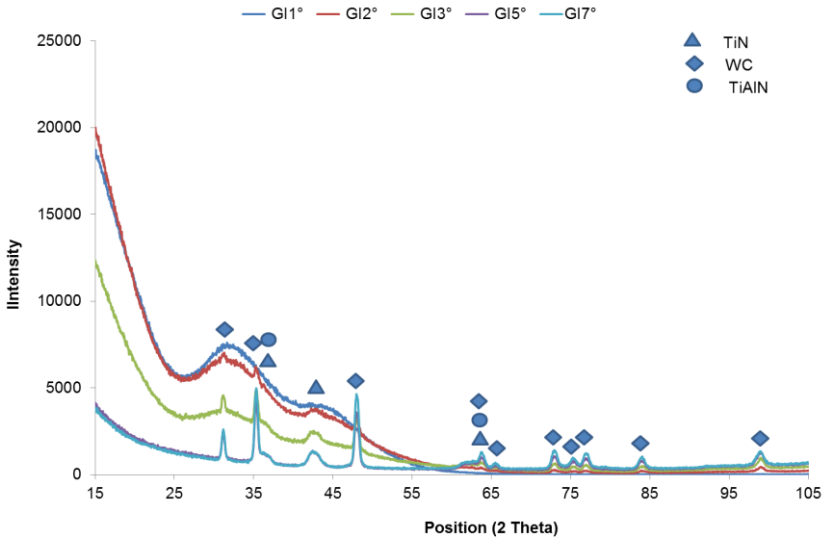
(a)



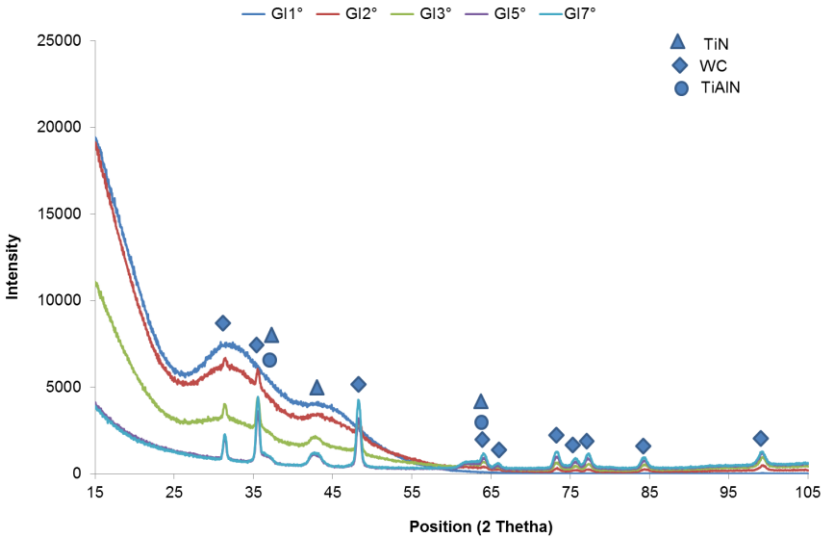
(b)



(c)

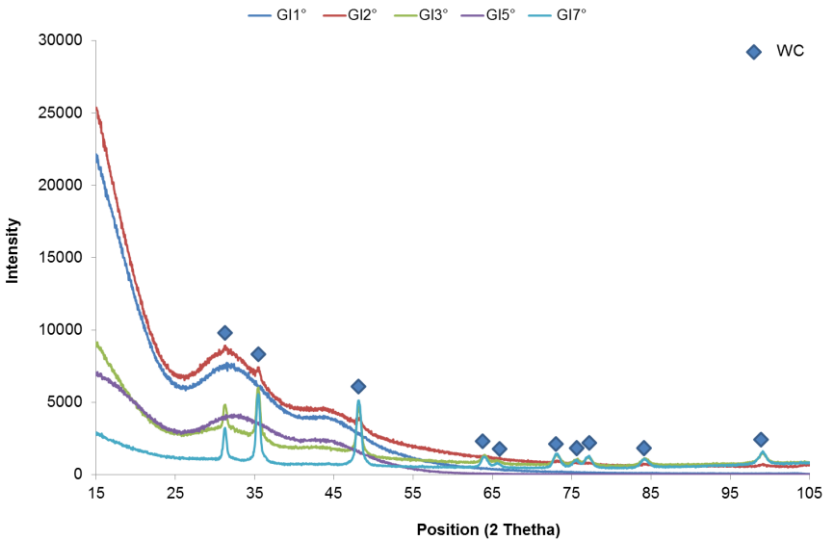


(d)

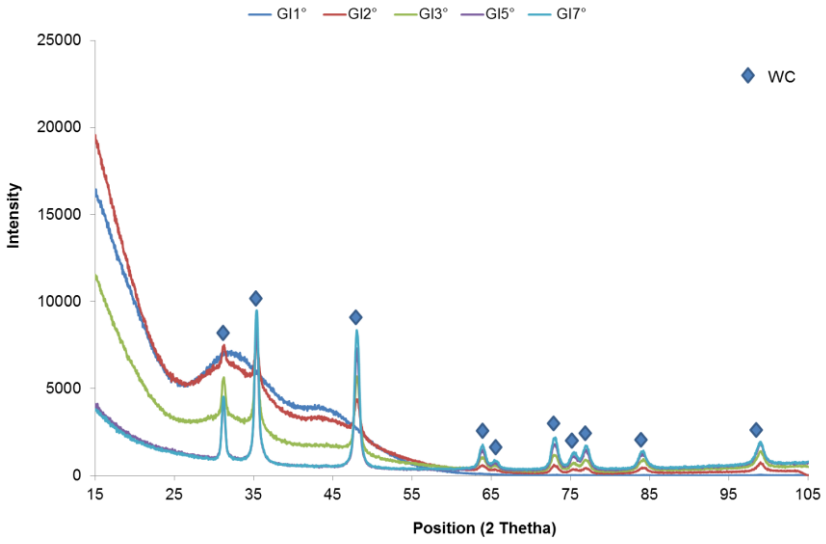


(e)

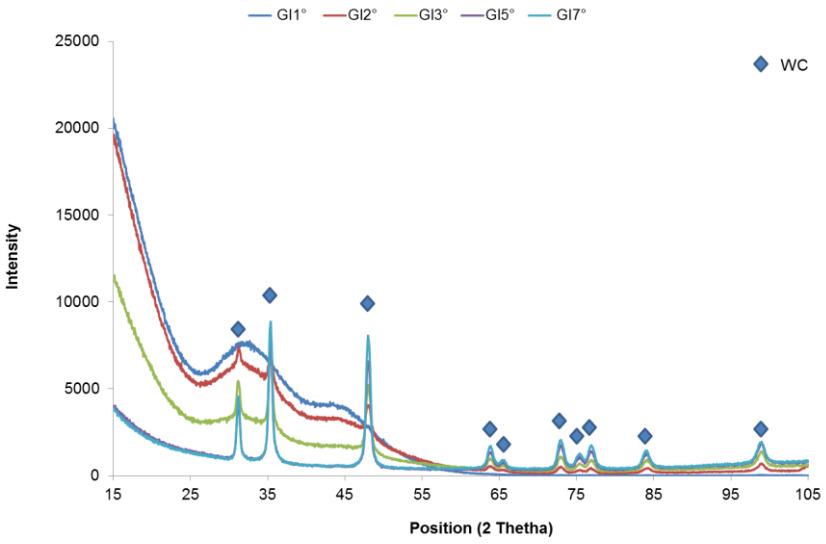
Figure C.0.1 GIXRD results (a) 5E+15, (b) 8E+15, (c) 1E+16, (d) 2E+16-120 keV and (e) 1E+17 ions/cm^2.


GI1°
GI2°
GI3°
GI5°
GI7°
WC
Intensity
Position (2 Thetha)

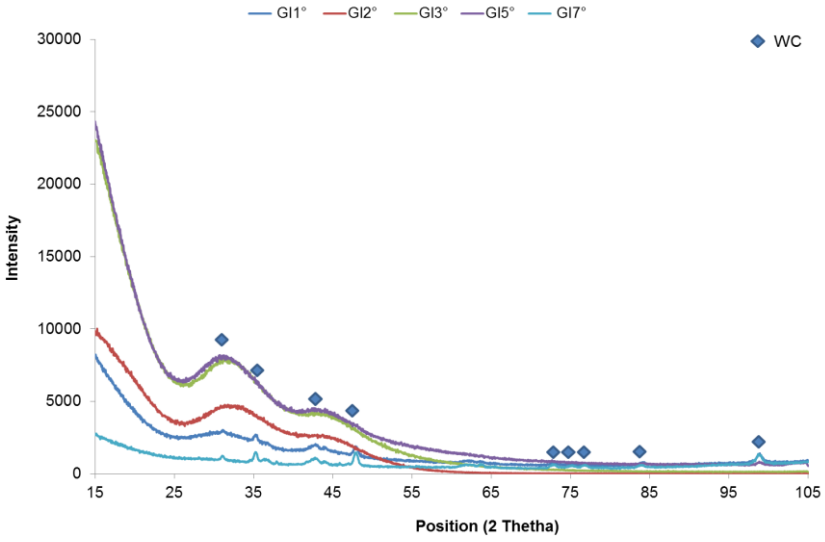
(a)


GI1°
GI2°
GI3°
GI5°
GI7°
WC
Intensity
Position (2 Thetha)

(b)


GI1°
GI2°
GI3°
GI5°
GI7°
WC
Intensity
Position (2 Thetha)

(c)

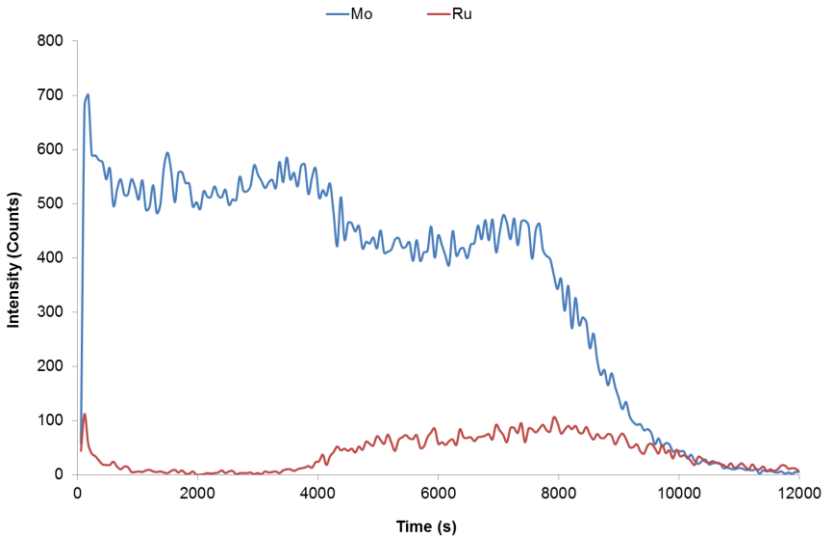


(d)

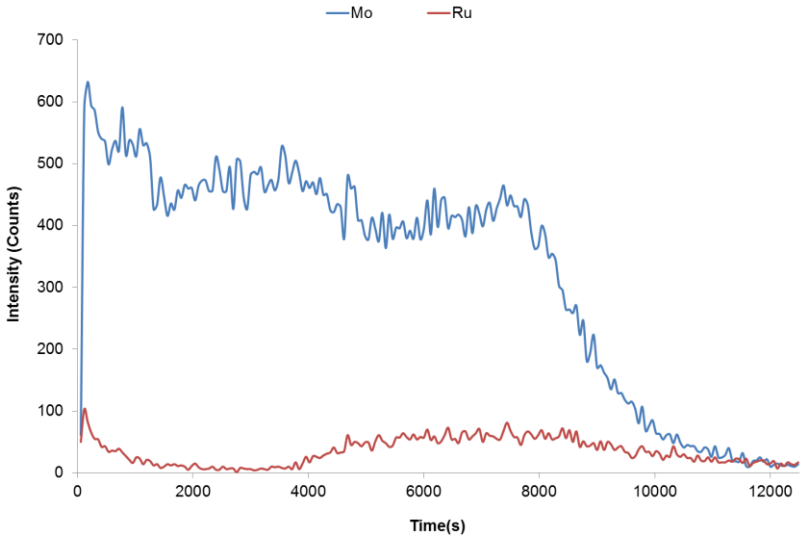
Figure C.0.2: GIXRD results (a) 5E+15, (b) 8E+15, (c) 1E+16 and (d) 2E+16-120 keV.

Appendix D

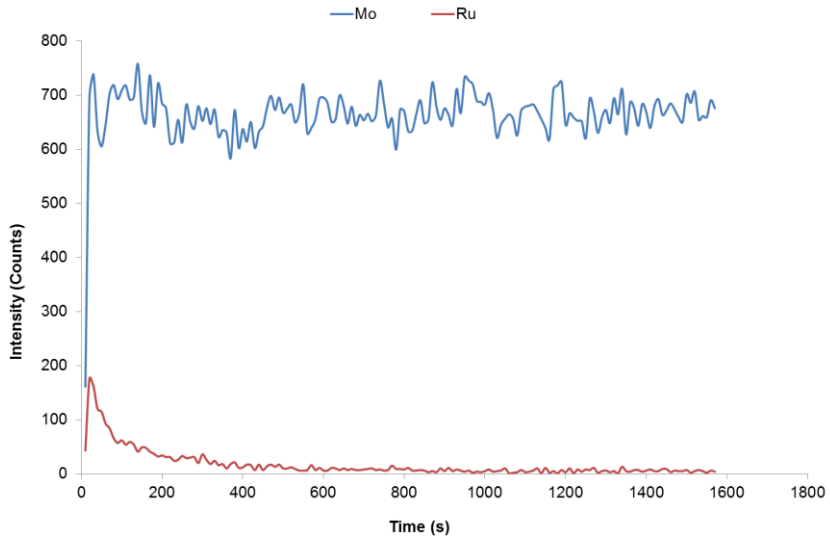
Time-of-Flight Mass Ion Mass Spectroscopy (TOFSIMS)



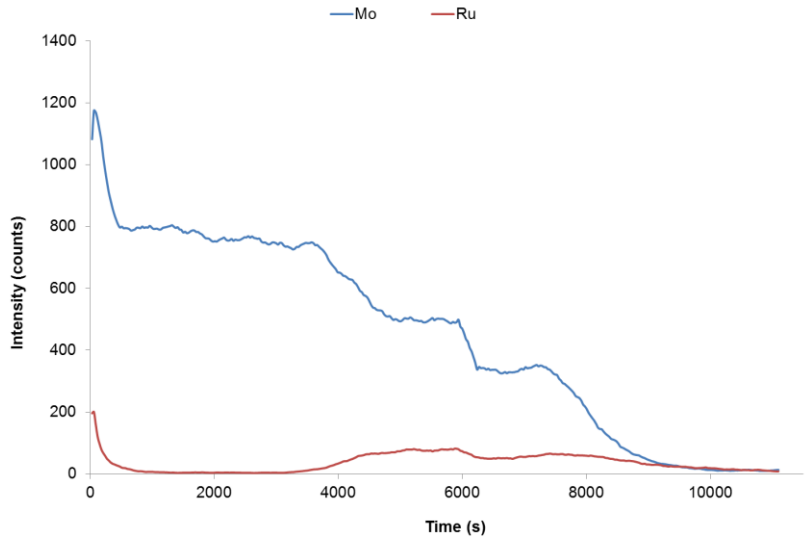
(a)



(b)



(c)



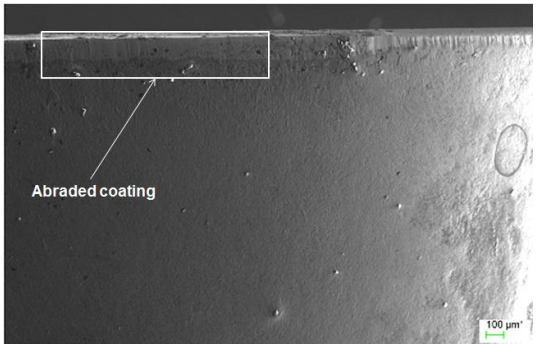
(d)

Figure D.0.1: TOFSIMS results (a) 8E+15, (b) 1E+16, (c) 2E+16-120 keV and (d) 1E+17 ions/cm^2.

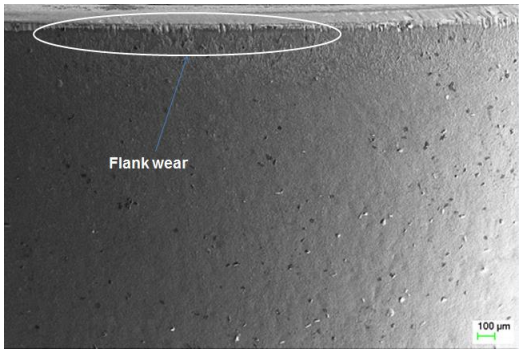
Appendix E

Flank face of the coated inserts

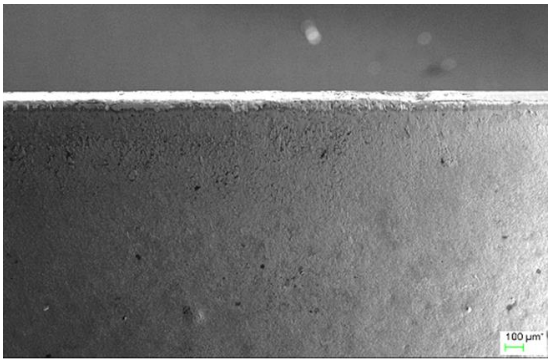
(a)



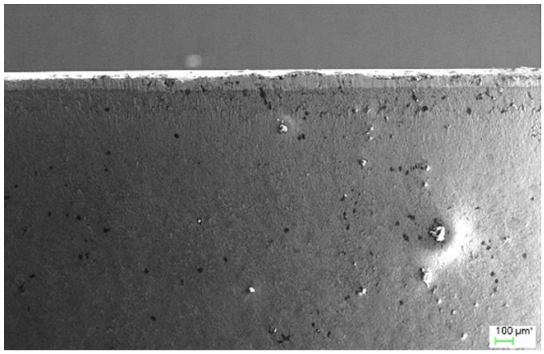
(b)



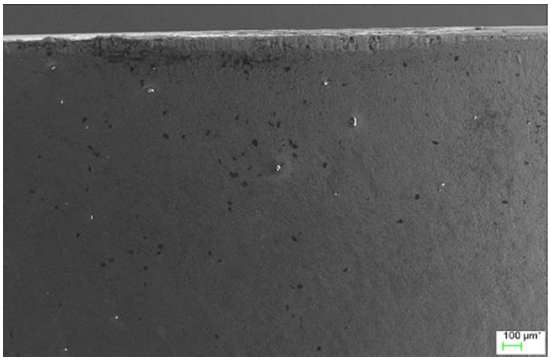
(c)



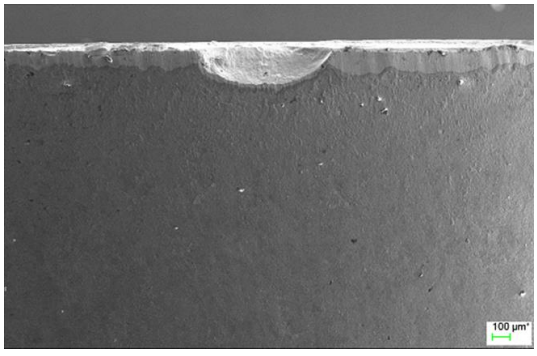
(d)



(e)



(f)



(g)

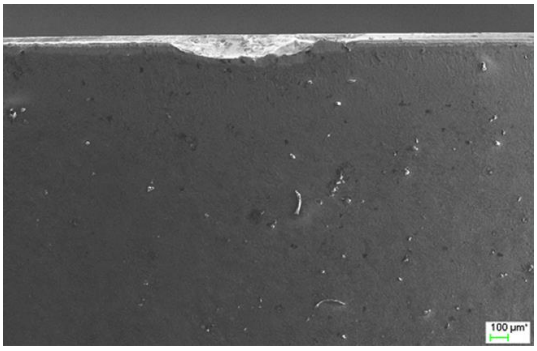
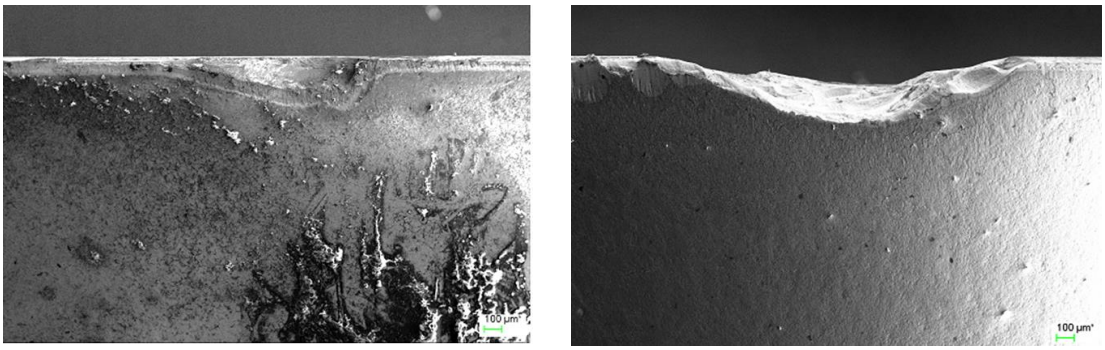


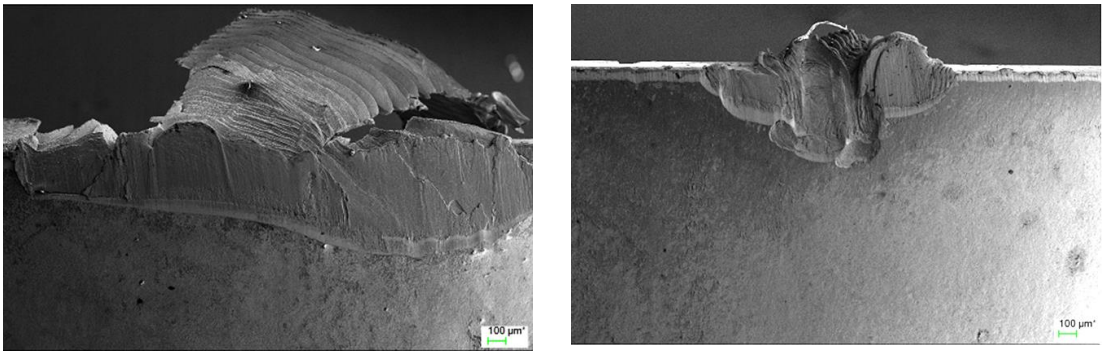
Figure E.0.1: FESEM Micrographs showing flank wear on the coated implanted inserts (a) non-implanted (b) 5E+15 (c) 8E+15 (d) 1E+16 (e) 2E+16, (f) 2E+16-120 keV and (g) 1E+17 ions/cm^2.

Flank face of the uncoated inserts

(a) (b)



(c) (d)



(e) (f)

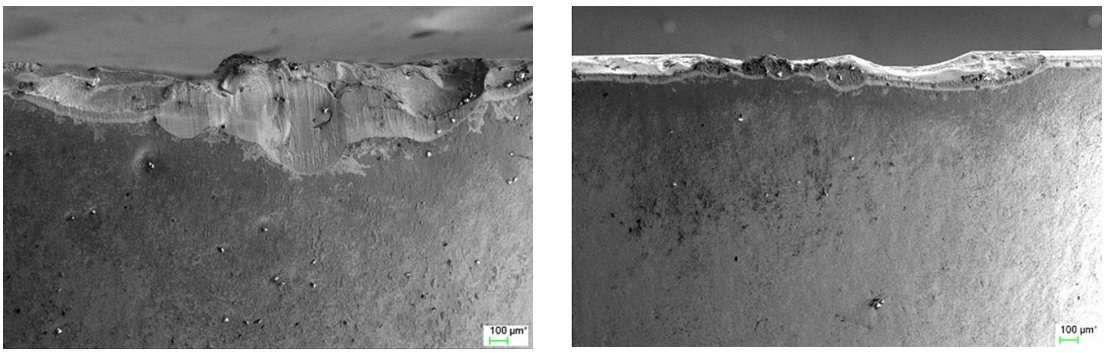


Figure E.0.2: FESEM Micrographs showing flank wear on the uncoated implanted inserts (a) non-implanted (b) 5E+15 (c) 8E+15 (d) 1E+16 (e) 2E+16, (f) 2E+16-120 keV ions/cm^2.

Appendix F

FESEM micrographs of the failed coated cutting tool inserts

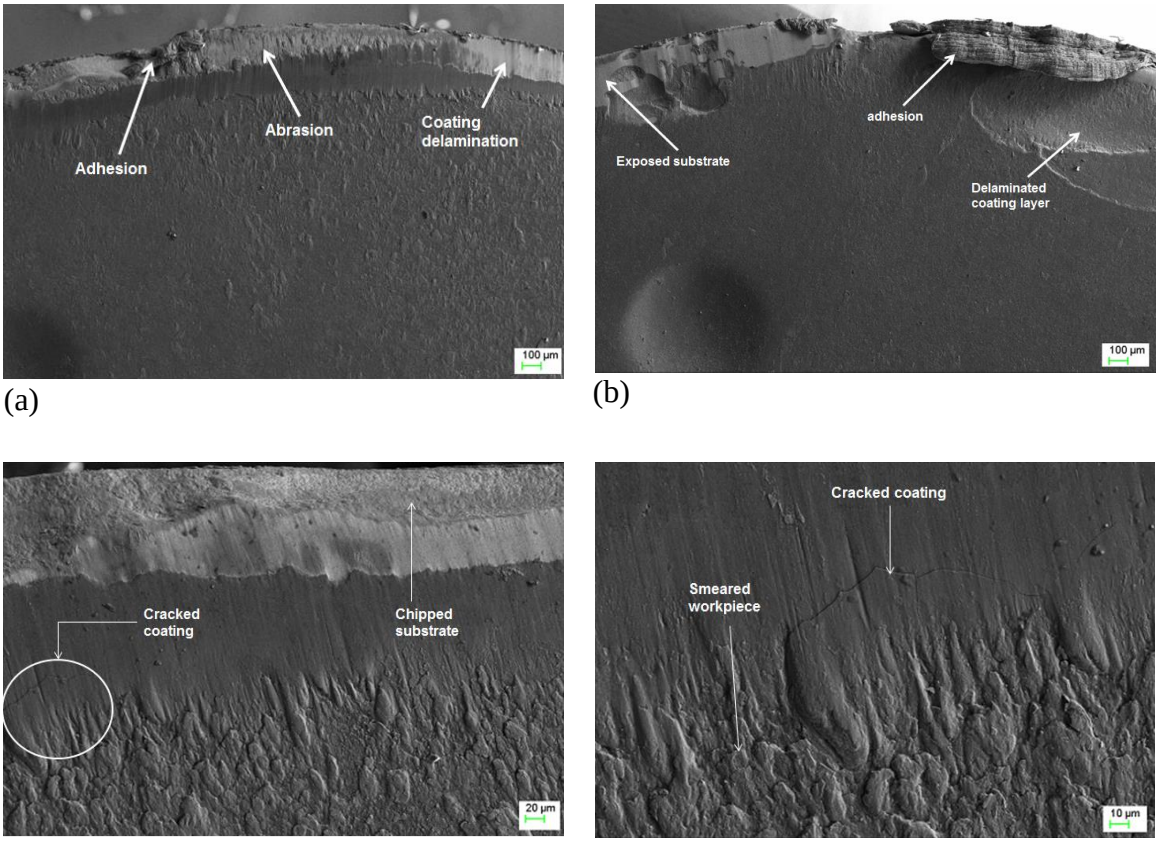
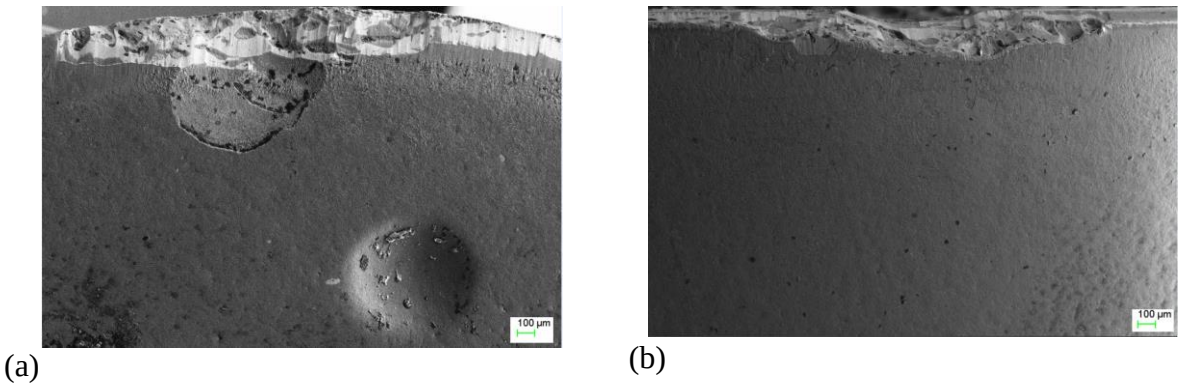
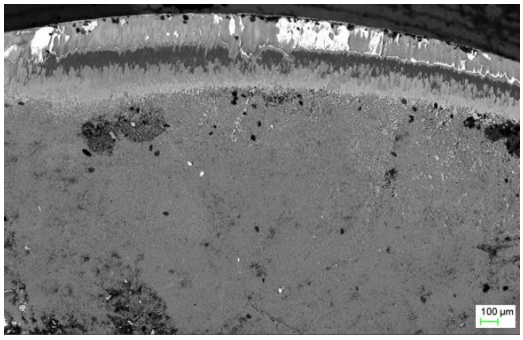
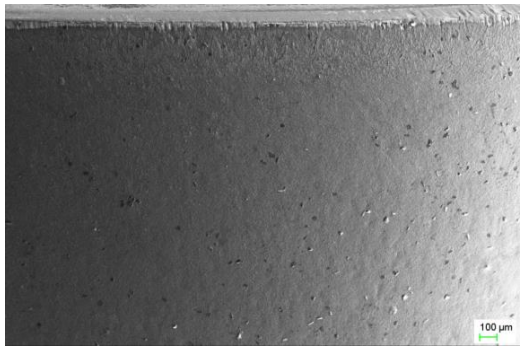


Figure F.0.1: Failure mechanisms of a set of non-implanted inserts on the rake face of the cutting inserts that were used at the same time.

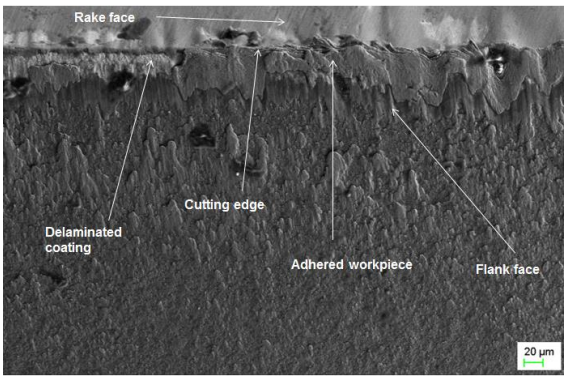




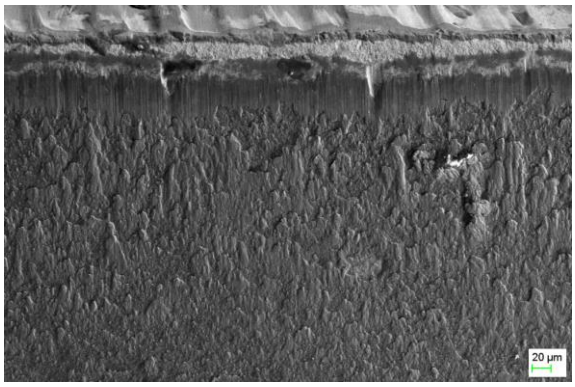
(c)



(d)

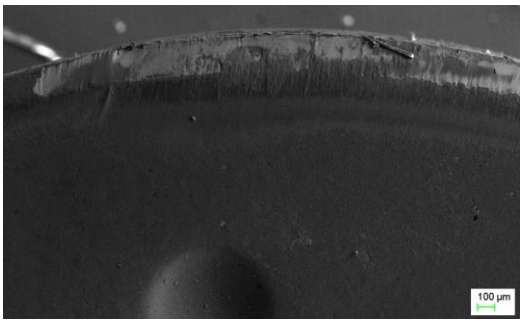


(e)

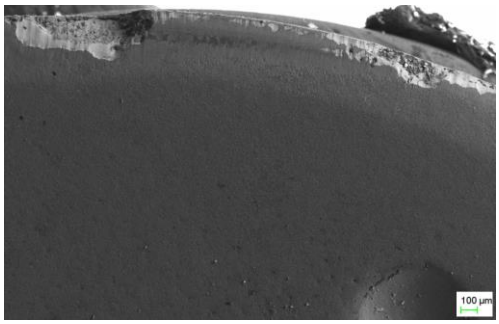


(f)

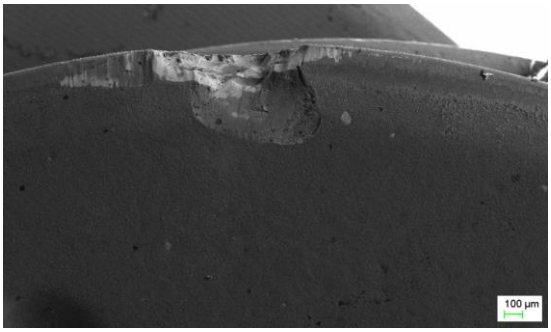
Figure F.0.2: Failure mechanisms of the cutting tool inserts with ion implantation dosage 5E15 ions/cm^2 (a) and (c) on the rake face and (b, d-f) shows the cutting edge from flank face.



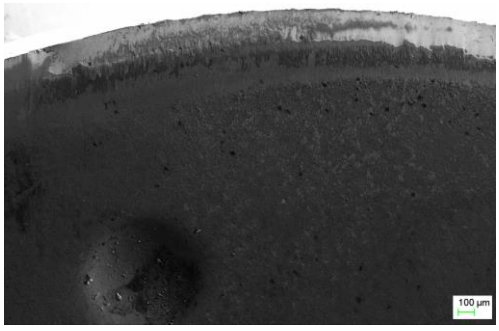
(a)



(b)



(c)



(d)

(e)

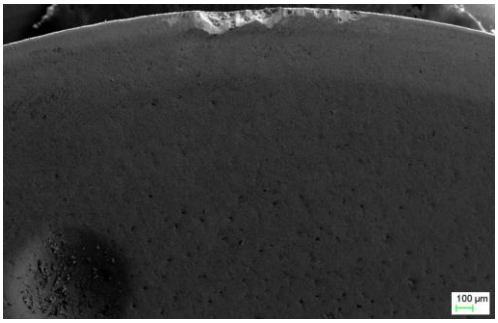
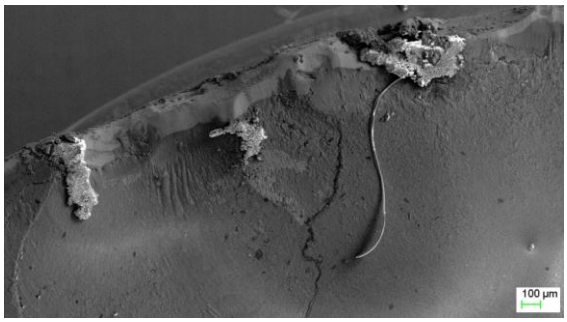
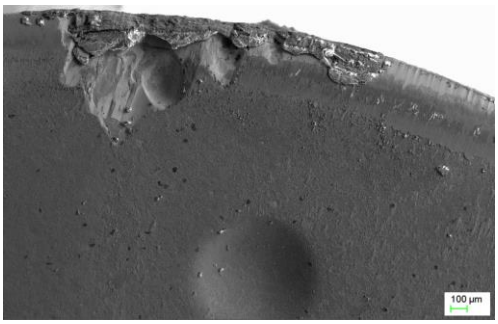


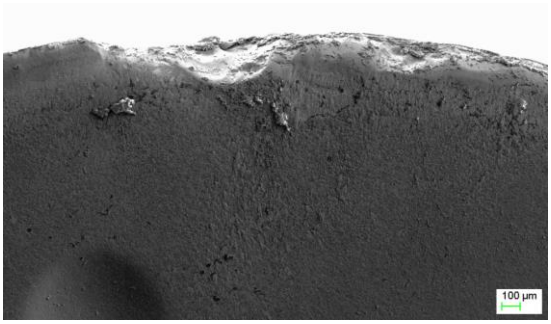
Figure F.0.3: Different failure mechanism of the rake face of the inserts implanted at 8E+15 ions/cm^2 dosage.



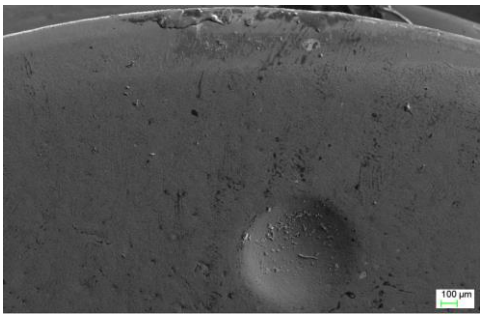
(a)



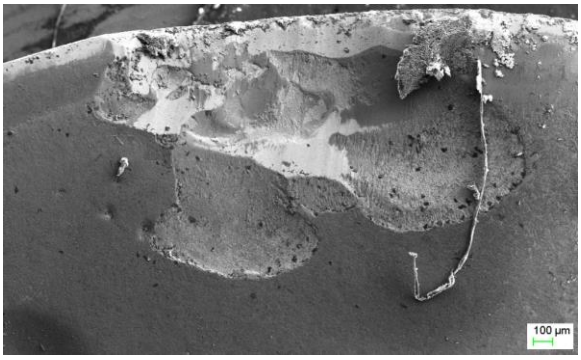
(b)



(c)

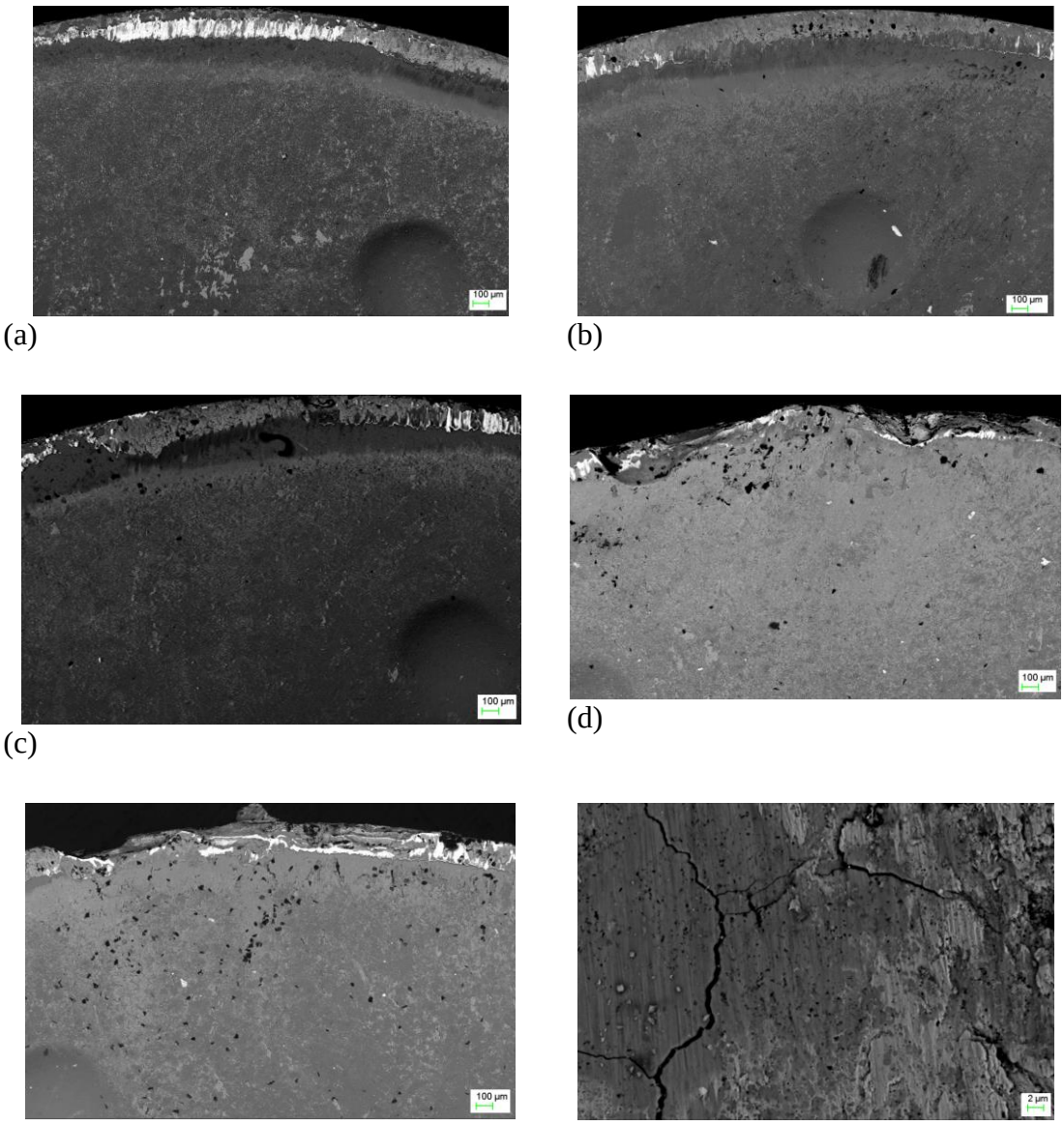


(d)



(e)

Figure F.0.4: Different failure mechanisms of the rake face of the cutting tool inserts implanted at 1E+16 ions/cm^2 dosage.

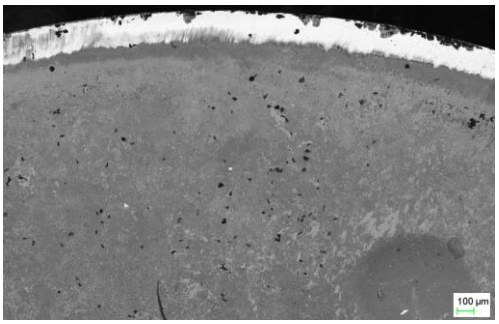


(a) (b)

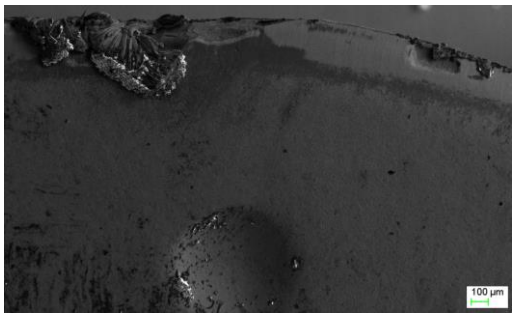
(c) (d)

(e) (f)

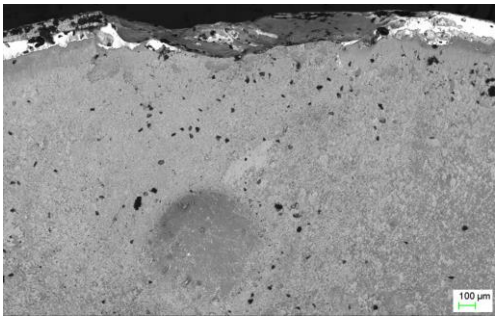
Figure F.0.5: Different failure mechanism of the rake face of the inserts implanted at 2E+16 ions/cm^2 at 100 keV.



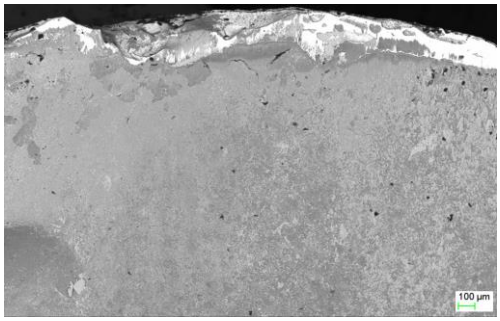
(a)



(b)

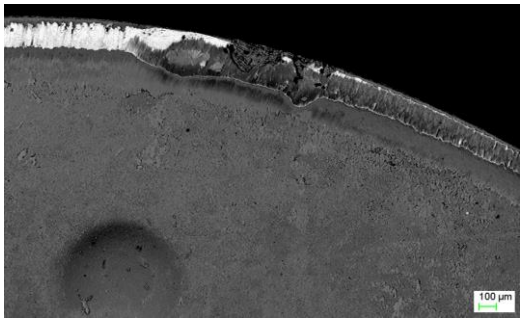


(c)

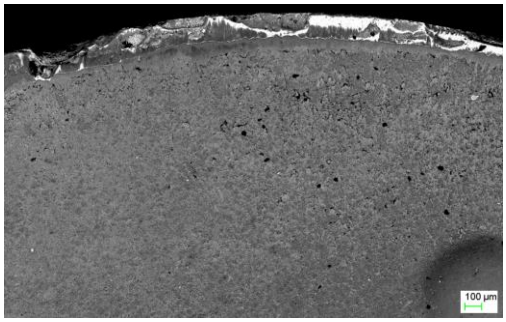


(d)

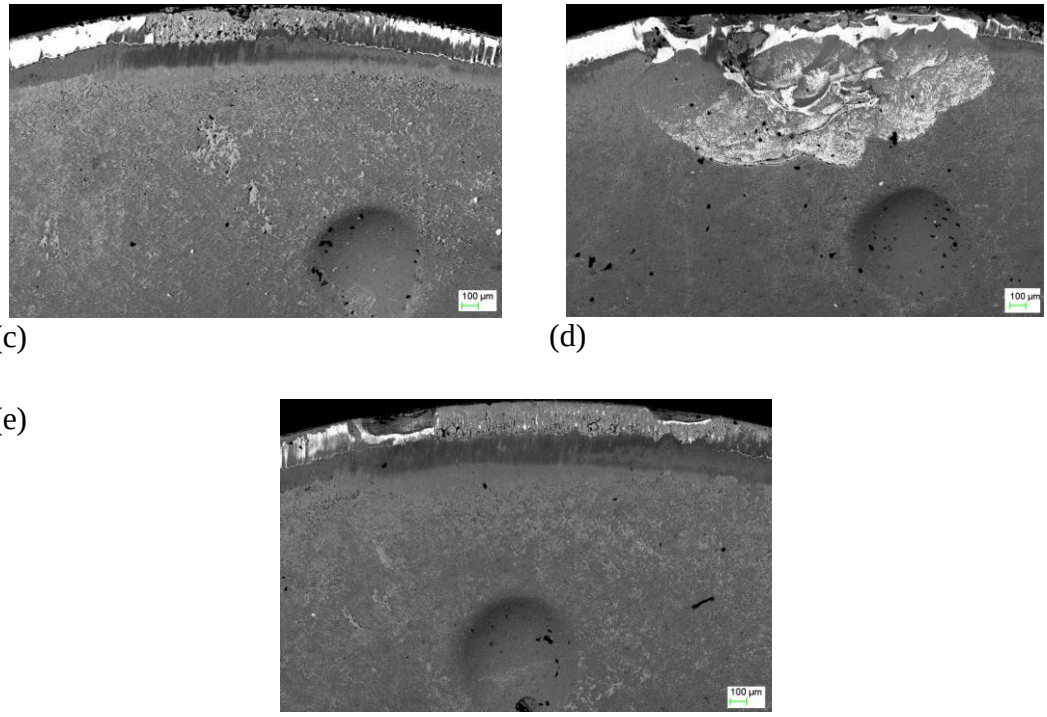
Figure F.0.6: Different failure mechanism of the rake face of the cutting tool inserts implanted at 2E+16 ions/cm^2 at 120 keV.



(a)



(b)

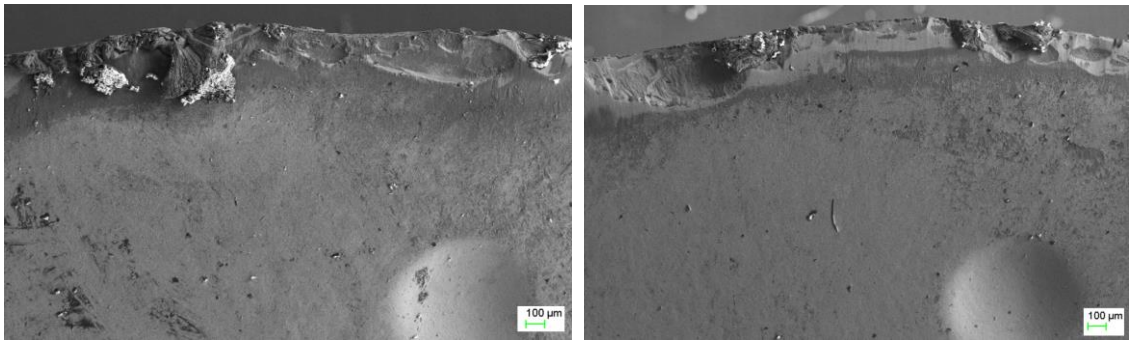


(c) (d)

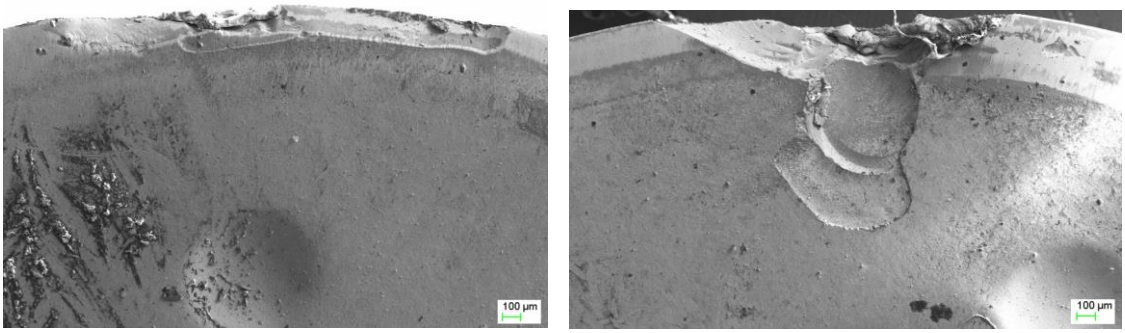
(e)

Figure F.0.7: Different failure mechanisms of the rake face of the cutting tool inserts implanted at 1E+17 ions/cm^2 dosage.

FESEM micrographs of the failed uncoated cutting tool inserts

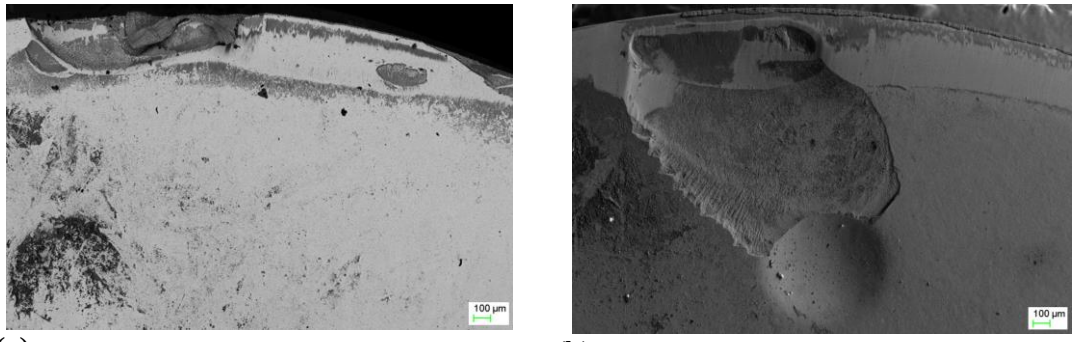


(a) (b)

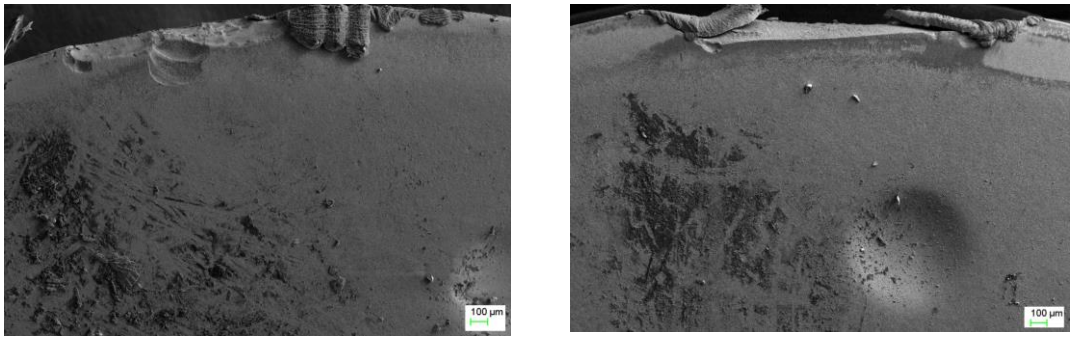


(c) (d)

Figure F.0.8: Failure mechanisms experienced by a set of non-implanted cutting inserts on the rake face.



(a) (b)



(b) (d)

(e)

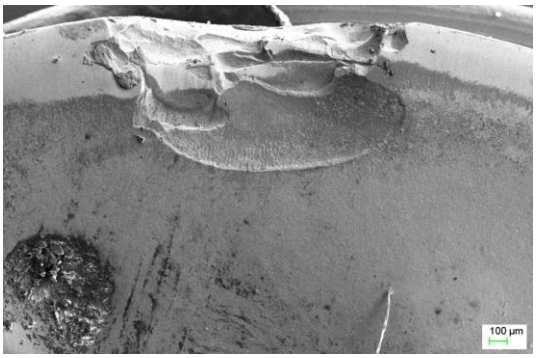
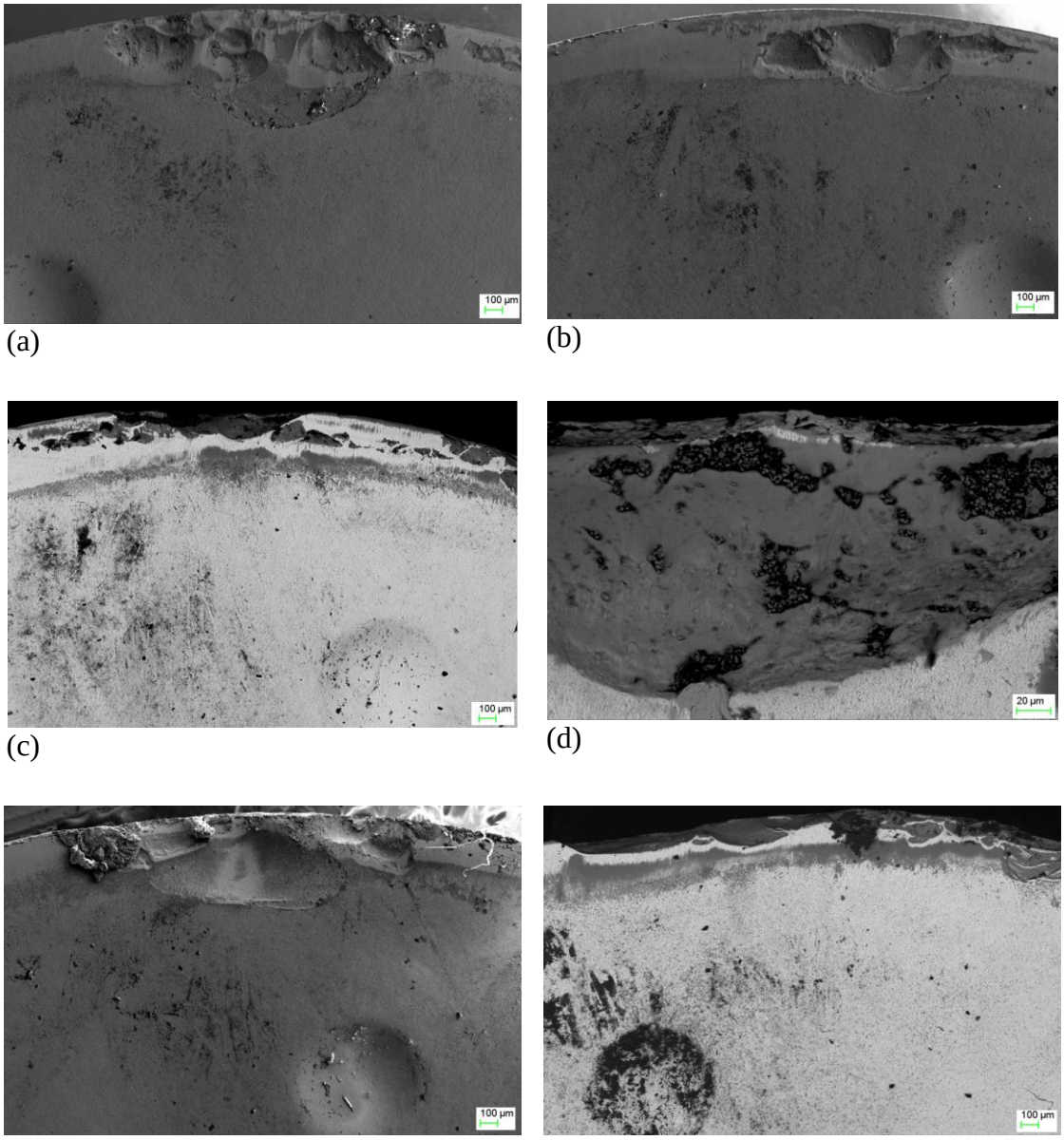


Figure F.0.9: Failure mechanism experienced by a set of cutting inserts on the rake face implanted at 8E+15 ions/cm^2.

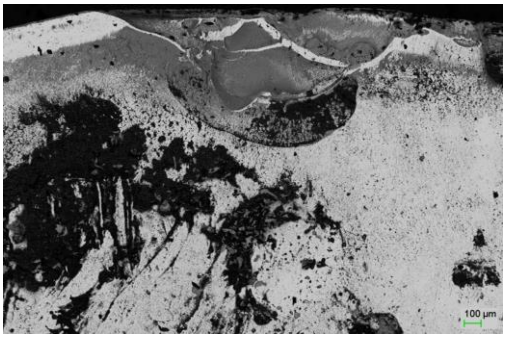


(a) (b)

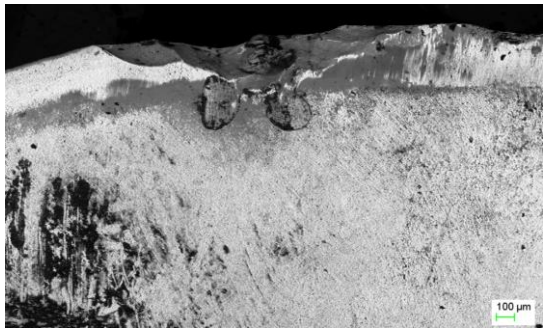
(c) (d)

(e) (f)

Figure F.0.10: Failure mechanisms experienced a set of cutting tool inserts on the rake face implanted at $1x10^{16}$ ions/cm^2



(a)



(b)

(c)

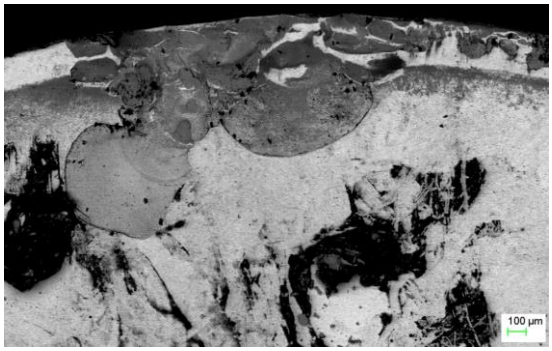
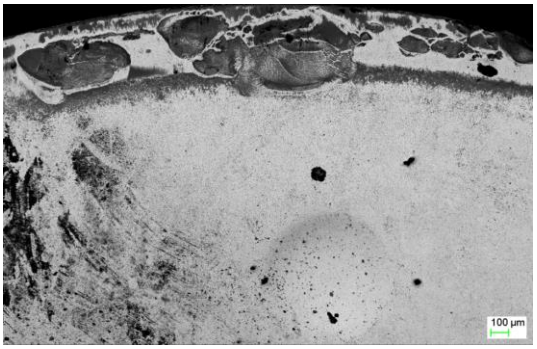
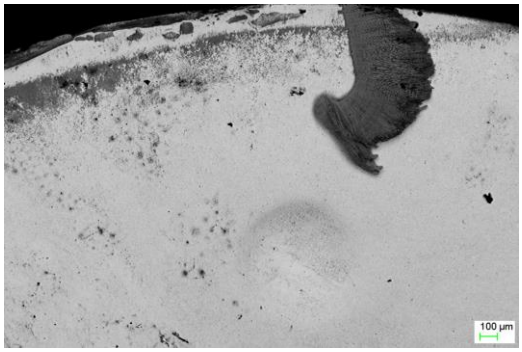


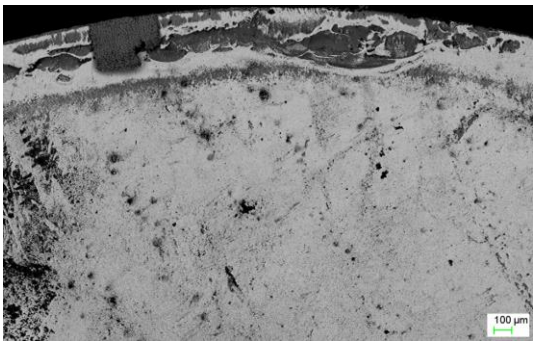
Figure F.0.11: Failure mechanisms experienced by a set of cutting tool inserts on the rake face 2E+16 ions/cm^2 at 100 keV



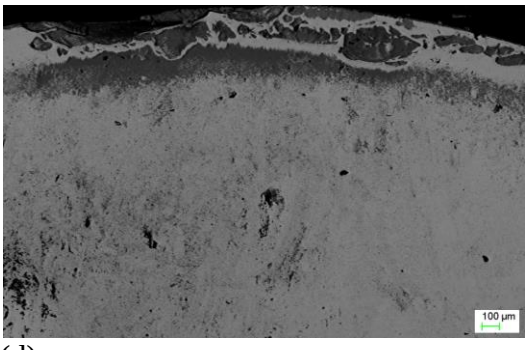
(a)



(b)



(c)



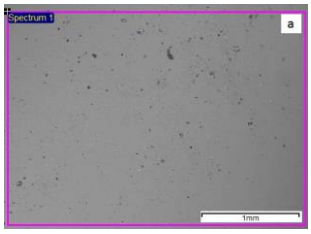
(d)

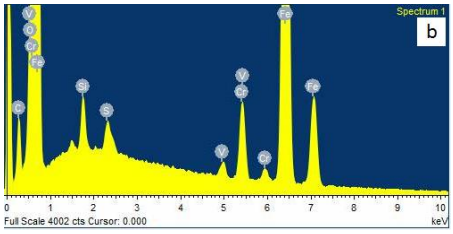
Figure F.0.12: Failure mechanisms of the cutting tool inserts implanted at 2E+16 ions/cm^2 -120 keV.

Appendix G

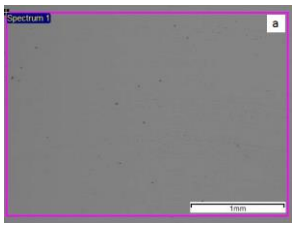
EDS results of the cutting chips

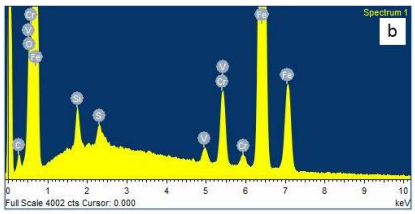
(a)





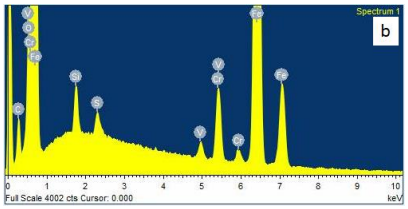
(b)



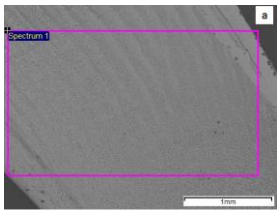


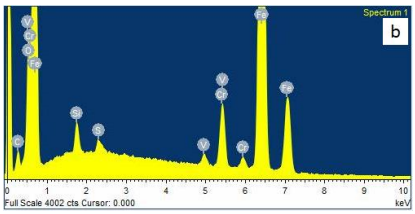
(c)



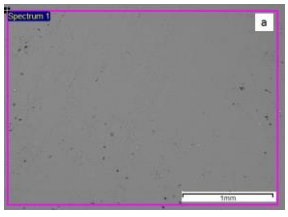


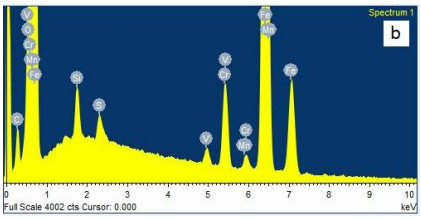
(d)



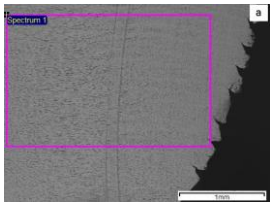


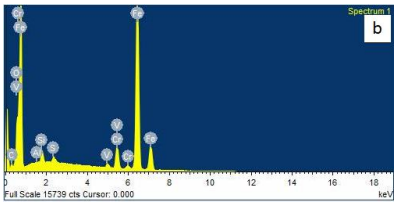
(e)





(f)





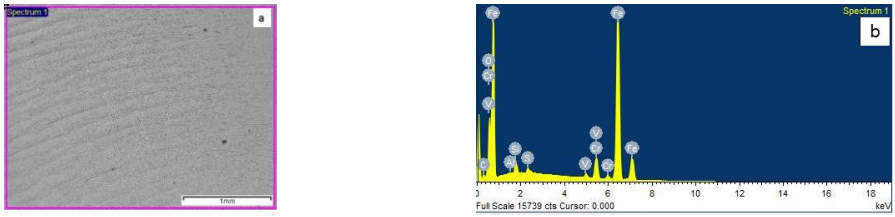
(g) 

Figure G.0.1: FESEM micrographs and the corresponding EDS analysis for the cutting chips (a) non-implanted, (b) 5E+15, (c) 8E+15, (d) 1E+16, (d) 2E+16 and (f) 1E+17 ions/cm^2 at 100 keV.